Confinement and Mobility in Artificial Lipid Bilayer Interfaces



Vivek Krishnan Ramakrishna
Wadham College
University of Oxford

A thesis submitted for the degree of
Doctor of Philosophy
in Physical and Theoretical Chemistry

Trinity 2019

Declaration

The work described in this thesis was carried out in the laboratory of Professor Mark Wallace, between October 2014 and November 2016 in the Chemistry Research Laboratory of the University of Oxford, and between September 2016 and November 2018 at Britannia House, King's College London. All the work herein is entirely my own unless explicitly attributed to collaborators. This work has not been submitted previously for any other degree at the University of Oxford or any other university. A publication stemming from this work is listed in Appendix A.



Vivek Krishnan Ramakrishna

Trinity Term 2019

Abstract

Confinement and Mobility in Lipid Bilayer Interfaces

Vivek Krishnan Ramakrishna - Wadham College - University of Oxford

Submitted for the degree of Doctor of Philosophy in Trinity Term 2019

All biological components are enclosed by membranes. Interfaces formed between membranes enable the transport of matter, information and energy between these components, but also serve as functional platforms for other processes. In these interfaces, membrane components such as lipids and proteins are recruited, sequestered and segregated to accomplish a range of operations. Often, sections of membranes are excised or inserted via transient interface formation. Due to the complexity of these processes, artificial models which represent reduced systems are used to understand the underlying physical, chemical and biological mechanisms. This thesis initiates an investigation into two key behaviours of membrane interfaces. Namely, the effects of substrates and intermembrane spacing on membrane mobility are studied using DNA linkers to alter the interactions between two model membranes; and the organisation of membrane components is studied using an artificial construct designed to mimic the structural properies of the membrane-deforming protein clathrin.

Chapter 1 introduces the role of lipid membranes, membrane proteins and membrane interfaces in biological systems. It also contains a discussion on some common models of membrane interface, and on the application of DNA nanotechnology in membrane systems analysis. Chapter 2 details the methods and techniques employed in this specific thesis. TIRF microscopy and single-molecule tracking techniques are detailed.

Chapter 3 introduces the artificial bilayer model used throughout the thesis. The interaction between two proximal bilayers and their diffusive properties are modulated using osmotic, ionic and density gradients across a GUV membrane. Next, DNA tethers are used to actively control the separation between the two membranes. Chapter 4 discusses a DNA-origami based clathrin mimic that can be programmed to form large scale assemblies on membranes. Chapter 5 summarises the work done so far and proffers a roadmap for future work.

Acknowledgements

"It's later than you think, but it's never too late", a clock tower once told me. This thesis has taken so long, I've amassed a not inconsiderable number of friends and well wishers I am grateful to, and far more whose patience I have tested. I wish I could include every single person who I'd like to thank and apologise to, but instead, I'll settle for apologising to those who I haven't thanked here. You know how grateful I am for you.

First, my sincere thanks to my supervisor, Mark, for the unending patience, support and ideas. Choosing to work in the Wallace lab is the best decision I've ever taken. To all the members of the Wallace Lab who I've worked with- when I grow up, I want to be exactly like (each and every one of) you. In particular, thanks to Helena for a most surprising friendship, her grating pragmatism and her perennially cheery disposition; Matt for being the ultimate flatmate, literally and *literally*; Carina for her unwavering zest-for-life; Hajra for being the glue that held everything together; Rav for the lore, and for Echopraxis; Matthew for all the treats, edible and cerebral; Jason for a shared interest in looking at things; Eve for introducing me to new experiences; Lyndsey, for the scientific synergy; John for merely His Divine Presence; Szabo for Netflix and energy drinks; and Joanne for all the coffee and wisdom. To Christopher I entrust the duty of maintaining lab morale; to Vivien, the onerous task of being the Big V; and to Steven, my pressure cooker.

I'd like to thank Prof. Andrew Turberfield and Céline Journot for a fruitful and educational collaboration on the DNA origami work. I hope all my future collaborations are as good as this.

My time in England has seen me pass through Southampton, Oxford and is likely to come to a close in London. Tom B, Noëlie, Jyotishko and Capt Chitla's combined

tutelage in Southampton helped me through my freshest days. The two years in Oxford were dream-like, thanks in no small part to Josh's fresh-faced enthusiasm, Kallol's generous box (and guidance), Alice's conspiracies and shenanigans, Patrick's dazzling aesthetic and Ethan's sheer variety. To Anna, Eoin, Fred, Ed, Dom, Grace, Urmila, Jon, Hannah, Hannah, Sarah(<3), Sarah, Sam, Sam, Sandy, Manuel, Ash, Laura *et al.* : I couldn't have wished for a better set of uni mates/drinking companions/posh twats. I would be remiss in not thanking Wadham College for facilitating a remarkable experience and also for the timely support. I would also like to thank Aga Borkowska for easing the lives of so many aspiring chemists.

Life in London has been a singularly excellent experience, and made all the more excellent by the companionship of Ivan, Seco, Lara, Frederike, Chaitanya, Gopika, Kasturi Aunty, Yubanaswa, Vamsi, Aniruddh, Chloe, Mike, Monica and Indy, amongst many, many others. Marya Shariq's friendship, love and wit constantly gladdened my heart.

Of the old guard, I owe a deep gratitude, first and foremost to the King, for always being around, and also for being a kind and just King; to Navjot Kukreja for his passion and temperament, which frequently helped correct my course when I strayed; and to Gangu for the regular pearls of wisdom. Aditya for the thoughtful advice and stark optimism which never failed to spark joy even on the glummest of days, Ashwin, for his infectious confidence, and for introducing me to the joys and horrors of avian taxonomy; all members of the extended Galeez gang, the most sensible and practical set of people I know; Jayendran for the constant check-ins; Ameya for his patience and liberal views; Aravind for being a real together guy; Arvind's interludes, which irregularly triggered dramatic changes in my life; Prof. Banerjee for his friendship and mentorship, Gappan for the political insight; and Bhargav for his scholarship and horde of degrees, that inspire both awe and envy.

I would also like to express my appreciation for the WhatsApp group chat currently titled 'Naala', and every person in it, for consistently challenging convictions and providing entertaining discourse. Mangta hai!

Thanks also to Deepa, Benny, Swarna, Nisha, Deepu, Tonu, Nalini and Lambu- I've know you too long to not see your part in this.

The last year has been one of confusion and uncertainty, and this thesis exists because of the friendship of three people, two dogs and one foetus. Beena has been a constant presence in my life in England. Her support and companionship have been unwavering through thick and thin, and there are simply no limits to her kindness and patience. I may never be able to repay my debt to her, but I shall try. Mushko and Russel's encouragement and entertainment have been of immeasurable worth. Priya and Srikumar are two of the finest people I have ever known, and my time as their ward has left me with the fondest of memories. I cannot overstate the importance of their advice and help, nor can I exaggerate the quality of their banter and their kitchen. I'd like to assure Baby Mira that she's in for a cracker of a life, that she'll never have as good a flatmate as her very first one, and I hereby grant her permission to harass, harangue and make ridiculous demands of me in perpetuity.

Lastly, but most importantly, the only reason I am even here is because of my family: Mum, Dad and Vishal. Thank you for letting me be. I could not ask for more. This thesis is dedicated to the three of you.

No one knows what it is supposed to gain from this. Nature, in her infinite wisdom, is presumably working on it.

- Douglas Adams, *Life, the Universe, and Everything*

Contents

1 Introduction **1**

1.1 Overview 1

1.2 Lipids 2

1.2.1 Lipid structure 2

1.2.2 Membrane self assembly 3

1.3 Biological membranes 5

1.3.1 Continuity and fluidity 6

1.3.2 Membrane organisation by diffusion 7

1.3.3 Membrane shape 9

1.3.4 Cytosis 10

1.4 Interfaces in biology 11

1.5 Artificial membranes 13

1.5.1 Giant Unilamellar Vesicles (GUVs) 15

1.5.2 Supported Lipid Bilayers (SLBs) 16

1.6 Fluorescence analysis of membranes 17

1.6.1 Total Internal Reflection Fluorescence (TIRF) microscopy . . 17

1.6.2 Single-molecule tracking 19

1.7 Hydrodynamic models of membrane diffusion 20

1.7.1 Theory of diffusion 20

1.7.2 The Einstein relation 20

1.7.3 The Saffman-Delbrück model 21

1.7.4 Interactions of membranes with solid substrates: The Evans-Sackmann model 22

1.7.5 Thermodynamic models of membrane interfaces 23
1.8 Experimental models of membrane interfaces 25
1.8.1 GUV-SLB interfaces 25
1.8.2 Stacked membranes and other artificial models 27
1.8.3 Hybrid live-cell-SLB interfaces 27
1.9 DNA models of membrane components 29
1.9.1 DNA nanotechnology 29
1.9.2 DNA-mediated membrane interactions 30
1.9.3 DNA origami 31
1.9.4 DNA origami on membranes 32
1.10 Single-molecule studies of lipid membranes 32

2 Materials and Methods **35**
2.1 Materials 35
2.1.1 Lipids 35
2.1.2 GUV electroformation 36
2.1.3 DNA spacers 36
2.1.4 DNA origami 37
2.1.5 Other materials 37
2.2 Model membranes 37
2.2.1 Small Unilamellar Vesicles (SUVs) 37
2.2.2 Supported Lipid Bilayers (SLBs) 38
2.2.3 Giant Unilamellar Vesicles (GUVs) 39
2.2.4 GUV-SLB interfaces 40
2.2.5 DNA interactions with membranes 40
2.3 Microscopy 42
2.3.1 Single-molecule TIRF microscopy 42
2.3.2 TIRF illumination improvement 42
2.3.3 Fluorescence Recovery After Photobleaching (FRAP) 44
2.3.4 Two channel epifluorescence microscopy 44

2.3.5 Image acquisition 46
2.3.6 Background subtraction 46
2.3.7 Single-molecule tracking 46
2.3.8 Diffusion analysis 47
2.4 A brief history of prior work 49

3 Control of Membrane Diffusion in Artificial Synapses 54
3.1 Diffusion in GUV-SLB interfaces 54
3.2 Dual bilayer single-molecule tracking 55
3.2.1 Specific methods 55
3.2.2 Forming the interface 55
3.2.3 Measuring lipid diffusivity 56
3.2.4 Membrane defects and lipid exchange 58
3.2.5 Membrane buckling 59
3.3 DNA oligomers as an adhesion-repulsion system 63
3.3.1 Membrane functionalisation 63
3.3.2 DNA oligo design 64
3.4 Results 65
3.4.1 DNA interaction with membranes 65
3.4.2 DNA diffusion at GUV-SLB interfaces 66
3.4.3 Cushioning effect of unhybridised DNA 68
3.4.4 Coupling effect of hybridisation of short DNA 69
3.4.5 Effect of hybridisation of long DNA 71
3.4.6 Interplay of cushioning and coupling behaviours of short DNA 71
3.4.7 Effect of temperature on diffusion 73
3.4.8 Effect of DNA on GUV membrane topography 74
3.5 Discussion 75
3.5.1 Polymer properties of DNA 75
3.5.2 Membranes in proximity to surfaces 77
3.5.3 Unhybridised DNA increases the height of the GUV 78

3.5.4 Hybridisation of short DNA strands pulls the GUV closer to the SLB . . . 78
3.5.5 Long DNA strands are tilted by the GUV . . . 79
3.5.6 Linker and spacer density affects GUV membrane conformation 79
3.5.7 Calculating intermembrane separation . . . 80
3.5.8 Evans Sackmann Model: Caveats . . . 81
3.5.9 GUV yield and DNA surface density . . . 84
3.6 Summary . . . 85

4 Modifying Membrane Morphology and Interactions with DNA Origami Clathrin-Mimic Networks 87
4.1 Shaping membranes . . . 87
4.1.1 Clathrin . . . 88
4.2 Design of DNA origami triskelia . . . 90
4.2.1 Polymerisation . . . 91
4.2.2 Dimers . . . 93
4.3 Membranes and triskelia . . . 93
4.3.1 Triskelia on monolayers . . . 93
4.3.2 Triskelia on SUVs . . . 94
4.3.3 Triskelia on GUVs . . . 95
4.3.4 Triskelia on SLBs . . . 96
4.4 Membranes and triskelia at interfaces . . . 97
4.4.1 GUV-GUV interfaces . . . 97
4.4.2 GUV-SLB interfaces . . . 99
4.5 Discussion . . . 101
4.5.1 Curvature effects of DNA origami . . . 101
4.5.2 GUVs and triskelia . . . 103
4.5.3 Magnesium and membranes . . . 103
4.5.4 SLBs and Triskelia . . . 105
4.5.5 Triskelia at interfaces . . . 105

4.5.6 Experimental considerations 107
4.6 Summary 107

5 Conclusion and Future Work **108**
5.1 Conclusion 108
5.2 Future work and experimental wish-list 109
5.2.1 Quantification of electroformation efficiency 109
5.2.2 Fluorescent DNA assays of GUV-SLB interfaces 110
5.2.3 DNA origami-based biomimics for membrane modification . . 111

A Publications **113**

B Code **114**
B.1 Python 114
B.1.1 GUI free TrackMate 114
B.2 ImageJ background subtraction macro (Java) 118
B.3 MATLAB 118
B.3.1 Track analysis 118

C DNA Origami schematics for CADNano **121**
C.1 Triskelion sequences 121

Bibliography **134**

List of Figures

1.1 Structure of the phospholipid DOPC 3
1.2 Structure of the sterol cholesterol 3
1.3 Monolayer self-assembly 3
1.4 Lipid shape and packing 5
1.5 Organisation in biological membranes 8
1.6 Membrane shaping by proteins 10
1.7 Clathrin endocytosis 11
1.8 Artificial lipid membranes 14
1.9 Giant Unilamellar Vesicles 16
1.10 Supported Lipid Bilayer 17
1.11 Total Internal Reflection Microscopy 18
1.12 Hydrodynamic models of lipid membranes 21
1.13 Adhesion-repulsion model 26
1.14 Hybrid cell-SLB interfaces 28
1.15 DNA-tethered membrane interface 30
1.16 DNA-mediated adhesion between GUV and SLB 31
1.17 DNA Origami on membranes 33

2.1 Cholesterol with TEG spacer 36
2.2 GUV electroformation 40
2.3 TIRF of a membrane interface 41
2.4 TIRF setup 43
2.5 Two channel fluorescence microscopy setup 45
2.6 Particle tracking 47

2.7 MSD vs Δt 48
2.8 Phase separation in GUVs 50
2.9 Chol-DNA as a trigger for GUV phase separation 52
2.10 iScat of GUV 53

3.1 GUVs resting on an SLB 56
3.2 Effect of osmotic and ionic forces 57
3.3 Lipid exchange 60
3.4 Buckling in GUVs 61
3.5 Defects at GUV-SLB interfaces 62
3.6 Single-molecule tracking in GUVs 62
3.7 Location of cholesterol-tagged DNA 67
3.8 Diffusion of DNA at interfaces 68
3.9 DNA only on one membrane 69
3.10 Effect of DNA concentration on SLB diffusion 70
3.11 DNA hybridisation across interfaces 70
3.12 DNA linkers as a fraction of total surface DNA coverage 72
3.13 Effect of temperature on interface diffusion 73
3.14 Normal diffusion in GUV 75
3.15 DNA surface-tethered conformations 77
3.16 DNA linkers and intermembrane separation 80
3.17 Diffusion vs. height 82

4.1 Clathrin 89
4.2 Design of DNA origami 90
4.3 Internal curvature of DNA triskelia 91
4.4 Schematics for triskelion assembly 92
4.5 Triskelia on lipid monolayers 94
4.6 Triskelia on SUVs 95
4.7 Triskelia on GUVs 96
4.8 Distribution of triskelia on GUVs 97

4.9 Triskelia on SLBs 98
4.10 GUV aggregation 98
4.11 Triskelia at GUV-GUV interfaces 99
4.12 Triskelia at GUV-SLB interfaces 100
4.13 Effect of origami internal curvature 102
4.14 Budding at boundary of interfaces 103
4.15 Budding due to inverted triskelia 104
4.16 Effect of Mg^{2+} on GUVs 105

C.1 Arrangement of helices 132
C.2 CADNAno routing for triskelion 132

Chapter 1

Introduction

1.1 Overview

Since the dawn of time, what we may call 'life' has tried to create order and complexity out of all that is *not* life. An important step towards this was the development of a barrier to keep everything that may be called 'life' apart from everything that therefore may not. In the current iteration of life, this protective and defining role is performed by lipid membranes. Everything in life is contained by membranes. The flux of all matter, information and energy into and out of these containers must invariably be facilitated by biological membranes. Modern organisms have several sophisticated methods to control the spatiotemporal properties of the membranes to efficiently undertake complex functions. Following on the heels of compartmentalisation, there developed specialised means to allow fluxes between compartments. Cells involve themselves in various types of interfaces, differing in function, size and temporality. The ability to remain individualised, yet not isolated [1], proved critical in the development of life as it exists today.

All this great complexity is underpinned by simple physical mechanisms. Artificial systems allow for paring down this complexity in order to examine specific aspects of complex biological phenomena. This thesis discusses the physical properties of membranes and membrane components, and how proteins and lipids interact in these confined environments. This discussion is conducted through two projects that utilise DNA-based models of membrane proteins. The first project employs simple DNA

constructs to control the separation between two membranes. The second project employs complex DNA constructs to induce local curvature of membranes.

This chapter provides an introduction to biological membranes and interfaces, and the systems and techniques used to study them. It focuses on membrane organisation, membrane shape, and the self-regulating interplay between the two. It also summarises the state of the art in experimental membrane research relevant to the two projects discussed later, and the theoretical background for studying interface dynamics.

1.2 Lipids

1.2.1 Lipid structure

All forms of life consist of cells that are surrounded by cell membranes, and all cellular membranes are made of lipids. In particular, they are made largely of amphiphilic lipids, which consist of a hydrophilic head region, and a hydrophobic (or oleophilic) tail region. The head is polar, and can be charged or zwitterionic. There are several types of head groups, varying in size and overall charge. The tail region is non-polar, and is composed of one or more chains of saturated, unsaturated, branched or cyclic hydrocarbons. The number of fatty chains, their lengths, and degree of saturation determine the shape and volume of the lipid. The presence of unsaturated bonds and branches change the physical properties of the lipids and lead to a decrease in order.

Phospholipids make up a large percentage of total lipids in organisms [2]. A phospholipid consists of a polar head containing a phosphate group, and a hydrocarbon region. 1,2-dioleoyl-*sn*-glycero-3-phosphocholine (DOPC) is a typical synthetic phospholipid, widely used in experimental research (Figure 1.1). It consists of a choline-derived head group, and two 18 carbon-long monounsaturated 'oleoyl' tails. The single double bond imparts a kink to each tail, rendering DOPC as a truncated cone.

Another important class of lipids are sterols, of which the most familiar one is cholesterol (Figure 1.2). Cholesterol makes up about 30% of animal cell membranes.

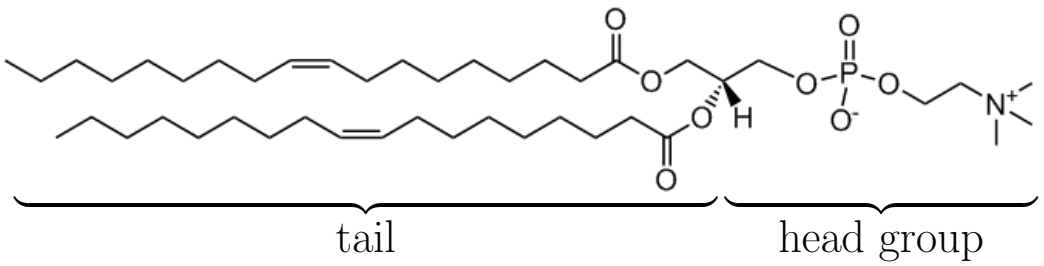

Figure 1.1: Phospholipid Structure. DOPC is an amphiphilic phospholipid with two hydrocarbon tails attached to a zwitterionic head groups. From avantilipids.com.

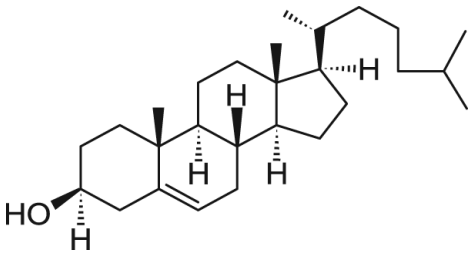

Figure 1.2: Sterol Structure. Cholesterol is amphiphilic molecule composed of a four-ringed hydrophilic region and a hydroxyl head group. From avantilipids.com.

Its hydrophobic moiety consists of four rings and a short hydrocarbon tail, while the head group consists of a hydroxyl group. Cholesterol is a modulator of membrane fluidity and plays an important role in maintaining membrane fluidity and membrane phase behaviour [3, 4]. Cholesterol intercalates between the tails of the phospholipids and stabilises their packing order via lateral van der Waals interactions [5]. At long length scales, it prevents clustering of lipids, while at shorter scales, lipid clusters enriched in cholesterol and exhibiting increased order— or lipid rafts— act as platforms for signalling and trafficking proteins [6, 7].

1.2.2 Membrane self assembly

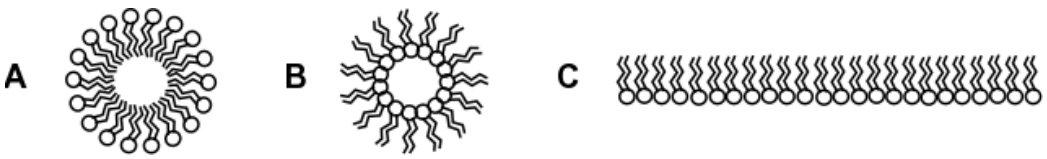

Figure 1.3: Monolayer self-assembly. Amphiphilic lipids in aqueous media self-assemble into micelles, inverse micelles and planar bilayers, from [8].

On a watery planet, amphiphilic molecules that could *self-assemble* in aquatic environments provided an efficient (and elegant) system to generate serviceable barriers. Amphiphilic lipids orientate into membraneous structures when present in mixtures of aqueous and organic solutions (such as might be found in a primordial puddle). This happens in order to minimise the interactions of the tail groups with any aqueous phases. This phenomenon is the hydrophobic effect [9]. The hydrophobic tails, being unable to form hydrogen bonds, disrupt the dynamic hydrogen bond network of water. This results in the formation of ordered, cage-like (or clathrate) structures of hydrogen bonds around the tails, thus decreasing the entropy of the system. The resultant increase in the free energy is countered by reducing the hydrophobic surface in contact with the aqueous phase. Thus, the polar heads interact with aqueous phase, while the tails extend into the organic phase. At interfaces between aqueous and organic phases and at air/water interfaces, for instance, the phospholipids arrange into spherical (micelles/reverse micelles) or planar monolayers (Figure 1.3).

The size of the head groups and the shape of the tails determine the packing of the lipids. The self-assembled shape can be predicted by the packing parameter S (Equation 1.1):

$$S = \frac{V}{a\ell_o} \tag{1.1}$$

where V is the tail volume, a is the projected area of the head group and ℓ_o is the tail length.

In a purely aqueous medium, phospholipids can also arrange into various lamellar and non-lamellar structures, depending on the shape of individual lipids and the overall lipid composition of the bilayer. The packing parameter for two chain phospholipids, for instance, ranges between 0.5 and 1, describing a truncated cone, which pack into bilayer vesicular structures [10]. One such assembly is a planar bilayer formed of two extended monolayers, where the tail groups face each other, forming a hydrophobic core. This core is shielded from the aqueous medium on both sides by the head groups. Spherical bilayer shells are entropically preferred in suspension, and

the enclosing structures so formed are commonly referred to as liposomes or vesicles (Figure 1.7) [11]. Thus, many biological membranes, discounting their contents, components and functions, are simply vesicles. Artificial vesicles, which may be composed of naturally derived or artificially synthesised lipids, are classified on the basis of their size and lamellarity [12]. Lipids with a more conical shape tend to form non-lamellar or non-bilayer structures by themselves, but when present in biological membranes, they help in modulating the lateral pressure in the membrane and thus stabilise the inclusion and binding of membrane proteins [13]

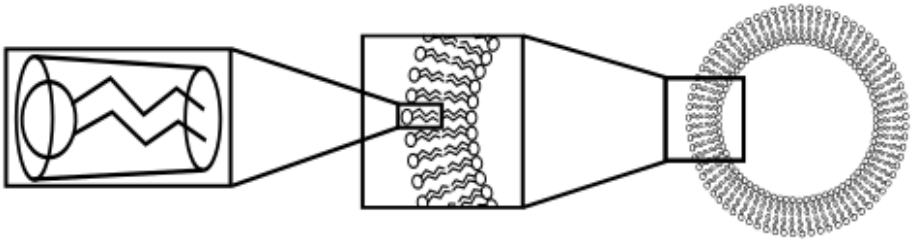

Figure 1.4: Lipid shape and membrane packing. The truncated conical shape of most phospholipids causes them to favourably pack into a spherical structure. From [8].

1.3 Biological membranes

Biological systems utilise the self-assembling property of lipids to create selectively permeable barriers through which to conduct exchanges with the external environment. Within the cell, membranes also demarcate regions of cells into pockets of specialised function, the organelles. Biological membranes consist of a host of components including lipids, proteins, peptides, sugars, and the sum total of their interactions and complexes. In addition to providing encapsulation, membranes enable transportation and communication with the external environment. Some organelles such as the Golgi body and the endoplasmic reticula are composed entirely of membranes, acting as platforms for various biological processes.

Proteins make up over 50% of the cell membrane by mass [14]. Proteins may either span the membrane via hydrophobic transmembrane domains, or associate with

the membrane via lipid anchors (peripheral proteins). Other membrane-associated proteins interact with the membrane electrostatically or via a number of protein-protein or protein-glycan interactions. Proteins are fundamental for transportation, signal transduction, detection among various other processes. The following sections discuss some of the ways in which membranes interact with and coordinate protein activity.

1.3.1 Continuity and fluidity

While the main function of the cell membrane is to separate the inner and outer environments, a very important quality of biological membranes is that they are selectively permeable. They allow certain molecules to pass through them, while blocking out others. Non-polar molecules and water (albeit slowly) can cross the membrane, but ions require special channels in order to do so. Cells also employ active transport mechanisms that expend energy to transport molecules against concentration gradients. Both active and passive mechanisms are critical for maintaining homeostasis in biological systems.

Another important feature of biological membranes is their fluidity. This was first described by the famous fluid mosaic model, according to which partially-embedded proteins and other molecules diffuse freely in the lipid membrane [15]. Membranes can be modelled as two-dimensional fluids, in which lipids and other components can diffuse over long ranges [16]. The diffusion of membrane components is dependent on their size, and the hydrodynamic properties of the membrane and the aqueous media on both sides. The viscosity of the membrane can be finely tuned by altering the local lipid composition [17]. This allows the cell to control the diffusion and organisation of membrane proteins, to be recruited to and assembled at specific sites (Figure 1.5 A). For example, the lipid raft hypothesis posits that membrane lipids separate into domains enriched in ordered lipids, which act as platforms for various critical biological functions [18].

1.3.2 Membrane organisation by diffusion

It is estimated that the human body contains over 1 km^2 of lipid membranes [19]. The composition of membranes varies between different membranes, between different regions of the same membrane, as well as between the two leaflets at a given region. They differ in lipid composition as well as protein and carbohydrate content. For example, in the plasma membrane of erythrocytes, the outer leaflet is rich in sphingomyelin and phosphatidylcholine lipids, while inner leaflet is enriched in phosphatidylethanolamine and phosphatidylserine lipids [20, 21]. Proteins often require the presence of certain lipids to regulate their activity [22]. So, rather than have all functional components continuously active and homogeneously distributed over its entire area, cells are able to efficiently direct proteins and lipids to specific regions of the membrane where their effects are amplified [23]. Flippases, floppases and scramblases are proteins that shuttle lipids between leaflets to alter leaflet composition [24, 20]. This influences the local physical properties of the membranes, such as permeability, curvature and charge concentration. Proteins are also recruited to specific sites on the membrane to perform their proteinly duties (Figure 1.5 B). For example, α-haemolysin is a membrane protein that is composed of seven monomers that assemble to form a membrane spanning pore [25]. Dynamin is a scission protein that induces fission by polymerising into a helical tube around membrane tubules. Indeed, it is recruited to these tubules because of their high curvature [26].

Molecular detection and recognition are two other processes that are mediated by membrane proteins. Both these processes trigger the recruitment of proteins that initiate different pathways. Viruses identify and bind to receptors on host membranes to initiate infection [29]. The immunological response of the host cell is also initiated by the detection of antigens on the pathogen by T lymphocytes. This is followed by the formation of the immunological synapse, which consists of a central cluster of T cell receptors surrounded by a ring of adhesion molecules [30]. Such spatial arrangement of proteins at interfaces has been shown to be driven by membrane

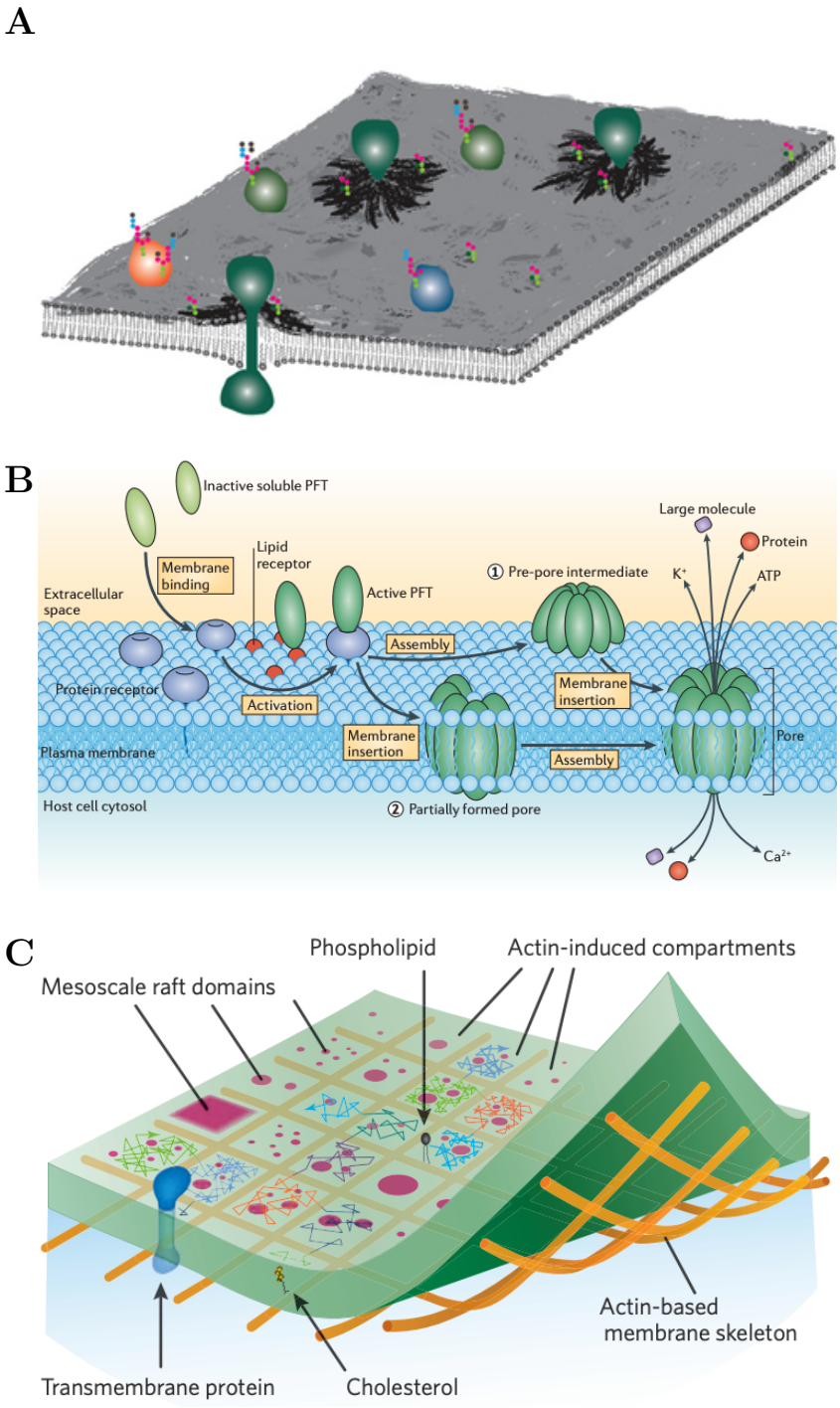

Figure 1.5: Organisation in biological membranes Biological membranes employ a variety of mechanisms to organise individual components and complexes in order to facilitate transportation and communication. (**A**) Certain species of lipids (dark) accumulate into domains to accommodate specific proteins (adapted from [23]). (**B**) Pore-forming proteins (PFTs) are recruited to membranes, oligomerise at the membrane surface and insert into the membrane to form a pore (from [27]). (**C**) The cytoskeleton interacts with the membrane and induces compartmentalisation of lipids and protein complexes (adapted from [28]).

fluctuations, and is dependent on the size of the proteins [31]. Similarly, ligand-receptor interactions at cell adhesion sites have been shown to slow down the lateral diffusion of lipids and receptors [32].

1.3.3 Membrane shape

Cell membranes are continuously changing in shape and size. This is due to the influence of protein interactions and lipid packing which impart deforming forces on the membrane. The cytoskeleton is the dynamic network of structural proteins that provide spatial guidance and support to cellular components, including the cellular membrane. Cytoskeleton components such as actin filaments associate with membrane and are essential in maintaining membrane integrity and stability. Actin assembly modifies membrane tension to enable membrane fusion [33], and also provides the force required to detach clathrin coated vesicles during endocytosis [34]. Recent cell membrane models, such as the picket-and-fence model, have expanded on the role of the cytoskeleton in compartmentalising and sequestering membrane components (Figure 1.5 C) [35, 36, 37].

Similarly, the glycocalyx is a dense matrix of glycoproteins and glycolipids that covers the outside of several types of cells. The glycocalyx has also been implicated in affecting lipid organisation in membranes [38], and also acts as repulsive modulator of cellular adhesion [39, 40].

The cell also controls the local composition of lipids to induce local shape changes. The density of lipids such as cholesterol or cardiolipin alters the packing order of the membrane, thus modulating local membrane rigidity. Inter-leaflet asymmetry in the density of differently shaped lipids can generate directional or localised curvature.

The diffusion and interactions of the various membrane components also influence the local curvature of membranes (Figure 1.6). Curved proteins such as BAR-domain proteins and clathrin impart curvature by scaffolding the membrane [41, 42]. Clathrin attaches to membranes via adaptor proteins; the polymerisation of clathrin into cages initiates and reinforces membrane budding, leading to vesicle formation [43]. Certain proteins insert amphipathic helices into one leaflet, and the resultant change in lipid

packing drives curvature. Protein crowding is known to drive membrane curvature by increasing lateral pressure [44].

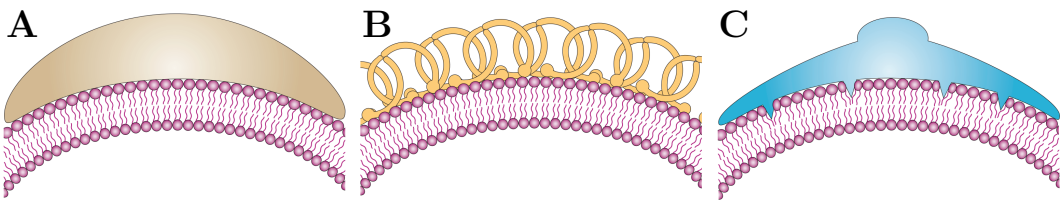

Figure 1.6: Membrane shaping by proteins. Proteins shape membranes by either (**A**) scaffolding, where a rigid, curved protein binds to a membrane and bends the membrane beneath it; (**B**) polymerising coats which stabilise intrinsic membrane curvature; and (**C**) insertion of amphipathic moieties, affecting the local spontaneous curvature. adapted from [45].

There is active debate about the actual role of membrane proteins associated with membrane shape changes [46, 47]. While some evidence suggests that the polymerisation or assembly of proteins generates forces that act upon the membrane [48, 49], it has also been argued that the same effect could be achieved by the lateral forces generated by protein crowding [44]. Similarly, clathrin plays a fundamental role in several cytotic pathways, but the mechanism of its assembly into a range of shapes, and how these affect membrane deformation, is still unclear [48, 50]. This suggests a need for experimental evidence isolating the effect of shape from the effect of aggregation. Chapter 4 presents a DNA origami mimic of clathrin which has been used to explore the effects of shape and assembly of such membrane-bound mechanisms on membrane shape.

1.3.4 Cytosis

In addition to the active and passive transporters, cells also employ vesicular transport mechanisms. Endocytosis and its counterpart exocytosis are examples of these bulk transport mechanisms into and out of cell, respectively. In these processes, membrane bound cargo is transported to the cell membrane, where the membranes fuse to release the cargo to the required side of the cell membrane. These vesicles were in turn produced by excising sections of another membrane in order to encapsulate the cargo.

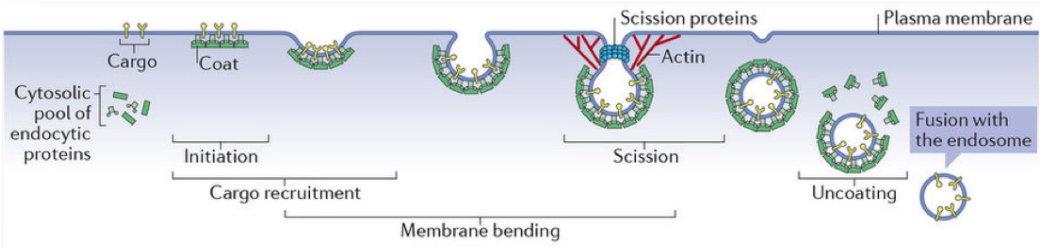

Figure 1.7: Stages of endocytosis Endocytosis is driven by proteins that are recruited from the cytosol and assembled on the membrane. First, proteins such as clathrin assemble into a 'coat' which deforms the membrane at the site where the target cargo is present. Other proteins help to stabilise the developing bud, while scission mechanisms act to release the vesicle. The coat then disassembles, and the proteins cycle back into the cytosol. From [51].

Fission and fusion are energy-intensive operations. Both processes involve overcoming repulsive forces to bring membranes in contact as well as transiently exposing the hydrophobic core to the aqueous environment. Proteins assist in the fission and fusion processes at various intermediate steps, from initiating, imprinting and driving budding to recruiting, docking and mediating vesicle fission. In general, vesicle formation for cytosis pathways comprise of two steps: first, the membrane is deformed by curvature imprinting proteins such as clathrin or caveolin. This is followed by a scission mechanism such as dynamin or actin polymerisation which releases the vesicles [52]. On the other end of the cytotic pathway, vesicle fusion is mediated by protein complexes such as SNARE, which undergo conformational changes in a 'zippering' action to provide the force required to overcome membrane repulsion for membrane fusion [53]. While clathrin mediated endocytosis is the classic endocytosis pathway, several clathrin independent endocytosis pathways are also recognised [54].

1.4 Interfaces in biology

In a way, the two integral events of any cytotic pathway, fission and fusion, can be described as forming transient interfaces. In a more general sense, interactions between two membranes forms the basis of several biological functions. Specialised membrane interfaces arose from the need for cooperation and the evolution of multicellularity.

Cells (and organelles within them) interact with each other through regions of physical contact between membranes. A synapse forms when two membranes come in close proximity such that they influence each other's physical properties. One of the most famous membrane interface is the *neuronal synapse*, within which protein mediated vesicular trafficking (being yet another interfacial process) enables signal transmission across neurons. The *immunological synapse* is formed between lymphocytes and antigen presenting membranes, through which the immunological response is carried out [30]. The functional component of the endoplasmic reticulum and Golgi apparatus is a dynamic network of membrane tubules and flat membrane disks called cisternae [55]. Several viruses and bacteria employ mechanisms for attachment, fusion and infection of host cells [56]. Cells in multicellular organisms are adhered to the extracellular matrix and other substrata via adhesion sites. Cellular adhesion is mediated by a combination of attractive and repulsive forces between the membrane and its target.

In many of these processes, pathways are initiated by the local redistribution of membrane proteins and other signalling molecules. These are initiated on nanoscopic length scales, and rapidly result in micron-scale organisation, such as the structures observed in the immunological synapse [57, 58]. As can be expected, the density and organisation of membrane components is influenced by the confined geometry of the interface. Binding and non-binding proteins are segregated by adhesive and repulsive forces acting on the membranes at the interface. Simultaneously, the membranes and recognition molecules play a role in the arrangement and recruitment of interfacial components. Given the scale and complexity of these synaptic processes, artificial models of membrane interfaces provide a means of deconvoluting the myriad physical phenomena involved in them. A more detailed understanding of how molecules move and interact within the interface will allow for the development of ever more complex artificial systems. Simultaneously, these model systems must also allow for probing by novel investigative techniques. To this end, the following sections discuss some of the techniques and models used in contemporary biophysics.

1.5 Artificial membranes

Cell membranes are complex, 2-dimensional sea of lipids, proteins, glycolipids, glycoproteins, and assemblies and complexes thereof. It is impractical to study the physical properties of individual components in them. Artificial bilayers are simplified lipid bilayers with a controlled number of parameters that help in understanding the effect of individual and ensemble elements that constitute biological membranes. They are built from the bottom up, allowing for controlling the composition and physical properties, and consequently the complexity, of these model membranes. (The work presented in this thesis were funded by a grant imaginatively titled CoSMiC: **Co**mplex **S**ynthetic **Mi**mics of the **C**ell membrane.)

The characteristic of amphiphilic lipids in aqueous environments to self assemble into entropically or kinetically favourable structures can be exploited to synthesise different kinds of artificial membranes for specific purposes. These are determined by the particular property to be reproduced and also by the technique used to study them. Langmuir monolayers formed at air/water interfaces (and when transferred to a substrate, Langmuir-Blodgett films) (Figure 1.8 A, B) are used to study lipid ordering and mechanical properties of individual leaflets. Planar bilayers, as the name suggests, are membranes restricted to a planar configuration. This makes them useful in optical analysis using techniques like total internal reflection fluorescence (TIRF) microscopy. Planar bilayers can be associated with a solid substrate— be it suspended across an aperture (black lipid membranes, Figure 1.8 C) [59, 60], or directly supported by a substrate (Figure 1.8 D)[61, 62, 63]. They can also be floating over a substrate [64], or cushion or tethered by polymers [65, 66, 67](Figure 1.8 E, F). Droplet interface bilayers formed between two opposing monolayers at oil-water interfaces allow access to both sides of the membrane (without the excess solvent often trapped in suspended bilayers) and are ideal for studying ion channel and membrane pores (Figure 1.8 G) [68]. Protein-reinforced nanodiscs are useful for studying proteins in minimal lipid environments (Figure 1.8 H) [69].

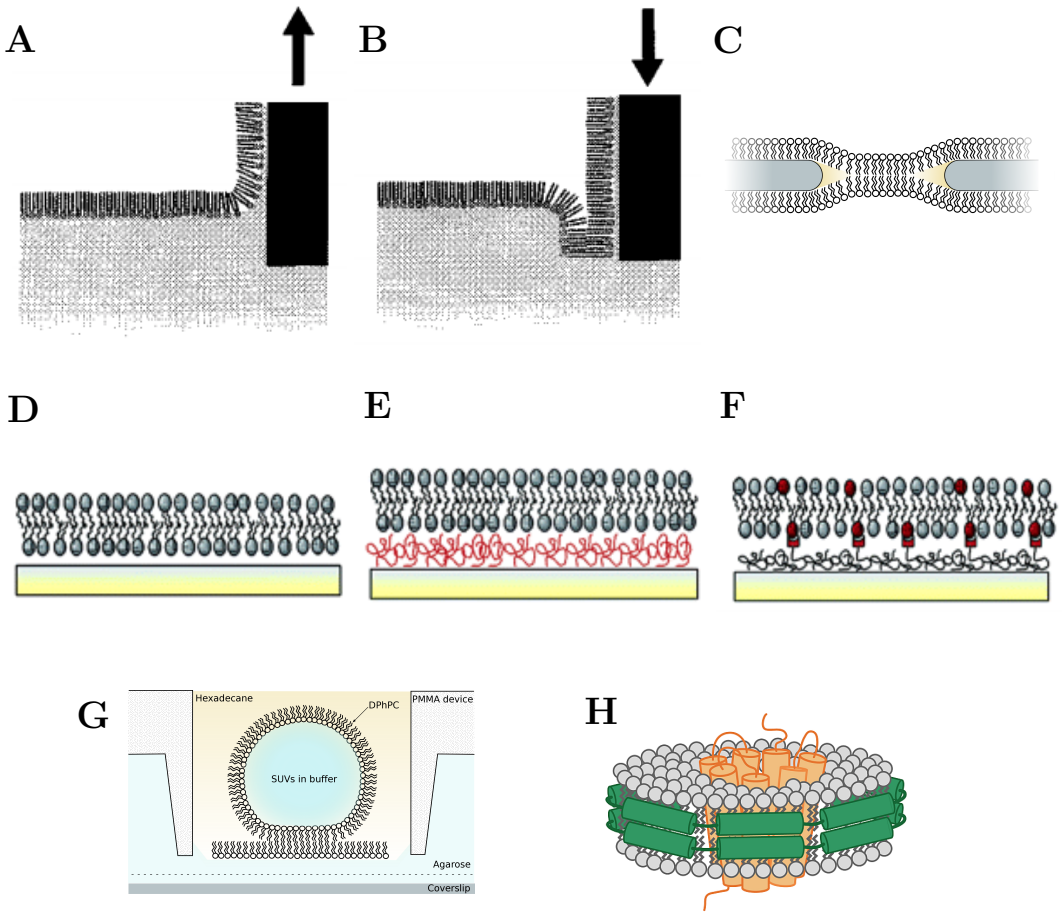

Figure 1.8: Artificial lipid membranes Some examples of artificial model membranes: (**A**,**B**) Monolayer and bilayer deposited by Langmuir-Blodgett method (adapted from [64]); (**C**) Black lipid membrane (from [8]); (**D**, **E**, **F**) Planar supported membrane, planar polymer-cushioned membrane and planar tethered membrane (adapted from [70]); (**G**) Droplet interface bilayer (from [8]); (**H**) Nanodisc with membrane scaffold proteins (from cube-biotech.com).

Vesicles are another class of typically spherical membranes, which can encapsulate a volume of buffer or even molecular cargo. They are usually free membranes, *i.e.*, they do not interact with any solid substrates. These are useful when the effects of curvature or trans-membrane chemical gradients in osmotic pressure or ionic concentration are required [71, 72] . Small unilamellar vesicles (SUVs, of diameter <100 nm) are useful in experiments that require encapsulation and release [73]. Their tendency to fuse to form larger membranes is also employed in membrane fusion studies [74]. SUVs also provide a high curvature environment for protein studies [75]. Giant unilamellar vesicles (GUVs, of diameter >1 µm) are comparable in size and curvature

to cell membranes, and are thus a very popular model for cell membrane studies [76]. Their large size makes them accessible to optical microscopy [77, 4]. Vesicles encapsulated within vesicles have also been imaginatively characterised as vesicle reactors and protocells [78, 79].

The high curvature stress in the SUV membrane can be utilised to make them fuse into larger membranes such as planar supported bilayers [62]. Work done for this thesis extensively employed giant unilamellar vesicles and supported lipid bilayers, and a short introduction to these models follows.

1.5.1 Giant Unilamellar Vesicles (GUVs)

Giant Unilamellar Vesicles (GUVs) are by far the most commonly used model system for cell membrane studies. They are characterised by low curvature, controllable tension and large size. Both sides of the membrane are free from substrate interactions, making them suitable for the study of transmembrane proteins [71]. The large size of GUVs also makes them ideal for visualising with light microscopy (Figure 1.9). GUVs have been employed in the study of liquid-liquid phase separation [4, 80]. The tension in the GUV membrane can be controlled by varying the osmotic gradient across the membrane. Bending rigidity studies have been carried out using fluctuation analysis of GUV membranes [81, 82].

GUVs were traditionally formed by the gentle hydration of dry lipid films (pioneered by Reeves and Dowben in 1969 [83]), often also subjected to thermal cycles. A key improvement was electroswelling, which drastically increased yield and reduced preparation time, while avoiding thermal variation [84]. GUVs can also be produced by gel-assisted hydration of lipid films embedded in polymer hydrogels [85]. More recently, microfluidic systems have been developed, enabling tighter control on vesicle size. GUVs with incorporated proteins can be synthesised by electroforming in the presence of proteoliposomes (SUVs with proteins) [86].

Electroformation is by far the most commonly employed protocol of GUV formation, and was also the method of choice in this thesis. Dried lipid films are deposited on to electrodes which are then hydrated with an aqueous medium. As in the gentle

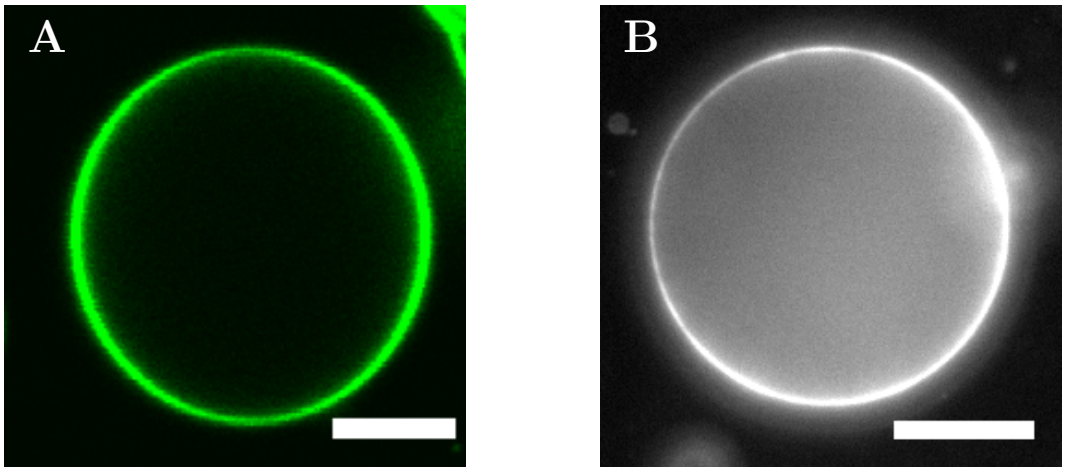

Figure 1.9: Giant Unilamellar Vesicles GUVs are giant (> 1 µm diameter), unilamellar (single bilayer) vesicles (enclose volume). (**A**) Fluorescently labelled GUV visualised at the equatorial plane using confocal microscopy. (**B**) Fluorescently labelled GUV visualised at an apical plane using epifluorescence microscopy. Scale bars 20 µm.

hydration method, the solution flows between individual lipid films, and causes them to swell. The application of an electric field increases the repulsion between the lipid films, accelerating the formation of vesicles with size >1 µm. One drawback of the electroformation process is that the presence of ions impedes the formation of vesicles, though electroformation in physiological ionic concentrations have been reported [87].

1.5.2 Supported Lipid Bilayers (SLBs)

Supported lipid bilayers or SLBs are a popular model for optical studies. Planar membranes can be assembled on glass coverslips, allowing for easy visualisation under a microscope. The planar geometry is conducive to high-resolution optical imaging by epifluorescence or TIRF microscope—which makes possible imaging of the dynamics of single molecules [88]. SLBs are also commonly used to passivate coverslips for the purpose of imaging GUVs and cells. As mentioned earlier, SLBs only allow physical access to one side of the membrane. As such, the behaviour transmembrane proteins with large cytosolic domains is altered by substrate interactions. Moreover, the surface properties of the substrate, such as roughness, hydrophilicity and charge, may also affect the physical properties of the membrane. Despite this, SLBs are

suitable models to study lipid behaviour, and have been regularly employed to study the diffusion and segregation of lipids in membranes.

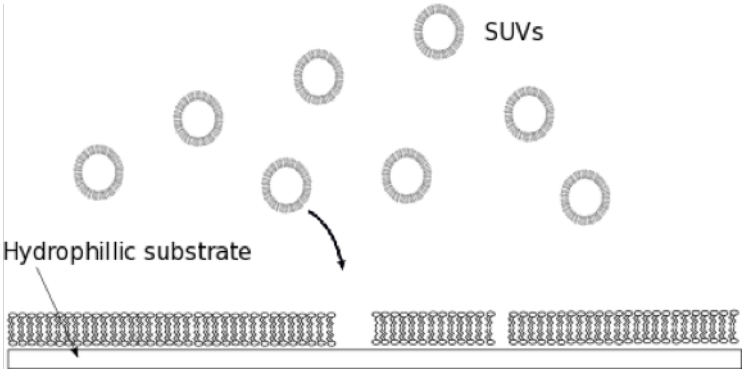

Figure 1.10: Supported lipid bilayer SLBs are prepared by the fusion of small unilamellar vesicles (SUVs) on a hydrophilic substrate.

SLBs are typically prepared by Langmuir Blodgett deposition [61], or by action of vesicle fusion (Figure 1.10) [70, 62]. The membrane is separated from the substrate by a thin layer of water, which preserves lipid fluidity. There is no consensus on the thickness of this water layer, with reported values ranging from 1 nm to 60 nm [89].

1.6 Fluorescence analysis of membranes

The experiments carried out in this thesis utilise fluorescence microscopy to visualise diffusion and assembly of membrane components. Epifluorescence microscopy, total internal reflection fluorescence microscopy and confocal microscopy have been carried out at a range of fluorescence levels, from bulk to single molecule.

1.6.1 Total Internal Reflection Fluorescence (TIRF) microscopy

Total internal reflection fluorescence (TIRF) microscopy is an established technique that employs the principle of total internal reflection to illuminate a small volume of the sample [90]. Whereas in epifluorescence microscopy the entire sample volume is illuminated, only a volume 100-200 nm above the cover slip is illuminated in TIRF microscopy. This means that only fluorophores close to the surface of the coverslip are excited by the incident illumination.

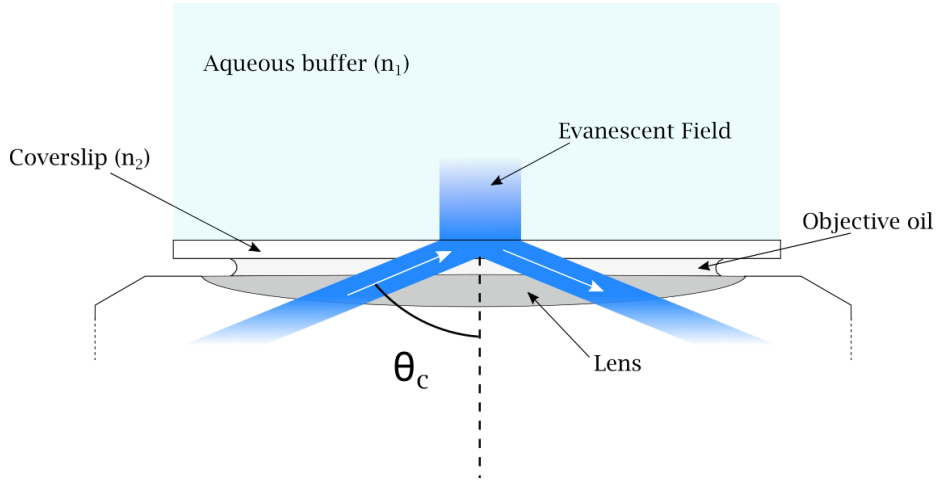

Figure 1.11: Total Internal Reflection Microscopy An aqueous sample with refractive index n_1 on a glass coverslip of refractive index n_2. The objective is in contact with glass via index-matched oil (matched to n_2), so that the beam passes through to the glass-sample interface without any deviation. An incident laser beam is aligned such that it is refracted through the objective lens at just over the critical angle θ_c, causing it to be totally internally reflected, generating an evanescent field that propagates into the sample.

In a typical microscopy experiment, the angle of incidence of the illumination beam at the slide-sample interface is lower than the angle of refraction in the lower refractive index aqueous sample solution— that is, the beam is transmitted into the sample. At the critical angle θ_c, the refracted beam is tangential to the interface- it is not transmitted into the medium. This critical angle is given by

$$\theta_c = \sin^{-1}(n_1/n_2) \tag{1.2}$$

where n_1 is the refractive index of the buffer, and n_2 is the refractive index of the glass coverslip.

In TIRF microscopy, the illumination beam is directed at the sample such that the angle of incidence is greater than the critical angle, causing total internal reflection of the beam. It is to be noted that this phenomenon occurs when $n_2 > n_1$. This leads to the generation of an evanescent wave perpendicular to the plane of incidence and into the sample medium. This wave decays exponentially along the perpendicular direction (z) and for an incident beam of intensity I_0, the intensity in the sample I is given by

$$I(z) = I_0 e^{-z/d} \tag{1.3}$$

The depth of propagation d of this wave is

$$d = \frac{\lambda_0}{4\pi} \left(n_2^2 \sin^2 \theta - n_1^2 \right)^{-1/2} \tag{1.4}$$

λ_0 is the wavelength of the light incident at angle θ. Chapter 2 details the optical setup employed for TIRF experiments.

1.6.2 Single-molecule tracking

When fluorophores are recorded on a CCD or CMOS sensor, the image captured is not the actual particle itself, but the convolution of the fluorophore's illumination profile and the point spread function of the imaging setup. Moreover, the noise from background illumination and optical artefacts is also captured. The main advantages of TIRF microscopy are the increased power density of incident light in the illuminated volume, and a decreased amount of noise from the bulk of the sample. This translates to a higher signal to noise ratio, that allows for localising the point source (fluorophore) from the point spread function. This typically involves the fitting of an ideal point spread function to the recorded data, such as with a 2D Gaussian of the form,

$$G = A \exp\left(- \left(\frac{(x - x_o)^2}{2\sigma_x^2} + \frac{(y - y_o)^2}{2\sigma_y^2} \right) \right) + B \tag{1.5}$$

where A is the amplitude, (x_o, y_o) are the coordinates of the centre of the molecule, σ_x and σ_y are standard deviations in the x and y directions respectively, and B is an offset. The error in localisation depends on the number of photons detected (N) as well as the standard deviation of the Gaussian σ, and scales as $\sigma/\sqrt{N}$ [91, 92]. The trajectory of a fluorophore is obtained by linking its position in consecutive frames, as described in Chapter 2, and its diffusion coefficient is calculated.

1.7 Hydrodynamic models of membrane diffusion

1.7.1 Theory of diffusion

Brownian motion refers to the random motion of particles in a fluid resulting from collisions with other molecules. In the 2-dimensional continuum of the lipid membrane, lipids and proteins diffuse within the plane of the membrane. The mean squared displacement (msd, second moment) of a free particle is linearly proportional to observation time, while mean displacement will be zero, by symmetry. This is expressed as,

$$\langle \Delta r^2 \rangle = 4D\Delta t, \qquad \langle \Delta r \rangle = 0, \tag{1.6}$$

where D is the diffusion coefficient or diffusivity, Δr is the vector displacement, and Δt is the observation time.

1.7.2 The Einstein relation

The Brownian motion of lipids and other components and complexes in membranes can be described using continuum models. The starting point for these models is the Einstein relation [93], which expresses the diffusion of a particle in a fluid as a function of the drag (λ) experienced by it:

$$\mathrm{D} = \frac{\mathrm{k_B T}}{\lambda} \tag{1.7}$$

with $\mathrm{k_B}$ denoting the Boltzmann constant and T the temperature. The lipid membrane is treated as a sheet of thickness h and viscosity η_m (Figure 1.12). Membrane components are approximated as cylinders of radius R embedded in the membrane, experiencing translational and rotational drag via interactions with the membrane and the bulk fluid (of viscosity η_b) on either side of the membrane. Stephan Block provides a good review of the various hydrodynamic models and their experimental verification [94].

The drag on the cylinder consists of a rotational and a translational component. Rotational drag is pertinent only to the orientation of the cylinder in the membrane, and for the purposes of this thesis, only the 2-dimensional translational motion of lipids in the membrane is considered.

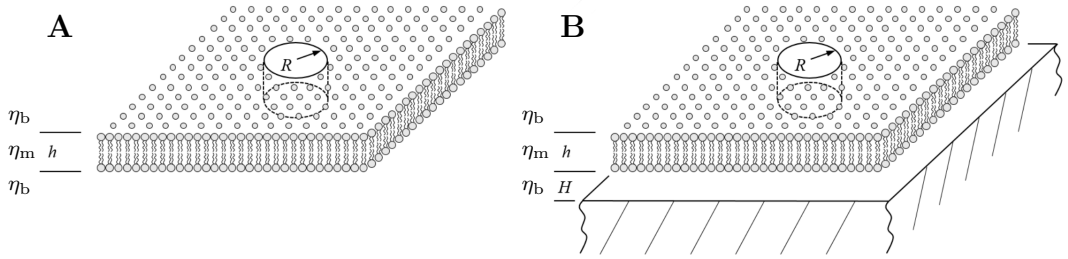

Figure 1.12: Models for diffusion in lipid membrane. Illustration of a cylindrical inclusion of radius R diffusing in (**A**) a freestanding bilayer of viscosity η_m and height h, in a fluid medium of viscosity η_b and (**B**) a bilayer supported by a solid substrate at a height H. adapted from [94].

1.7.3 The Saffman-Delbrück model

Saffman and Delbrück consider a freestanding membrane embedded in a medium of lower viscosity η_b (Figure 1.12 A) [16]. Their solution for calculating the translational friction coefficient λ_T gives

$$\lambda_T = 4\pi\eta_m h \left\{ \ln \frac{2}{\epsilon_{SD}} - \gamma \right\}^{-1} \tag{1.8}$$

with γ =0.5772, denoting Euler's constant, and ϵ_{SD} is a dimensionless parameter defined as

$$\epsilon_{SD} = \frac{R}{h} \frac{2\eta_b}{\eta_m} \tag{1.9}$$

The ratio R/ϵ_{SD} corresponds to the characteristic length scale of the membrane $l_m = \eta_m h/2\eta_b$, at which the bilayer starts to exchange momentum with the surrounding bulk medium. This model is generally applicable for 'freestanding' membranes, such as GUVs and BLMs, where the thickness of the bulk fluid on either side of the membrane is greater than l_m. However, in the GUV-SLB interface system, the distance between the GUV and the substrate is smaller than this length scale, hence a supported membrane model is appropriate.

1.7.4 Interactions of membranes with solid substrates: The Evans-Sackmann model

The model proposed by Evans and Sackmann considers the case of a bilayer supported on one side by a solid substrate [95]. It describes the weak frictional coupling between the membrane and the substrate in terms of an intrinsic frictional force which is dependent on the thickness H and the viscosity of the fluid layer between membrane and substrate. The translational drag coefficient for a cylinder of radius R diffusing in a membrane at a height H from a solid substrate is given by:

$$\lambda_{\mathrm{T}} = 4\pi\eta_{\mathrm{m}}h\left[\frac{1}{4}\epsilon_{ES}^2\left(1 + b_{\mathrm{p}}/b_{\mathrm{s}}\right) + \frac{\epsilon_{ES}K_1(\epsilon_{ES})}{K_0(\epsilon_{ES})}\right] \tag{1.10}$$

The ES model thus defines a new dimensionless coefficient ϵ_{ES} as

$$\epsilon_{ES} \equiv R\left(\frac{b}{\eta_{\mathrm{m}}h}\right)^{\frac{1}{2}} \tag{1.11}$$

where the $b = b_{\mathrm{s}} + b_{\infty}$ takes into account the total drag exerted on the membrane. b_{s} is the coefficient of frictional coupling between the membrane and the substrate, b_{∞} denotes the coupling between the membrane and the semi-infinite liquid on the other side of the membrane, and b_{p} is the friction coefficient between the moving cylindrical particle and the substrate.

K_0 and K_1 are modified Bessel functions of the second kind, orders zero and one. For a thin lubricating layer of fluid of height $H \ll l_{\mathrm{m}}$ between a membrane and a substrate, b simply reduces to the frictional coefficient b_{s}, and is given as

$$b_{\mathrm{s}} = \frac{\eta_{\mathrm{b}}}{H} \tag{1.12}$$

and the dimensionless coefficient, henceforth simply called ϵ, becomes

$$\epsilon \equiv R\left(\frac{\eta_{\mathrm{b}}}{\eta_{\mathrm{m}}hH}\right)^{\frac{1}{2}} \tag{1.13}$$

Further, the particle "self-drag" coefficient b_{p} can, particularly for lipids, be assumed to be equal to b_{s} [96], giving a simplified form of the Evans Sackmann model:

$$\lambda_{\mathrm{T}} = 4\pi\eta_{\mathrm{m}}h\left[\frac{1}{2}\epsilon^2 + \frac{\epsilon K_1(\epsilon)}{K_0(\epsilon)}\right] \tag{1.14}$$

Hydrodynamic treatments of membranes are idealisations of real membrane systems. They couple the 2-dimensional flow of membrane components to 3-dimensional flows in the bulk medium. While these models are in general agreement for simple systems involving generic attractive and repulsive forces, they still fail to take into account the physical properties of the substrate (such as roughness), the presence of pinning sites, and variations in membrane preparation [97]. Many of these models also tend to ignore inter-leaflet interactions and asymmetry. Therefore, these require a lot of empirical fitting parameters in order to correctly model biological phenomena. However, insofar as they are not used to model behaviour at molecular scales, they can be used as qualitative models of mesoscopic membrane properties [98].

1.7.5 Thermodynamic models of membrane interfaces

A classical model of cell adhesion was formulated by Bell, Dembo, and Bongrand, hence called the BDB model [99]. This model states that cell adhesion is governed by the competition between "specific" and "generic" interactions. The specific interactions occur between adhesion molecules, while the generic interaction refers to the classical forms of interaction between pure lipid membranes, the van der Waals attraction, the double-layer repulsion, the hydration repulsion, and the Helfrich entropic repulsion: the so-called "hydration forces" [100]. The BDB model posits the existence of two phase transitions consistent with the initiation of cell adhesion and a maximum contact state. Based on the minimisation of the free energy of the cell-cell system, the model proposes the existence of an equilibrium contact area (A), defined by an equilibrium linker density (N_b), and an equilibrium intermembrane separation(S):

$$\hat{\mathbf{S}} = \frac{1}{2}\left[L + \frac{kT}{\kappa\tau} + \sqrt{\left(L + \frac{kT}{\kappa\tau}\right)^2 + \frac{4kT}{\kappa}}\right] \tag{1.15}$$

where L is the optimal separation distance for which chemical potential is minimal;

κ is the spring constant for stretching the bridging molecules;

τ is the combined thickness of the polymer layers on both cells.

$$\hat{\mathbf{N}}_{\mathrm{b}} = 1/2 \left[N_{1\mathrm{t}} + N_{2\mathrm{t}} - \sqrt{(N_{1\mathrm{t}} - N_{2\mathrm{t}})^2 + 4\xi(\hat{\mathbf{S}})} \right] \tag{1.16}$$

where $\xi(\hat{\mathbf{S}})$ is a non-dimensional factor measuring the ratio of repulsion to binding;

$$\xi(S) = A_1 A_2 \Gamma(S)/kTK(S) \tag{1.17}$$

such that

$$\xi(\hat{\mathbf{S}}) < N_{1\mathrm{t}} N_{2\mathrm{t}} \tag{1.18}$$

$N_{1\mathrm{t}}$ and $N_{12\mathrm{t}}$ are total number of binders on either cell membrane

$$\hat{\mathbf{A}} = \frac{kT}{2\Gamma(\hat{\mathbf{S}})} \left[N_{1\mathrm{t}} + N_{2\mathrm{t}} - \sqrt{(N_{1\mathrm{t}} - N_{2\mathrm{t}})^2 + 4\xi(\hat{\mathbf{S}})} \right] \tag{1.19}$$

where $\Gamma(\hat{\mathbf{S}})$ is the energy required to overcome nonspecific repulsive forces per unit area.

$$\Gamma(S) = \frac{\gamma}{S} \exp\left(-\frac{S}{\tau}\right) \tag{1.20}$$

γ is a measure of the compressibility of the polymers.

While this seminal work provides a framework for understanding cellular adhesion, it does not account for close contact between the two membranes, as it assumes very large intermembrane repulsive forces which result in a simply tethered system separated by the uncompressed glycocalyx. This translates to an intercellular distance of ~15−40 nm.

The pioneering work of Sackmann and colleagues build upon this model, and provide experimental extensions in the form of receptor clustering, membrane pinning and membrane undulation forces. Weikl and Lipowsky discuss membrane adhesion in terms of *stickers* and *repellers* [101]. In this model, stickers and repellers are entropically sorted into domains, causing changes in the molecular ordering of the membranes. A summary of the experimental work on intermembrane interactions is give in the following sections.

1.8 Experimental models of membrane interfaces

Models of lipid bilayers differ by the degree of topographical constraint imposed upon them. In order to form interfaces, at least one membrane need to be relatively free to deform and undergo area changes. Simultaneously, the interface thus formed needs to be accessible to investigative techniques. Supported lipid membranes, being contained in a planar geometry, while also providing a fluid, cellular membrane-like surface [102], offer a suitable template for forming interfaces with 'free' membranes, which allow for the use of optical techniques to study the spatiotemporal behaviour of the interface dwellers. Two popular interface models are the fully artificial membrane-SLB interfaces —including interfaces formed between a GUV and an SLB, a floating/tethered membrane patch and an SLB, two or more vesicles —and hybrid live cell-SLB interfaces.

1.8.1 GUV-SLB interfaces

Interfaces formed by artificial vesicles and SLBs include those between GUVs and SLBs, burst GUV patches and SLBs, and membrane stacks formed via polymer-based linkers and spacers. Erich Sackmann pioneered the use of GUV-SLB model membrane interfaces, specially in the study of the mechanisms of cell adhesion, focussing on adhesion mediated by cell adhesion molecules (CAMs) (Figure 1.13). GUVs are doped with CAMs, while SLBs with reconstituted co-receptors or ligands to act as host and target cells, respectively. These provide the attractive forces required for the adhesion. The glycocalyx, which plays a moderating, repulsive role at these sites, is mimicked by functionalising lipids with polymer head groups. Albersdörfer *et al.* employ such a GUV-SLB system where the GUV was functionalised with lipopolymers to mimic the repulsive effect of a glycocalyx, and attractive forces were mimicked by incorporating biotinylated lipids in both membranes, coupled via streptavidin [40]. Observation of the interfacial membrane height profile using reflection interference contrast microscopy (RICM) revealed the formation of domains of tight adhesion separated by areas of low adhesion (marked by membrane undulations). These were

found to be in agreement with the BDB model. Bruinsma *et al.* and Kloboucek *et al.* expand upon this work, studying the effect of contact site A (csA) proteins on the control of cell adhesion on a GUV-SLB model incorporating polyethylene glycol (PEG) lipids and contact site A (csA) proteins as repellers and adhesive molecules [100, 103].

Receptor mobility and membrane deformation within the contact site have also been reported to influence adhesion strength [104]. Studies on GUV-SLB adhesion mediated by biotin-neutravidin linkers and E-cadherin linkers showed the existence of two competing adhesion states: an initial weak adhesion, followed by slower aggregation of the adhesion molecules into small, tightly bound clusters that coexist with the regions of weak adhesion [32]. In summary, Sackmann *et al.* propose that adhesion follows a two stage process of fast initial pinning followed by a slow lateral growth phase of adhesion patches [105]. The role of the glycocalyx is expanded upon, in that it is now thought to actively modulate the adhesive interactions via size-dependent exclusion, as well as by regulating the generic repulsive forces. Reviews such as those Sackmann and Smith [106] and Fenz and Sengupta [76] (and references therein) provide a useful summary of this remarkable body of work.

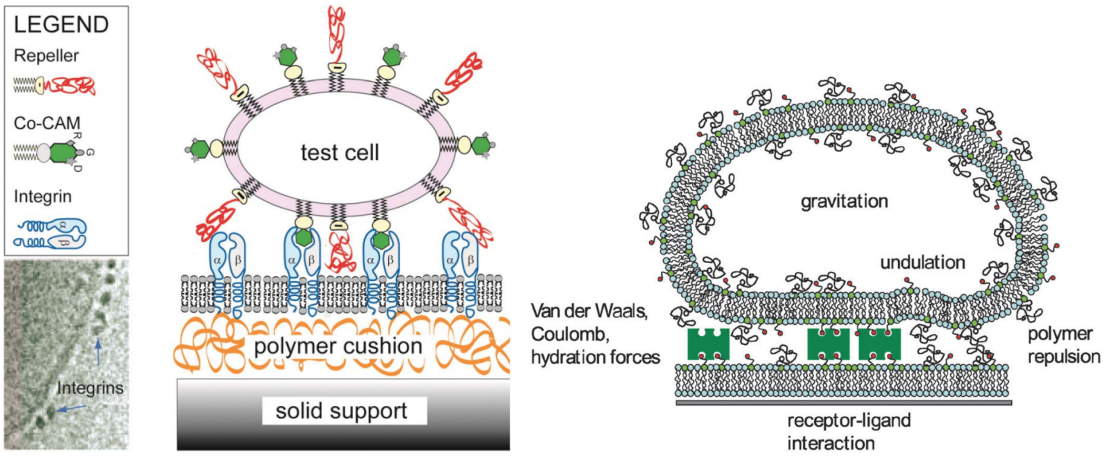

Figure 1.13: Adhesion-repulsion interactions studied using GUV-SLB interfaces. (Left) A model GUV-SLB system carrying the various participants involved in cellular adhesion. (Right) All the possible forces acting on two membranes at such a model interface. From [106] and [76].

1.8.2 Stacked membranes and other artificial models

A popular method of generating model membrane interfaces involves rupturing a GUV over an SLB. This model proves handy in the study of the physical properties of membranes at interfaces. Groves *et al.* employ fluorescent interference microscopy and FRET to study changes in membrane topology in a proximal environment [107, 63, 108]. They describe the confinement of water at the interface due to membrane fluctuations, and the existence of topographical domains of varying interface height. Work done in Steve Boxer's lab uses DNA-mediated interactions between membranes to initiate the formation and tethering for parallel bilayers [109, 110]. While this system was used to observe variable separation between the bilayers (Figure 1.15), it is unsuited for lipid diffusion analysis. At the edge of the stacked bilayer, the hydrophobic core is exposed to the aqueous environment. This is unstable, and leads to problems such as lipid mixing with the underlying SLB. Chapter 3 addresses this problem by employing a whole GUV tethered to a SLB by means of a similar DNA-tether mechanism to form interfaces. The continuity and deformability of the osmotically-modulated GUV avoids the formation of unstable bilayer edges.

Other examples of model membrane interfaces include McCloskey and Poo's interfaces between membrane-coated beads to show the diffusive trapping and accumulation of mobile ligands [111]. Aoki *et al.* use a gravitationally driven GUV adhesion system to study membrane area increase caused by hydroperoxidation of lipids [112]. Heath *et al.* assemble a multilayer lipid membrane system by rupturing vesicles onto existing supported lipid bilayers (SLBs) and supporting/separating the forming bilayer via poly l-lysine (PLL) electrostatic polymer linkers [113].

1.8.3 Hybrid live-cell-SLB interfaces

Another well studied example of interfacial processes in biology is the immunological synapse. The lateral arrangement of proteins at the immunological synapse, formed between T cells and antigen-presenting cells, is the initial step in activating the immunological response. Pioneering work by Michael Dustin and his associates report

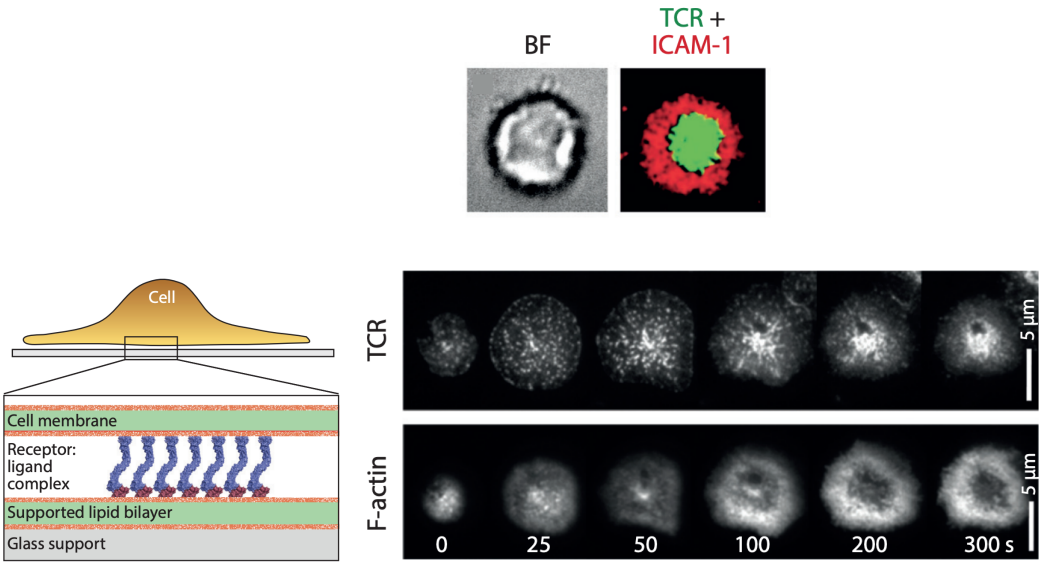

Figure 1.14: Hybrid cell-SLB interfaces. (Left) A model showing a typical interface model between a live cell and an SLB. From [102]. (Right) Spatial organisation of linkers and other membrane components visualised in the cell [114, 115].

on the spatial segregation of proteins at the immunological synapse formed at the interface between T cells and supported bilayers exhibiting an appropriate antigen [30]. This work demonstrates the 'bull's eye' arrangement, consisting of a central core enriched in T cell receptors, and pMHC (cSMAC), an intermediate ring enriched in adhesion molecules (pSMAC), and an outer ring containing receptors with large extracellular tails (Figure 1.14, right). Recently, Change *et al.* reported the local segregation of certain kinases and CD45 phosphatase at a nano scale, which initiates the formation of the immunological synapse [116]. Dustin *et al.* and Selvaraj *et al.* demonstrated the adhesion of cells via CD2-CD58 interactions by reconstituting the proteins into supported lipid bilayers [117, 118]. Cell spreading associated with adhesion mediated by ICAM-1 was also demonstrated on cell-SLB systems by Dustin and Springer [119]. Cell-SLB interfaces were successfully employed to measure 2D affinity and kinetic rates in contact areas [120]. For example the GPI-anchored form of CD58 was highly mobile in the supported planar bilayers, whereas the transmembrane form of CD58 was completely immobile. This laterally mobile form of CD58 was found to be 50-fold more potent than the immobile form of CD58 and stabilised adhesion faster [121, 122].

The interface models and techniques listed above provide platforms optimised for answering specific biological questions. However, they all involve certain common physical phenomena, the control of which are critical to life. Size is an important factor which determines the behaviour of proteins and other structures typically found at interfaces. For example, the formation of the immunological synapse proceeds by the size-based segregation of leukocyte surface molecules. Schmid *et al.* , using a combination of RICM and confocal microscopy, demonstrate the segregation of proteins based on the size of their transmembrane domains [31]. Conversely, as previously noted, crowding and clustering, such as in curvature sensing and scission processes, can determine the shape and eventual fate of membrane sections.

Secondly, the mediation of attractive and repulsive forces by proteins and glycocomplexes determines the nature of the interaction between membranes and substrates, as seen in the work of Sackmann *et al.* . Third, the hydrodynamic properties of the membranes and the surrounding aqueous media influence membrane topology as well as the diffusive properties of the membrane. The obstruction of membrane fluctuations at interfaces results in the development of repulsive Helfrich forces that also contributes to interesting effects in the confined geometry of the interface [123]. These combine to produce crucial topographical ordering of the interfaces [108].

These phenomena represent fundamental theoretical considerations in soft matter physics, and as is often the case, a bottom-up approach can prove very effective. As the oft-invoked LEGO® analogy suggests, DNA nanotechnology offers a popular, simple and elegant framework for the study of membrane properties.

1.9 DNA models of membrane components

1.9.1 DNA nanotechnology

DNA nanotechnology is a field focussed on the use of DNA as a structural component, rather than as an information carrier. This was first explored by George Church and Ned Seeman in the 1980s, who took inspiration from Holliday junctions [124] and other naturally occurring branched DNA structures to design lattices and arrays

[125, 126, 127]. The sequence specific binding and programmability of DNA base pairing, coupled with its mechanical properties, make DNA a versatile material to build structures from simple linkers to complex assemblies.

With its negatively charged backbone, DNA can bind to a lipid membrane by electrostatic interactions [128]. Further, the conjugation of DNA origami with lipophilic moieties such as cholesterol improves the ability of DNA origami to associate with and diffuse on lipid bilayers [129]

1.9.2 DNA-mediated membrane interactions

The use of DNA linkers in facilitating membrane interactions was pioneered by Höök *et al.* who used DNA tethers on SUVs to induce membrane fusion [74]. Steven Boxer's group described a method to tether DNA-functionalised vesicles to SLBs bearing complementary strands [130, 131], followed by DNA-mediated vesicle-vesicle interactions [132]. This method was also used to create DNA-tethered planar membranes on SLBs [109], with intermembrane height controlled by the length of the DNA linkers (Figure 1.15) [110]. The same group introduced a system to study membrane fusion mechanisms by using DNA hybridisation to help overcome the energetic cost of bringing apposing membranes in close proximity [133, 134, 135, 136]. Further, DNA-based tethers were also employed to mimic viral receptor binding [29].

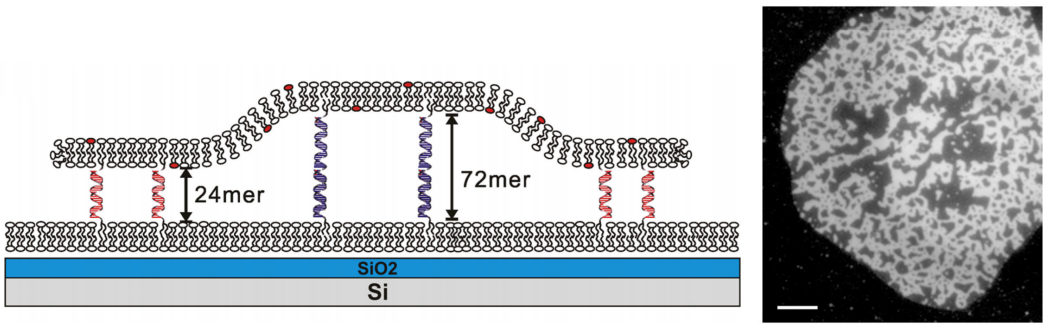

Figure 1.15: Height variation in membrane interfaces. In a GUV tethered to an SLB by DNA linkers of differing lengths, longer linkers were found to coalesce into domains of greater membrane separation, visible as dark regions in the interferometric image. From [110].

Beales and Vanderlick investigated the DNA-mediated binding of LUVs and GUVs and demonstrated the effects of salt concentration and DNA surface density on vesicle aggregation [137]. They also showed that the non-specific electrostatic binding of DNA to lipid membranes influences the interaction strength between the membranes, as well as the thermal dehybridisation of the DNA linkers [138].

Parolini *et al.* have previously employed a DNA-mediated adhesion system between GUVs [139], and between a GUV and an SLB [140] (Figure 1.17) . Adhesion strength is modulated by temperature changes and membrane geometry, which alters the formation of bridges (across the interface) and loops (on the same membrane). Using geometric and fluctuation analysis, they describe the resultant effects on mechanical properties of the membranes, such as changes in membrane tension and porosity in the GUVs. More recently, Taylor *et al.* created an artificial T-cell receptor using DNA linkers at cell-SLB interfaces [141].

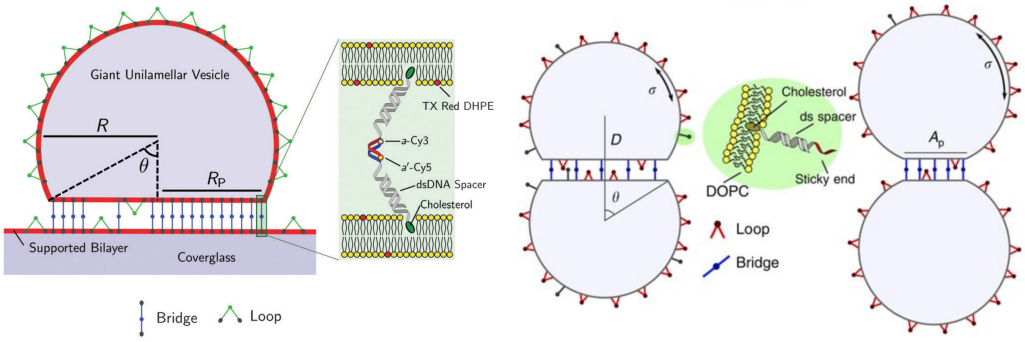

Figure 1.16: DNA mediated adhesion. Parolini *et al.* employ a system of DNA linkers and spacers to study the effect of temperature on GUV membrane tension. From [140].

1.9.3 DNA origami

In 2006, Rothemund put forward a revolutionary new strategy to create much larger and complicated DNA structures: DNA origami [142]. A single DNA strand, acting as a scaffold, can be 'folded' into a desired shape using hundreds of small oligonucleotide 'staples' which direct and stabilise the design. Developments in computer

aided strand design and arrangement have since rendered DNA origami an established technique for nanostructure assembly. Staples can be placed with nanometer precision (~6 nm) [142], and the origami structures can be functionalised with proteins, dyes, nanoparticles and lipids to improve its optical, chemical and electronic functionalities [143].

1.9.4 DNA origami on membranes

The conjugation of DNA origami with lipophilic moieties such as cholesterol improves the ability of DNA origami to associate with and diffuse on lipid bilayers [144, 145, 146]. This can be exploited to design of DNA structures that can form into long-range ordered assemblies on the lipid membrane [128, 147, 148]. DNA nanotechnology has thus been used to build simplified biomimetic models for the study of biological systems [149, 147, 143, 150, 151]. A popular design strategy is to use bundles of DNA helices arranged in a honeycomb lattice, as first described by Douglas *et al.* [152]. Recently, Xu *et al.* demonstrated the use of DNA structures as supports for the organisation of SNAREs leading in membrane fusion [153]. DNA origami can also be designed to directly model the role of proteins structure in membrane bending by mimicking the shape of existing proteins: Franquelim *et al.* have demonstrated an origami structure for membrane binding and sculpting [154]; Grome *et al.* have explored a spiral DNA origami scheme, inspired by dynamin, that can polymerise to induce membrane tubulation [155].

1.10 Single-molecule studies of lipid membranes

One major advantage of single-molecule tracking (or single particle tracking, or SPT) techniques over ensemble measurements is that it allows for the detection of subpopulations and rare dynamic events [156]. SPT has been employed to study anomalous diffusive behaviour in membranes, notably by Saxton *et al.* [157, 158, 159]. Kusumi *et al.* employed single molecule tracking to study anomalous diffusion phenomena arising from membrane compartmentalisation by actin, and developed the picket and

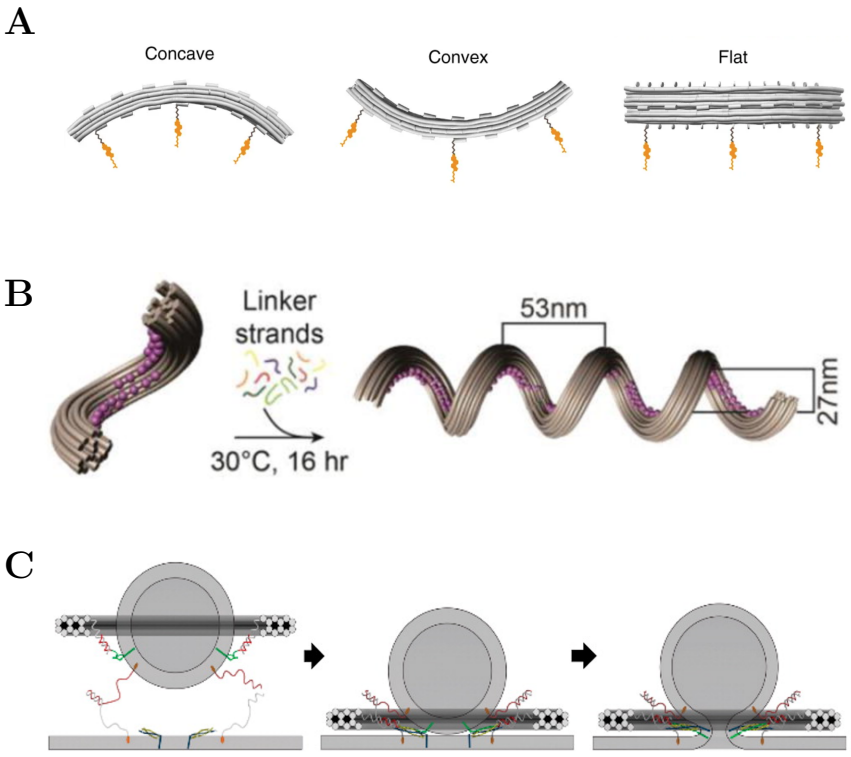

Figure 1.17: DNA origami on membranes. Recent examples of DNA origami mimics of membrane components. (**A**) Franquelim *et al.* describe a BAR-protein mimic that can shape membrane. adapted from [154]. (**B**) Grome *et al.* explore a spiral construct that can polymerise to induce tubulation. adapted from [155]. (**C**) Xu *et al.* employ a DNA-origami based scaffold that organises SNARE-proteins for membrane fusion. adapted from [153].

fence model of the cell membrane [35, 36]. Guo *et al.* compare lipid diffusion values obtained from SPT, FCS, ITIR-FCS (imaging-TIR FCS) and FRAP in GUVs and SLBs, and note that each technique is suited to specific conditions, geometries and label densities. They also go on use SPT to extract a range of diffusion coefficients which incorporate the biases of the other techniques [160].

There are many reports of single molecule tracking on plasma membranes [161, 162], but the complex topography of cells makes interpretation of the results difficult. Moreover, this also presents challenges of delivering sufficient laser power, and in correlating localisation of fluorophores and target molecules. Therefore, traditional SPT is carried out on 2-d (flat) membranes. Sharonov *et al.* compare lipid diffusion in GUVs and SLBs under similar conditions using low-angle-epi-illuminated, single-

molecule tracking of fluorescent proteins bound to the lipids [163]. Woodward *et al.* and Coker *et al.* study the effects of membrane topology on lipid diffusion and sorting [164, 165].

Two studies employ single-particle tracking to characterise systems involving bilayer stacks. However, both these studies look at the mobility of transmembrane proteins in the second (upper) bilayer. Murray *et al.* use SPT to characterise a double bilayer system formed by fusing LUVs on a pre-formed SLB. They found that protein mobility on the second bilayer was not significantly improved [166]. Wang *et al.* rupture GUVs onto SLBs presenting a PEG-cushion, reporting increased mobilities for lipids and syntaxin-1A transmembrane proteins [167].

The work discussed in this thesis explores two contrasting applications of DNA nanotechnology in membrane studies. The first project utilises the complementarity of simple DNA constructs to mediate attractive and repulsive interaction between a GUV and an SLB. While being acutely wary of claiming novelty, it is believed that this thesis presents for the first time, a single particle tracking study of multiple components of a model membrane junction. It provides a proof-of-concept for a holistic single-molecule study of membrane interfaces− allowing for simultaneous measurements of both the membranes as well as the intermembrane components.

The second project discusses the design of a DNA origami structural mimic of the membrane protein clathrin, and its programmable ability to form long range assemblies and induce membrane deformation. Finally, the conclusion presents a summary of the learnings, and offers a roadmap, to-do lists and wish lists for future experimental work.

Chapter 2

Materials and Methods

This chapter describes the materials used in this work, along with techniques and protocols employed. The two lipid bilayer models, GUVs and SLBs, are described, along with the protocols for producing them.

2.1 Materials

Unless otherwise stated, all chemicals and solvents were of analytical grade and used without further purification.

2.1.1 Lipids

1,2-Dioleoyl-*sn*-glycero-3-phosphocholine (DOPC) was purchased from Avanti Polar Lipids (Alabaster, USA) and from Lipoid GmbH (Steinhausen, Switzerland). Atto-488-1,2-dioleoyl-*sn*-glycero-3-phosphoethanolamine (Atto488-DOPE) and Atto647N-1,2-dipalmitoyl-*sn*-glycero-3-phosphoethanolamine (Atto647N-DPPE) were purchased from ATTO-TEC (Siegen, Germany). TexasRed-1,2-dipalmitoyl-*sn*-glycero-3-phosphoethanolamine (TexasRed DPPE) was purchased from Thermo Fisher Scientific(Waltham, USA).

DOPC was dissolved in chloroform to 25 mg mL^{-1} and stored at -20° C for up to a month during use. For single-molecule experiments, fluorophore stocks were made to 10 ng mL^{-1} in a 9:1 mixture of chloroform and methanol.

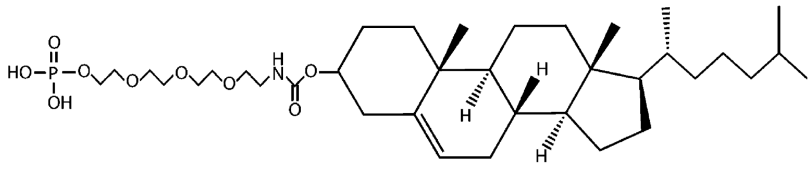

Figure 2.1: Cholesterol with tetraethyleneglycol (TEG) spacer. Cholesterol-TEG attached to the DNA oligo via the phosphate group at the 5' end of the backbone allows the DNA to interact with membranes. From [168].

2.1.2 GUV electroformation

Indium Tin Oxide (ITO) coated glass slides were purchased from Sigma Aldrich (St. Louis, USA) (70-100 $\Omega\,\mathrm{cm}^{-1}$) and Delta Technologies (Loveland, USA) (5-15 $\Omega\,\mathrm{cm}^{-1}$). Leads were attached to the ITO coated sides via adhesive copper tape (No. 1181, 19mm) from 3M (Maplewood, USA). A PDMS spacer was made using the Sylgard 184 kit from Sigma Aldrich (St. Louis, USA). A function generator (Model 4040A, BK Precision, Yorba Linda, USA) was used to apply an AC field. Solution was injected into the electroformation chamber by using a 1 mL syringe fitted with a 23 gauge (blue, 0.63 mm outer diameter) needle. Needles with a wider bore (19 gauge, cream, 107mm outer diameter) were used for GUV extraction. Needles and syringes were procured from Beckton Dickinson (Franklin Lakes, USA).

2.1.3 DNA spacers

DNA oligonucleotides were purchased from atdbio (Southampton, UK). Oligonucleotides without any modifications were obtained after HPLC purification, while those with cholesterol-TEG anchors (Figure 2.1) after PAGE purification. Oligonucleotides with Atto647N fluorophore attached were obtained after purification by Double HPLC.

Double stranded DNA with sticky ends were annealed on a Mastercycler Thermocycler (Eppendorf, Germany).

Specific sequences used in experiments are listed in their individual chapters.

2.1.4 DNA origami

DNA origami structures used in the clathrin mimic experiments were prepared and characterised by Dr. Céline Journot at the Department of Physics, Oxford. The origami were functionalised with cholesterol to allow for specific interaction with cell membranes. Each construct was also tagged with Atto647N fluorophore for fluorescent microscopy purposes. Origami were folded and purified in 1× TE buffer (1 mM Tris and 5 mM EDTA) with 12 mM $MgCl_2$. Tris(hydroxymethyl)aminomethane (Tris) was purchased from Sigma Aldrich (St. Louis, USA). Anhydrous tetrasodium Ethylenediaminetetraacetic (EDTA) was obtained from Thermo Fisher Scientific (Waltham, USA). $MgCl_2$ was purchased from Sigma Aldrich (St. Louis, USA). The design of the DNA origami structures is discussed in Chapter 4, and the schematics are shown in Appendix C.

2.1.5 Other materials

Chloroform, propan-2-ol and methanol (all HPLC grade) were purchased from Sigma Aldrich (St. Louis, USA). Sucrose and NaCl were purchased from Sigma Aldrich (St. Louis, USA). Standard phosphate-buffer saline (PBS) tablets (137 mM NaCl, 2.7 mM KCl, 10 mM Na_2HPO_4, 1.8 mM KH_2PO_4 — "1× PBS") were also purchased from Sigma Aldrich. Decon-90 surfactant was purchased from VWR International (Lutterworth, UK).

In this work, water refers to ultra-pure deionised water (18.2 MΩ cm resistivity at 25° C) purified on a Direct-Q® 3 UV system (Merck Millipore, Billerica, USA).

2.2 Model membranes

2.2.1 Small Unilamellar Vesicles (SUVs)

Liposomes were formed by hydrating a dried lipid film. 2 mg of DOPC lipid stock (50 µL of 10 mg mL^{-1} chloroform solution) was aliquoted into a 15 mL glass vial, dried under Nitrogen gas and subsequently placed in a vacuum desiccator for a minimum of two hours to remove all traces of solvent. The dried lipid film was then hydrated

with 2 mL of deionised water, and the vial was vortexed. This facilitates the detachment of the film from the walls of the tube, and forms a suspension of polydisperse multilamellar vesicles [62]. The suspension was then sonicated with a probe sonicator (Vibracell VCX130PB with CV188 tip, Sonics & Materials, Newtown, USA). The glass tube was placed in an ice bath and sonicated at 25% power for 10 minutes, or until the suspension was clear. The suspension was then centrifuged at 14000 rpm for 3 minutes to sediment any titanium particles transferred from the sonicator, and the supernatant was retained. SUV preparations were stored at 4° C for up to 72 hours. The sonication tip was washed by sonicating in methanol, followed by deionised water, for 3 minutes and then rinsing with deionised water before and after each use.

2.2.2 Supported Lipid Bilayers (SLBs)

SLBs were prepared by the fusion of SUVs on glass coverslips, as first described by Brian and McConnell in 1984 [62]. Glass coverslips were rigorously cleaned by first abrading the surface with Decon-90 detergent solution using a gloved finger. This was followed by a stepwise bath sonication protocol involving washing in Decon-90, water and propan-2-ol for 20 minutes in each. The coverslips were stored in deionised water. Immediately before use, they were dried under Nitrogen, and treated with oxygen plasma for 3 minutes in a Femto low pressure plasma system (Diener Electronic, Ebhausen, Germany).

Wells were formed on the coverslip using either high-vacuum grease (Dow Corning, USA) or repurposed commercial perfusion chambers (Coverwell, Grace Bio-Labs, USA). Between one and four wells of ~100 µL volume were made on the coverslips, but care was taken to ensure that there was no transfer of material between individual wells. 50 µL of SUV stock solution were diluted with 50 µL of standard 1× PBS solution and applied to each well. Upon incubation for 15 minutes, a lipid bilayer was formed on the coverslip enclosed by the well. Vesicles rupture occurred against the glass surface under the effect of osmotic shock and the hydrophilicity of the glass. Excess vesicles were removed by rinsing the bilayer with 2 mL of degassed deionised

water (100 µL per rinse), followed by rinsing with the dilution buffer (NaCl of differing concentrations or standard 1×PBS). Finally, the dilution buffer was similarly exchanged for the experimental buffer (2 mL in 100 µL rinses of NaCl of differing concentrations or standard (1×) PBS, according to the experiment).

2.2.3 Giant Unilamellar Vesicles (GUVs)

Giant unilamellar vesicles (GUVs) were produced by the electroformation technique [84, 169]. Lipids in chloroform (50 µL, 1 mM DOPC, or 0.01 mol% ATTO488-DOPE, 99.99 mol% DOPC) were spread on two clean, ITO-coated conductive glass slides and dried in a vacuum desiccator for 30-60 min. This aids in the formation of ordered lipid films on the electrode surface (Figure 2.2) [170]. A chamber of ~1 mL volume was formed between the two ITO slides by sealing them together with a custom-made rectangular PDMS spacer. Electrodes were connected to the two conducting sides of the slides via adhesive copper tape. 1 mL of sucrose at required concentration was injected into the chamber between the two electrodes and a square wave potential was applied with an rms amplitude of 1.3 V and a frequency of 10 Hz for 90 minutes. The electroformation setup was placed inside an INCU-Line® IL 10 incubator from VWR International (Lutterworth, UK) so that the electroformation was carried out at a temperature of 60° C in order to ensure a highly mobile lipid film [171]. GUVs form inside the chamber and were collected using a wide bore needle (19 gauge) to prevent shearing.

NB: In early experiments ITO slides were cleaned and reused for economic reasons. The cleaning protocol involved sequential bath sonication in chloroform, propan-2-ol and deionised water for 20 minutes in each. (A previously used step included sonicating in Decon 90, but this was discarded due to difficulties in fully washing off the detergent from the ITO surface, leading to a drop in GUV yield). It is to be noted that surface conductivity diminishes with the wearing off of the ITO coating, and slides with resistivity greater than 200 Ω cm^{-1} were discarded. In later experiments, a newfound generosity allowed for the use of fresh ITO slides for each batch of GUV electroformation.

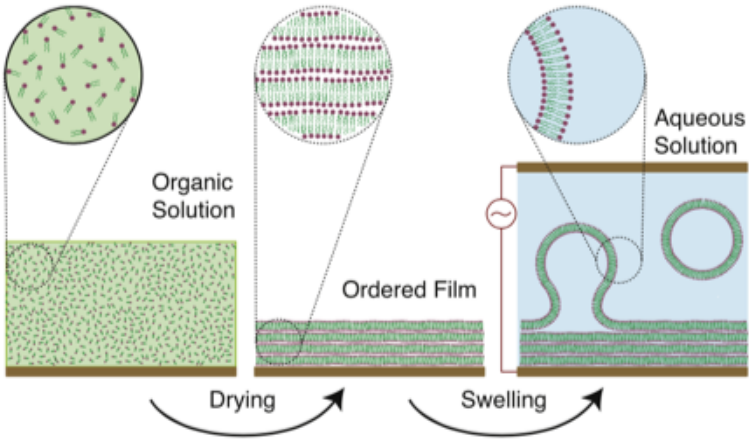

Figure 2.2: GUV Electroformation. GUVs swell from ordered lipid films in an electric field. Adapted from [170].

2.2.4 GUV-SLB interfaces

GUV-SLB interfaces were prepared by density sedimentation of GUVs onto SLBs. GUVs filled with sucrose at required concentration were introduced to an SLB-containing well filled with experimental buffer. The concentration of the sucrose and buffer were selected such that the density of the GUV interior was greater than the external buffer, while the osmolarity was kept equal or lower. For the interface experiments, GUVs were electroformed in 100 mM or 500 mM sucrose and introduced to SLBs hydrated by NaCl solution. Sometimes, glucose was added to vary the osmotic gradient across the GUV while maintaining the ionic gradient. (For the DNA origami experiments, GUVs were electroformed in 52 mM sucrose solution in order to maintain osmotic balance with the 1× TE + 14 mM $MgCl_2$ buffer.) The GUV drifts to the bottom, and rests on the SLB. The SLB acts as a passivating film that prevents the GUV from bursting due to interactions with the coverslip. The GUV now assumes a semi-flattened shape, and the diameters of the contact region and the rest of the GUV are determined by the osmotic difference.

2.2.5 DNA interactions with membranes

For experiments involving DNA interactions with GUVs, a small aliquot of DNA (oligos or origami) suspension was introduced to a 5 µL aliquot of GUV suspension.

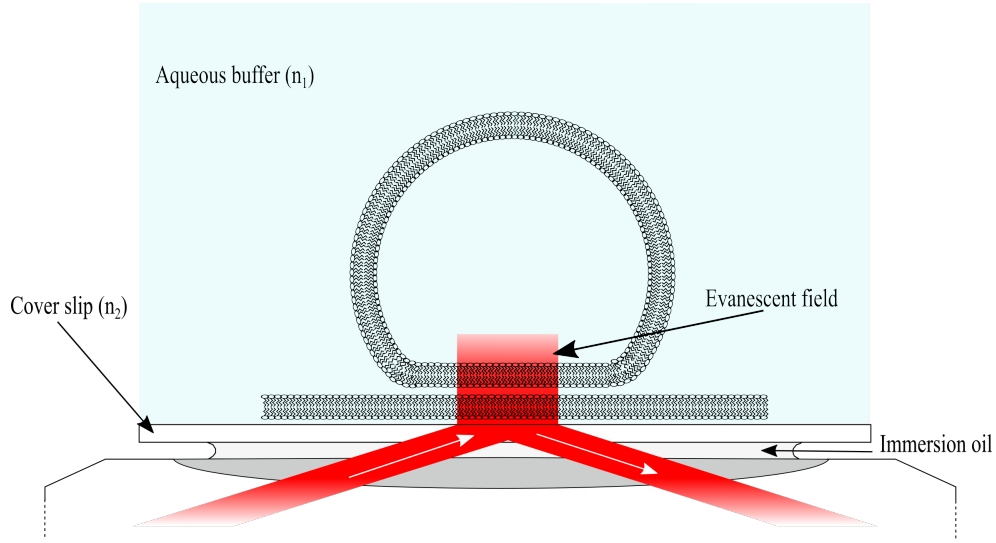

Figure 2.3: Interface TIRF microscopy working principle. The total thickness of a GUV-SLB interface is smaller than the height of the evanescent field generated, allowing for simultaneous single-molecule tracking in both membranes.

The mixture was allowed to incubate for at least 10 minutes, and the DNA constructs tethered to the membranes via insertion of cholesterol groups into the outer leaflet of the membranes [129].

For DNA triskelion polymerisation experiments, the origami was first tethered to the GUVs as described above, followed by the addition of 10× concentration of polymerising staples. The DNA-decorated GUVs were then introduced to the experimental chamber containing the SLB.

For DNA-SLB interactions, the DNA was introduced directly into the SLB chamber, and allowed to incubate for at least 10 minutes. This was followed by washing the SLB with the experimental buffer as described previously. This ensures that DNA strands adhered to the SLB via non-specific interaction with the glass substrate are eliminated. DNA bound to the membrane via cholesterol anchors continue to be bound after washing.

2.3 Microscopy

2.3.1 Single-molecule TIRF microscopy

Total internal reflection fluorescence (TIRF) microscopy was used to illuminate fluorescent molecules within ~100 nm of the substrate, allowing for simultaneous imaging regions of SLB and GUV bilayers (Figure 2.3), and the positions of these markers were tracked over time. Experiments were performed on an Eclipse Ti-E inverted microscope (Nikon, Tokyo, Japan), set up as detailed in Figure 2.4. For Atto647N, a 642 nm, 60 mW continuous wave laser (Stradus 642-110, Vortran, Sacramento, USA) was focussed at the back focal plane of the objective lens (Apo TIRF 60× NA 1.49 oil immersion objective, Nikon, Tokyo Japan) such that the beam was totally internally reflected at the coverslip-sample interface. For TIRF microscopy, an incident power of 0.34 mW at the sample was adequate to resolve individual fluorophores. Atto647N is excited and fluoresces with a peak intensity of 664 nm (red). A combination of dichroic and band pass filters are used to ensure than only the fluorescent signal is imaged on an EM-CCD camera (iXon+ 860, Andor, Oxford, UK). An electron multiplying (EM) gain setting of 300 was selected. Up to 2000 frames were recorded at 50 Hz (20 ms exposure time) and saved in the Tagged Image File Format (*.TIF).

For Atto488-labelled species, a 474 nm CW laserStradus 473-80, Vortran, Sacramento, USA) is used, and the dye fluoresces with peak intensity at 520 nm. For Atto647N-labelled species, a 642 nm CW laserStradus 473-80, Vortran, Sacramento, USA) is used, and the dye fluoresces with peak intensity at 664 nm.

2.3.2 TIRF illumination improvement

In a typical microscopy experiment, the angle of incidence of the illumination beam at the slide-sample interface is lower than the angle of refraction in the lower refractive index aqueous sample solution- that is, the beam is transmitted into the sample. At the *critical angle*, the refracted beam is tangential to the interface− it is not transmitted into the medium. In TIRF microscopy, the illumination beam is directed at the sample such that the angle of incidence is greater than the critical angle,

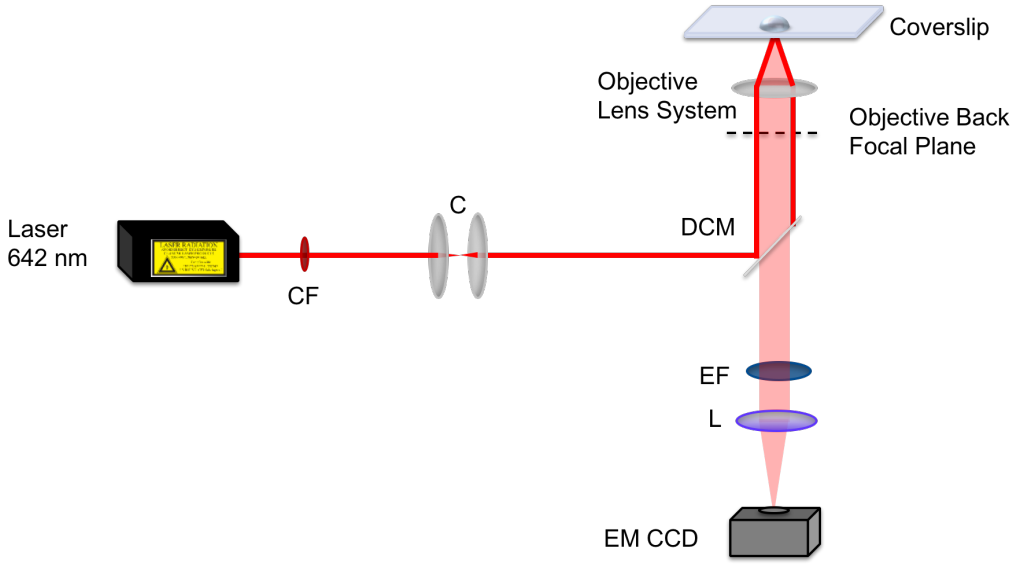

Figure 2.4: Microscope setup for TIRF experiments. CF= Clean up filter 642/10 nm, **C**= collimating telescope, **DCM**= dichroic mirror Di01-R405/488/532/635 nm Quad band, **EF**= emission filter 647 nm notch filter, **L**=lens, **EM-CCD**= electron-multiplying CCD camera

causing total internal reflection of the beam. This leads to the generation of an evanescent plasmonic field perpendicular to the plane of incidence and into the sample medium. However, defects in the optical components in the illumination path lead to scattering and stray diffraction that affects the power density in the evanescent field. The effect of this stray illumination is diminished by using a pair of oscillating galvanometer scanning mirrors, or galvo mirrors (Thor Labs, Newton, USA), that translate the beam in a circle around the axis of the objective. This 360° scanning of the illumination spot at the sample ensures a homogeneous power distribution in the evanescent field.The galvo mirrors were driven by two separate phase-locked function generators (DG 1022, Rigol, Reading, UK).

Tracks from single-molecule fluorescence videos were collected using the TrackMate plugin for FIJI [172]. Mean Square Displacement (MSD) analysis was performed on MATLAB using a Particle Analysis Tool developed by Dr. Matthew R. Cheetham.

2.3.3 Fluorescence Recovery After Photobleaching (FRAP)

In the experiments detailed in this thesis, the SLB is used as an active component rather than as a passivating surface. The fluidity of an SLB is defined by the long scale diffusion of the constituent lipids, and this is evaluated by measuring fluorescence recovery after photobleaching (FRAP) as described by Axelrod *et al.* [173]. FRAP is carried out on a SLB made of DOPC with 1 mol% TexasRed DPPE. A portion of the SLB is photobleached by illuminating it with a 532 nm laser (Oxxius, Lannion, France) at 25 mW incident power for 5 seconds. The geometry of the bleached spot is controlled via the microscope's aperture diaphragm. Following exposure, the recovery of fluorescent intensity is recorded over time using a lower power illumination. A custom program was developed by Dr. Matthew R. Cheetham to fit the data to the fractional recovery curve $f(t)$ at time t for a uniform circular illumination spot [174].

$$f(t) = \exp\left(-2\tau_D/t\right)\left[\mathbf{I}_o\left(2\tau_D/t\right) + \mathbf{I}_1\left(2\tau_D/t\right)\right] \tag{2.1}$$

Here, $\mathbf{I}_o$ and $\mathbf{I}_1$ are modified Bessel functions of the first kind, $\tau_D = R^2/4D$ is the characteristic diffusion time, R is the radius of the circular beam and D is the diffusion coefficient. A rigorous coverslip preparation protocol ensures mobile SLBs.

2.3.4 Two channel epifluorescence microscopy

For the DNA origami work, simultaneous two colour excitation was performed with the illumination set up for epifluorescence. The 473 nm laser was passed through a clean up filter (473/10 nm (MaxDiode, Semrock) and collimated. The 642 nm laser was passed through a 642/10 nm clean up filter (BrightLine, Semrock) and collimated. The beams were then combined using using a blue/red dichroic mirror (605 nm Edge BrightLine, Semrock). For epifluorescence microscopy, the galvo mirrors were turned off, and the beam strikes the sample normal (90°) to the coverslip. A quad dichroic (Di01-R405/488/532/635, Semrock, Rochester, USA) was used to direct both wavelengths towards the sample, and the fluorescence signals from both

fluorophores towards the detector. The sample contains Atto488 DPPE, which fluoresces with peak intensity at 520 nm, and Atto647N, which fluoresces with a peak intensity at 664 nm.

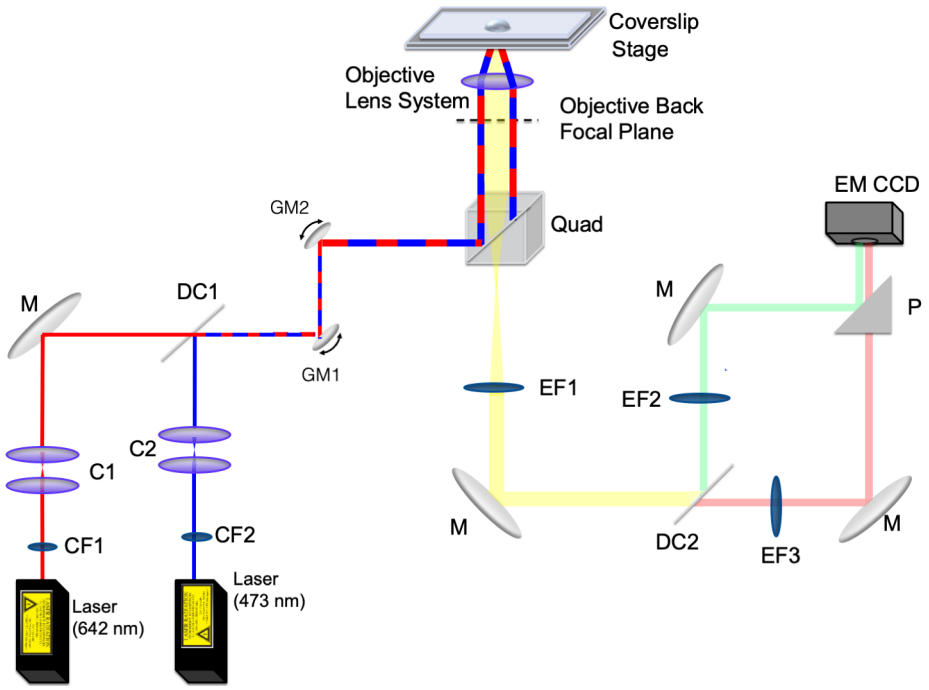

Figure 2.5: Microscope setup for dual-channel fluorescence experiments In addition to the optical components in Figure 2.4, dual channel microscopy requires **CF2**= blue clean up filter 473/10 nm, **DC1**= a dichroic mirror 605 nm Edge BrightLine, to combine the red and blue beams. **GM1**, **GM2**= galvanometer scanning mirrors homogenise the power density of the incident beam across the sample. **DC2**= 660 nm edge BrightLine dichroic beam splitter is mounted on an OptoSplit cube to separate the emitted wavelengths. Another pair of emission filters, **EF2**=550/88 nm and **EF3**= 680/42 nm are used to further improve the signal to noise ratio.

A 647 nm notch filter (ZET647NF, Chroma, Vermont, USA) was employed to further attenuate the red excitation beam. An Optosplit module (Cairn Research, Faversham, UK) was used to isolate the signal into two separate channels. The signal was split according to the constituent wavelengths using a Blue/Red Dichroic beam splitter (FF660-Di02, Semrock, Rochester, NY), and an additional set of emission filters (550/88 nm for green emission and 680/42 nm for red emission) was employed to remove stray wavelengths. The emissions from both fluorophores were then captured simultaneously on the EM-CCD camera. This setup is detailed in Figure 2.5

2.3.5 Image acquisition

2.3.6 Background subtraction

Image stacks were processed using the open source software package FIJI [175]. For single-molecule tracking, a background image was produced by calculating the median value of the intensity of each individual pixel (Figure 2.6 B). Immobile 'spots' significantly increase the median intensity values of the pixels which represent their position, while mobile spots do not significantly affect pixel median values. The stacks were then normalised by dividing each frame by the background image. This results in immobile features being subtracted, mobile features being retained, and normalised intensity variations in illumination (Figure 2.6 C).

2.3.7 Single-molecule tracking

Single-molecule tracking is dependent on localisation precision, so a sufficiently detailed point spread function and good contrast (signal to noise ratio) is essential. A relatively small and photostable fluorescent dye with a narrow emission spectrum, and appropriate laser power densities for the exposure times used (20 ms in the experiments presented) are some of the experimental conditions which ensure good spot quality and reliable tracking. Once the stacks of single-molecule tracks were collected and normalised, tracks were analysed using the TrackMate plugin in FIJI [172]. Spot diameter and intensity threshold were assigned manually, and the plugin identified particles using a Laplacian of Gaussian (LoG) filter (Figure 2.6 **D**) [176, 177]. Changes in the spatial coordinates of a spot between frames were calculated using a simple linear assignment problem (LAP) algorithm [178], and tracks were generated by linking these points together. Maximum linking distance, or the maximum distance that can be considered part of a track, was typically set to 5 pixels. In order to account for gaps caused due to imaging artefacts, maximum gap closing distance was also set to 5 pixels, and frame gap of up to 1 frame was allowed. These values were used for a pixel size of 390 nm and frame time of 20 ms. (The experiments were carried out in frame-transfer mode, and the frame time was set equal to exposure time.) The plugin

produced a collection of tracks, containing the space-time coordinates of each point in a track (Figure 2.6 **F**). This data was saved in XML format for further analysis using MATLAB.

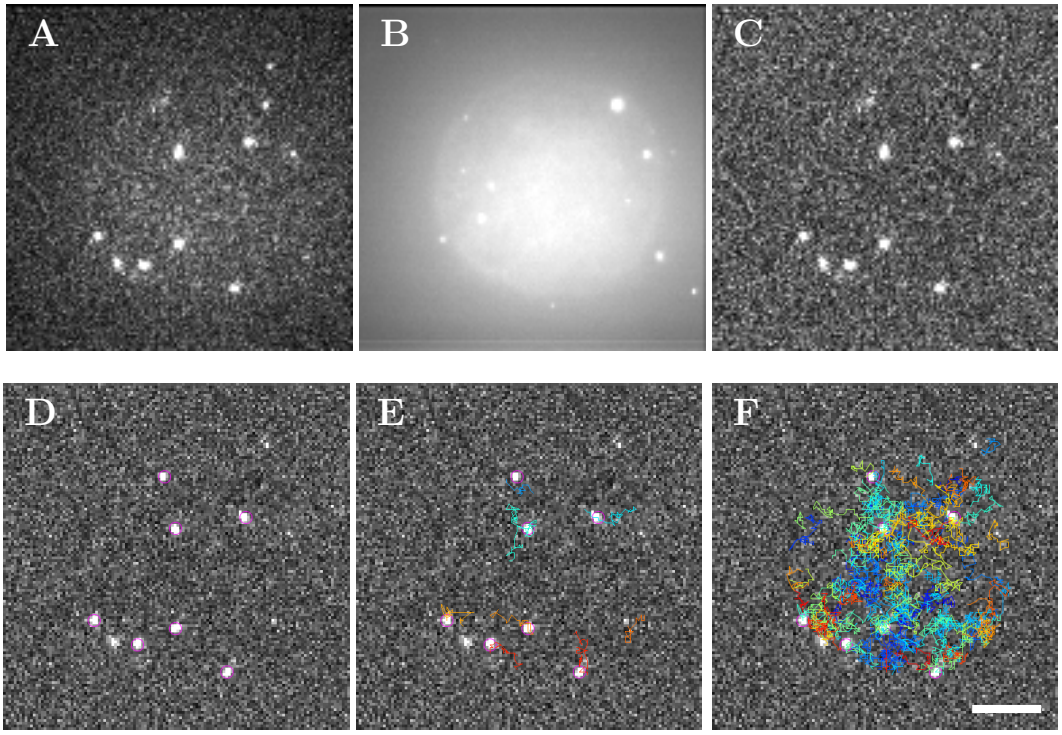

Figure 2.6: Single particle tracking in GUVs In order to calculate diffusion coefficients, MSD values are first obtained via particle tracking. (**A**) The raw image data is corrected for uneven illumination and to eliminate static artefacts. (**B**) A background image is produced via a median z-projection. Each frame is then divided by the background image. (**C**) The normalised stack has a 'flattened' illumination profile and static spots are eliminated. (**D**) Spot selection and tracking are performed using TrackMate. Spot sizes and intensity thresholds are entered manually, and the plugin identifies all good quality (high contrast) spots using a Laplacian of Gaussian (LoG) filter. (**E**) Linking parameters are manually entered, and tracks are generated using a simple Linear Assignment Problem (LAP) algorithm. The tracks depicted here show particle trajectories within ±20 frames of the current frame. (**F**) A representative image showing all the tracks obtained from this image stack. Scale bar 10 µm.

2.3.8 Diffusion analysis

The single-molecule tracks were used to perform diffusion analysis. Mean square displacements were calculated from spot coordinates for tracks at least 20 frames long at 20 ms time intervals, and diffusivities were calculated as in Equation 1.6.

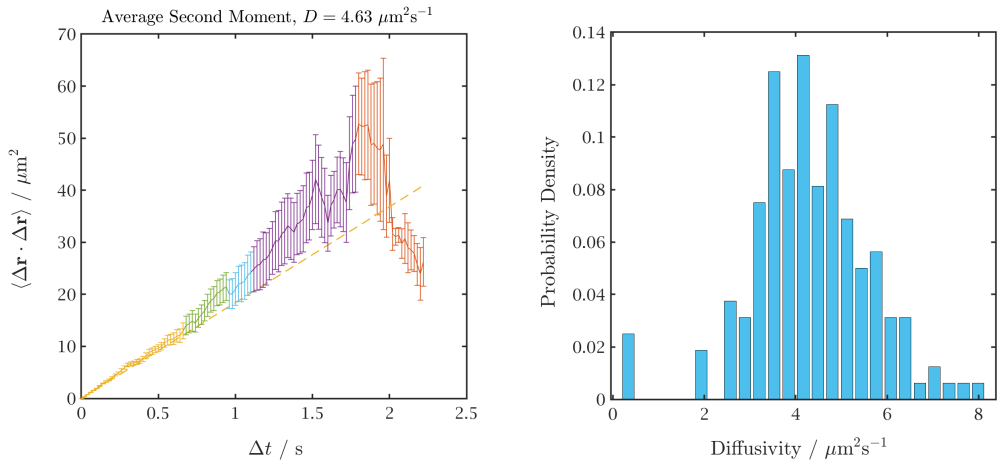

Figure 2.7: MSD vs Δt and diffusivity MSD vs Δt plotted for different lag times. Diffusion coefficients are calculated for all lag times, and the mean value is selected.

The displacements in x and y for a fixed observation time Δt were calculated as:

$$\begin{aligned} \Delta x_i(\Delta t) &= (x_{i+1} - x_i) \\ \Delta y_i(\Delta t) &= (y_{i+1} - y_i) \end{aligned} \tag{2.2}$$

where i is the index of the frame in the image stack.

Mean square displacement was calculated as the average of the squares of the displacements corresponding to a given lag time Δt:

$$\Delta \mathbf{r}_i{}^2 = \Delta x_i{}^2(\Delta t) + \Delta y_i{}^2(\Delta t) \tag{2.3}$$

$$\left\langle (\Delta r(\Delta t))^2 \right\rangle = \frac{1}{n} \sum_{i=1}^{n} \Delta r_i^2(\Delta t) \tag{2.4}$$

Diffusion coefficients were then calculated as the time-averaged mean squared displacement using a program written by Dr. Matthew Cheetham on MATLAB, shown in Appendix B.3 [165]. Figure 2.7 shows mean squared displacement vs Δt for different lag times. A histogram is plotted for these values and the mean is chosen, after ensure that D is invariant for lag times comparable to mean track durations.

2.4 A brief history of prior work

The aims of this DPhil have remained essentially the same since the beginning—develop techniques based on membrane-DNA interactions to understand aspects of membrane biophysics. While this thesis covers only the experiments that could be said to have produced 'results', many lessons were learned during the projects that didn't lead to any exciting results. This sections details the skills developed, work done, and lessons learned in the first two years, and how these led to the work presented here.

The very first project was envisioned as a DNA-based 'switch' to modulate lipid phase separation. Model bilayer membranes with multiple lipid species can be modulated to separate into phases, and even phases with micron-sized domains that can be studied using optical microscopy [4]. Phases differ in the packing order and diffusivity of the lipids contained in them. For example, in ternary lipid mixtures of a saturated lipid (high transition temperature, T_m, between ordered and disordered phases), an unsaturated lipid (low T_m) and a sterol such as cholesterol, one or more phases can be observed when the temperature is cycled. The three commonly observed phases are the solid ordered or gel phase S_o, characterised by a high order parameter and low diffusivity; liquid ordered L_o, of intermediate order and diffusivity; and liquid disordered L_d, characterised by a low order parameter and high lipid diffusivity. Figure 2.9 shows GUVs made from different compositions of DOPC, DPPC and cholesterol, exhibiting $L_o - L_d$ phase separation in a range of phase morphologies.

Vesicles were prepared using two primary techniques: agarose-lipid hybrid film swelling [85] and electroformation [84]. The agarose-lipid film swelling technique involves the swelling of dried films of agarose and lipids by an aqueous solution to produce GUVs. While the technique allowed for the growing of vesicles (of $10-130$ µm diameters) in physiologically relevant pH and buffer conditions, it had the drawback of encapsulating agarose within the vesicles, which might affect lipid diffusion and phase mobility. More importantly, as the lipids were embedded in a network of ultra-low melting temperature agarose, it was difficult to control the temperature and the diffusion of lipids in the hybrid film. This resulted in multiple phase morphologies

being produced in a single batch of vesicles formed by this method (Figure 2.9 A−C). Hence, electroformation at elevated temperatures became the preferred method for producing GUVs for the rest of the DPhil.

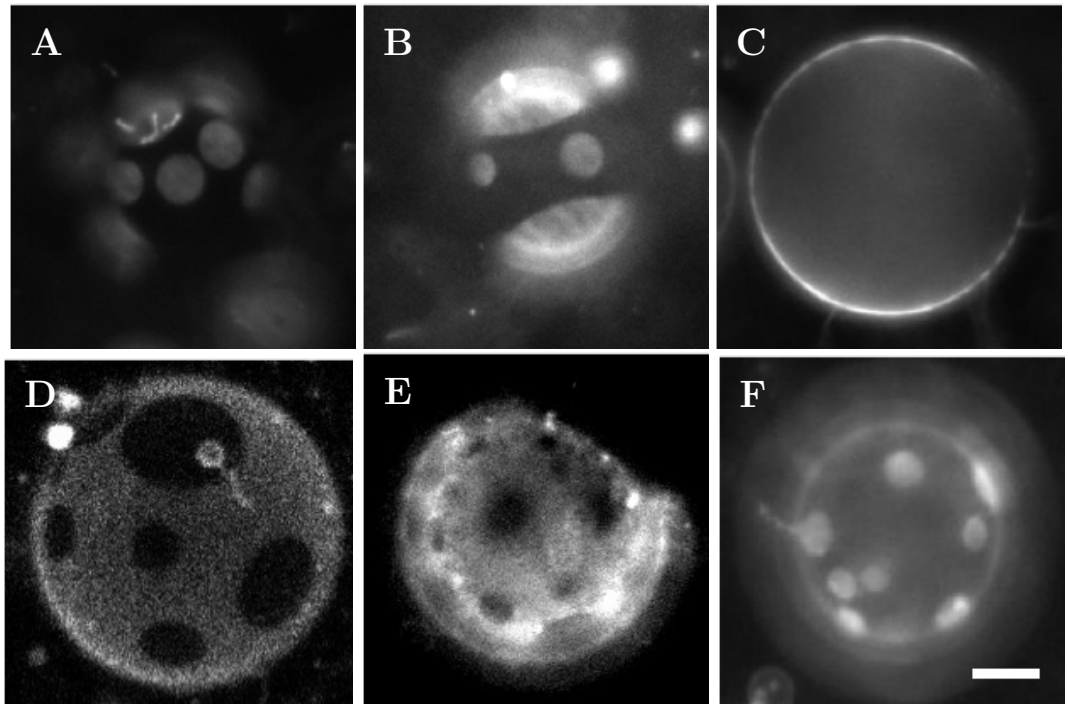

Figure 2.8: Phase separation in GUVs of 3-component lipid mixtures. GUVs electroformed from mixtures of DOPC, DPPC and cholesterol exhibiting a range of $L_o - L_d$ phase morphologies. While (**A**-**C**) were electroformed from the same lipid mixture ((3:4:3 DOPC:DPPC:Chol)), they exhibited different phase morphologies. This was due to poor lipid mixing during agarose-swelling at low temperature (lower than the highest T_m of the mixture). (**D**-**F**) show GUVs electroformed at high temperature (60° C) for different lipid compositions (2:2:1, 1:1:1 and 0.47:0.23:0.3 DOPC:DPPC:Chol respectively). Scale bar 10 µm.

Several strategies were experimentally evaluated to use as a handle for reversible switching of phase separation in the GUVs. DNA-hybridisation based switching was explored in detail. In systems with ternary lipid mixtures, the DNA-cholesterol partitions into both the L_d and L_o phases, but depending on ionic conditions and the type of spacer molecule used between the DNA and cholesterol, it can exhibit a weak phase preference, as well as potentially alter membrane structure. It was theorised that addition of a complementary DNA strand as a trigger, for example, might induce a reversible phase change depending on the size, charge or concentration of the DNA

strands. Cholesterol-TEG-DNA was used to construct three different types of DNA switching experiments based on complementarity and strength of interaction based on the number of cholesterol groups. 30 base pair strands were chosen so that they would be flexible as single strands, but rigid when hybridised. Single stranded DNA with a cholesterol group inserts into the bilayer and aligns itself roughly normal to the surface to the vesicle, whereas ds-DNA anchored by multiple cholesterol groups, being rigid and rod-like, lies flat over the surface of the vesicles [179]. This meant that a relatively large negative charge could be localised close to the surface of the membrane, potentially triggering a phase change in membranes with charged lipids. Vesicles were electroformed from a lipid mixture of 20% Cholesterol, 26.67% DOPG and 53.33% DPPC (1:2 DOPG:DPPC ratio) with 1% Texas Red DHPE in 10:1 TE buffer (10mM Tris, 1mM EDTA). 5 mol% pre-hybridised double stranded DNA functionalised with chol-TEG on the 3' and 5' ends was introduced to the suspension. This mixture was then subjected to a heating cycle, where the temperature was raised above and then lowered just below the miscibility temperature of this composition. A change in phase morphology was observed after the first heating cycle (Figure 2.9 A,B). This is evidenced by the change in the area fractions and size of domains of the phases. This suggested that the insertion of cholesterol-DNA had changed the morphology of the phases. This may have been due to the insertion of the chol-TEG-DNA into the membrane, as well as due to an electrostatic interaction between the DNA and the DOPG head groups. However, when the suspension was subjected to another heating-cooling cycle, it resulted in the vesicles losing their phase morphology and exhibiting only a single phase (Figure 2.9 C).

Once the vesicle formation protocols were established, it was possible to produce GUVs with fairly homogeneous lipid distribution for the DNA switching experiments. However, a few months into the project, difficulties were encountered in producing GUVs using either electroformation or agarose-lipid film hydration techniques. The GUVs formed were extremely unstable, and the yield was severely compromised due to vesicles bursting and budding. Investigating the problem using NMR and HPLC (with help from Dr. Hajra Basit) revealed the presence of oxidised lipids and other

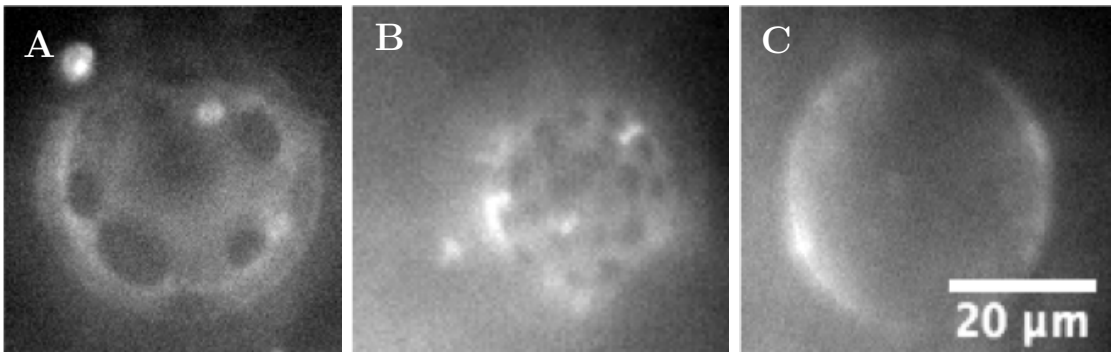

Figure 2.9: Chol-DNA as a trigger for GUV phase separation Vesicle phase morphology (**a**) before and (**b**) after insertion of Chol-DNA during the 1st heating cycle, imaged just below the T_m of DOPC. (**c**) shows the loss of binary phase morphology after multiple heating cycles, when imaged just below the T_m of DOPC.

impurities. Fluorescence imaging of a new stock of lipids showed the presence of fluorescent impurities in the new stocks of lipids. Other DNA constructs, as well as other switching mechanisms, such as light-induced cis-trans isomerisation of membrane-associated azo-molecules for vesicle rupture and budding [180] were explored, but not pursued.

Due to the inordinate amount of time spent in troubleshooting the contamination/oxidation issue, it was decided to undertake a collaborative project with Ms. Lyndsey Starr, to explore GUV shape changes and the role of curvature in bilayer fusion and hemifusion. This work was initiated on a young interferometric scattering microscope (iScat). Interferometric scattering is a light microscopy technique that detects the light scattered by the object, as opposed to detecting the signal from a fluorescent molecule. Label free imaging of molecules is highly desirable as it is eliminates photophysical effects such as photobleaching, and allows for perturbation free measurements of functional processes [8]. Previously, label-free imaging of lipid nanodomains had been reported from the lab [181].

GUVs were deposited on cover slips passivated with an SLB and the flattened surface was imaged on the iScat. In the presence of calcium ions, rapidly coalescing dark features were observed on the bottom of the GUV (Figure 2.10). In order to ascertain if there were any transient fusion events between the GUV and the SLB, a fluorescent lipid exchange assay was conducted. This led to the development of

this GUV-SLB system as a model membrane interface, as detailed in subsequent chapters. No more investigations were conducted on the iScat as it underwent further development, as detailed in other lab theses [182, 8].

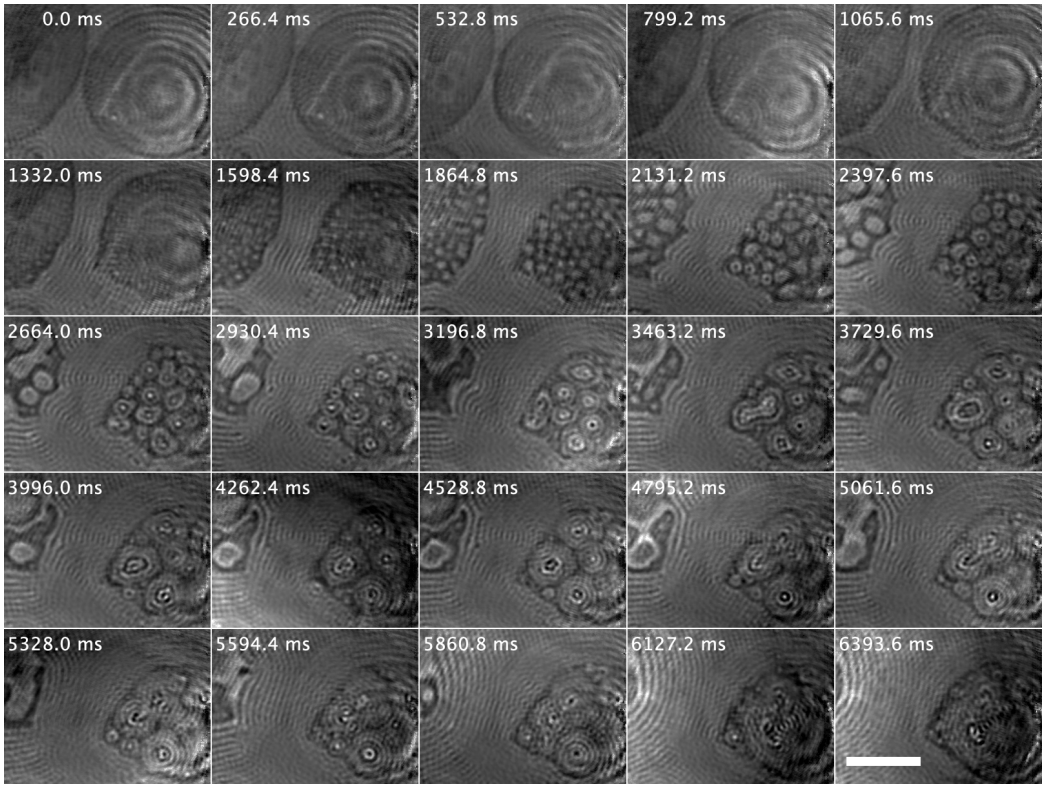

Figure 2.10: iScat of a GUV Time series of the flattened region of a GUV resting on an SLB, as observed using interferometric scattering microscopy. In the presence of Ca^{2+} ions, rapidly coalescing dark patches were observed, which were later found to be buckles due to membrane undulations. Scale bar 30 µm.

Chapter 3

Control of Membrane Diffusion in Artificial Synapses

3.1 Diffusion in GUV-SLB interfaces

This chapter presents a single-molecule study of diffusion at artificial membrane interfaces formed between GUVs and SLBs. This GUV-SLB model system allows for single particle tracking analysis of membrane components in both membranes, as well as the components that dwell in the intermembrane volume. The diffusion of lipids in both membrane were measured using single-molecule tracking. GUV lipids remain isolated from the SLB, and two distinct diffusive populations were observed. This allows for single-molecule analysis of the GUV lipids while also maintaining the osmotic and ionic gradients across the membrane. Next, membrane-anchored DNA linkers were employed as 'mimics' of interface binding proteins. SLBs and GUVs were doped with complementary DNA strands, and the hybridisation of these strands resulting in the formation of interface-bridging linkers. The strength of the interactions between the membranes was characterised by measuring lipid diffusion in the GUVs. Diffusion of lipids in the GUV was found to be dependent on the length, density and degree of hybridisation of the DNA anchors. Single stranded DNA strands were found to increase the mobility of lipids in the GUV, while hybridisation across the interface lowered it. Similarly, shorter strands were also found to lower diffusion in the GUV, while longer strands were found to have a much smaller influence. Interesting diffusive behaviours of some interface-spanning DNA linkers were also observed.

Finally, the data were analysed using the hydrodynamic approach proposed by Evans and Sackmann [95], and the results have been discussed. Thus, this chapter lays the foundation for a holistic single molecule level investigation into membrane synapses.

3.2 Dual bilayer single-molecule tracking

3.2.1 Specific methods

DOPC GUVs with 250 pmol% Atto488-labelled DPPE (sufficient to resolve individual molecules in the image) were electroformed in sucrose solution of different concentrations. DOPC SLBs were prepared by the normal method, and the SLB was sequentially washed with ionic buffer (typically NaCl or PBS) at the desired concentrations. GUVs were electroformed in sucrose solution. For the experiments using cholesterol-DNA spacers and linkers, GUVs were prepared in 150 mM sucrose solution, while SLBs were prepared in standard 1×PBS. GUVs and SLBs were separately incubated with a 5 µL aliquot of DNA suspension at concentrations calculated to achieve specific surface concentrations. An aliquot of the GUV suspension is then introduced into a chamber containing an SLB.

TIRF imaging was completed as per the general method. Image stacks of 2000 frames were recorded at 50 Hz. Image stacks were then median-corrected in FIJI, before tracks were generated in Trackmate using a Python script.

3.2.2 Forming the interface

Sucrose-laden GUVs sink to the bottom of the hydration chamber containing the SLB, which is hydrated by an ionic solution of a lower density than the sucrose (such as standard PBS solution or NaCl). The osmolarity of the SLB medium is typically slightly higher than that of the GUV sucrose medium, causing the vesicle to be 'floppy'. At the SLB, the GUV spreads radially from the apical contact point to form circular contact regions. Some GUVs burst, presumably due to defects or inclusions in the SLB. Furthermore, the SLB acts as a passivating film protecting the GUV from these substrate effects. Not only does sedimentation improve the

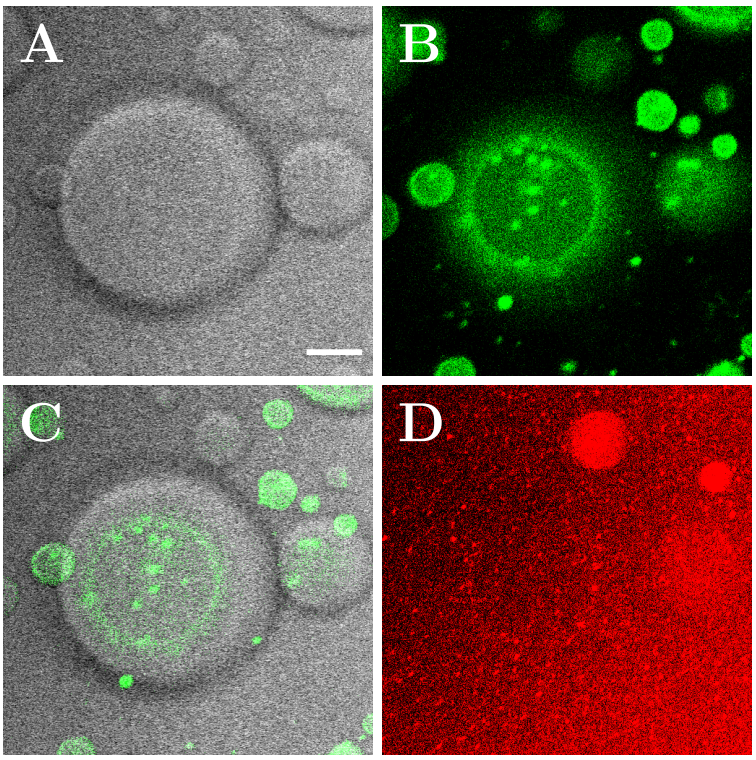

Figure 3.1: GUVs resting on an SLB. Multi-channel confocal images of Atto-488 labelled GUVs resting on an Atto647N-labelled SLB. GUVs are visible under (**A**) white light and (**B**) 532 nm illumination. (**C**) The composite of white (**A**) and green (**B**) channels shows a GUV where the interface with the SLB is smaller than the diameter of the GUV. The smaller green spots are small vesicles adhering to the GUV at the interface region. (**D**) shows the SLB under 642 nm illumination. Scale bar 20 µm.

yield of microscopically observable GUVs, but also stabilises the vesicles for acquiring contours or image stacks. Ipsen *et al.* study the effect of gravity on the bending rigidity of weighted GUVs, and find that contributions from gravity are in most experimental situations small and thus negligible [82].

Figure 3.1 (A) shows a confocal brightfield image of GUVs resting on an SLB. The central GUV has a diameter of 75 µm. Figure 3.1 (B) shows the flattened region (diameter 40 µm) of the Atto488 labelled GUV where it rests on the SLB. (Composite image Figure 3.1 (C)). Figure 3.1 (D) shows the Atto-647N labelled SLB.

3.2.3 Measuring lipid diffusivity

The GUV and SLB are separated by a thin aqueous layer. The separation between the two is maintained by the equilibrium of the "hydration forces" [183], a combination

of the van der Waals, steric and Coulomb forces between the two membranes. The thickness of this layer is of the order of 10 nm [184]. In a typical TIRF microscope, as the evanescent field decays within ~100 nm, fluorescent labels on both membranes, as well as in the hydration layer, can be illuminated and visualised simultaneously. Using single-molecule tracking analysis, the diffusivity of lipids in the GUV were found to be greater than in the SLB, as shown in Figure 3.2. (Diffusivity, or diffusion coefficient, is the the proportionality constant between a particle's mean squared displacement and observation time. The diffusion coefficient acts as a measure of the phenomenon of molecular diffusion. This measured value can be related to the mobility, which is a physical property of the ensemble, via the Stokes-Einstein relation. In practice, however, mobility and diffusivity are often used interchangeably.) The diffusivity of fluorescently labelled lipids in the GUV was measured as 4.21 ± 0.08 µm^2 s^{-1} and in the SLB as 1.27 ± 0.08 µm^2 s^{-1}.

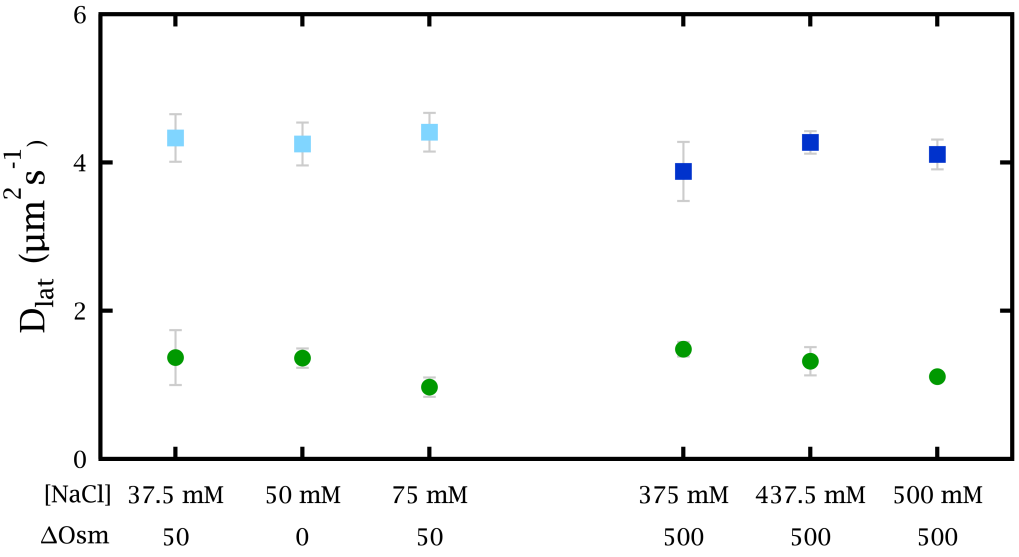

Figure 3.2: Effect of ionic and osmotic forces. Lateral diffusivity of lipids in the GUV (light blue: 100 mM sucrose, dark blue: 500 mM sucrose) and SLB (green) shown for a range of osmotic and ionic differences. Lipid mobilities in either membrane are largely unaffected by the osmotic difference across the GUV membrane, or the ionic strength of the SLB hydration medium.

GUVs formed in sucrose solutions of varying concentrations were introduced to SLBs in ionic media containing NaCl at different concentrations. Osmolarity at fixed

ionic concentrations was adjusted by the addition of glucose solution. Diffusivity of lipids in the GUV is unaffected by changes in osmotic effects and ionic strength. This implies that the shielding effect of monovalent cations and the effect of membrane stiffness at the interface are dominated by the hydration forces. This is in agreement with the Evans Sackmann model of hydrodynamic forces acting on a membrane near a solid surface.

3.2.4 Membrane defects and lipid exchange

SLBs were formed by the bursting of SUVs on a hydrophilic surface. Coverage and quality of the SLBs were tested using Fluorescent Recovery After Photobleaching (FRAP). As mentioned earlier, the SLBs acts as a passivating layer by inhibiting interactions between the glass substrate and the GUV lipid head groups [185]. The high energetic cost of lipids being transferred across the hydration layer means that two distinct populations of lipids are maintained. However, the SLB formation process occasionally leads to the incorporation of defects. These include irregularities and contaminants on the glass substrate, bare patches or voids in the SLB, and excessive SUVs adsorbed on the SLB. Following the same mechanisms by which SUVs are burst to form SLBs, these defects lead to the mixing of lipids between the GUV and the SLB. The SLB acts as a reservoir of lipids, and the movement of lipids from the SLB to the GUV was observed as an increase in the intensity of the fluorescent signal at the interface. Figure 3.3 (A) shows the time series of lipid mixing between a GUV and an SLB with excess SUVs adsorbed on the surface. In Figure 3.3 (C), a section of the SLB has been excised, and GUVs introduced to this SLB are shown to fuse with the SLB via the exposed edges of the bilayer at the boundary of the scratch. Both these mixing processes are analogous to the mechanisms of planar bilayer formation [70]. In the absence of SLB defects, fluorescent lipids are confined to their respective bilayers on experimental time scales, as shown in Figure 3.3 (B). Hence, for experiments involving GUV-SLB interfaces, extreme care was taken to ensure the glass surfaces were very clean. Oxidation of the acyl chains was also of concern, as it affects membrane fluidity

[186, 187]. However, SLBs were always prepared using SUVs less than 2 days old so as to minimise oxidation effects.

3.2.5 Membrane buckling

The osmotic imbalance across the GUV membrane drives a flow of water molecules from the inside of the GUV, reducing the volume, and a lowering of the surface tension within the membrane, manifesting as an effective increase in membrane area. That is, a spherical membrane with relatively low stretching modulus has more area than a sphere of the same volume. This excess area in turn causes an increase in the out-of-plane fluctuations in the GUV. When the GUV makes contact with the SLB, this results in water being trapped between the buckled regions of the GUV and the SLB (Figure 3.4). These buckles coalesce into larger bubbles, which diffuse outwards and undulate into the GUV membranes outside the interface region, stabilising in about 100 seconds (Figure 3.5 **A**).

This effect was observed when the GUVs were subject to a high osmotic pressure difference (~10^2 mM) [184], or low divalent cationic concentrations (~10^1 µM). The addition of divalent cations to a fully formed interface led to the formation of new buckles due to the disruption of the electrostatic and hydration interactions between the two membranes. As shown in Figure 3.5 B, divalent cations such as calcium and magnesium also resulted in the formation of regions with multiple bilayers. These were observed to be trapped vesicles which had budded off from the original interfacial region of the GUV.

In an aqueous solution, the charges on the head groups result in the existence of a surface charge density and an associated electrical double layer on either side of a bilayer. The formation of hydrogen bonds with water also results in the development of a 'hydration layer', which determines the separation between membranes. Divalent cations interact with multiple head groups as well as with water molecules, and are known to strongly adsorb onto membranes, meaning that divalent cation concentration is much higher near membranes than in the bulk solution [188]. This results in the dehydration of the membrane (shrinking of the hydration layer) and the formation

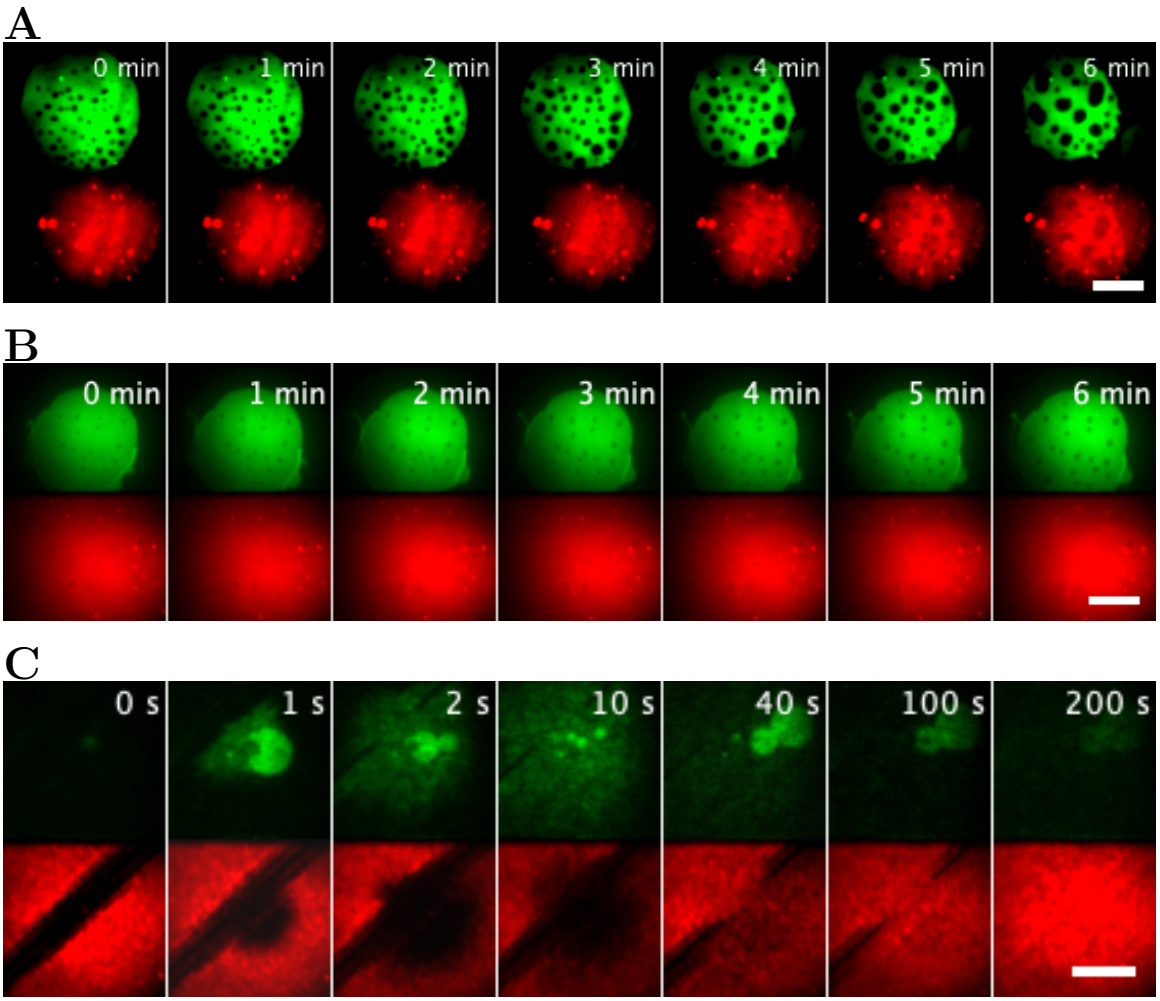

Figure 3.3: Lipid transfer across interface. (**A**) Defects in the SLB arising from the SLB formation process, such as bare patches or excess adsorbed SUVs (bright spots in the bottom row) can cause interactions with the GUV, resulting in lipids being exchanged over time. Here, TIRF microscopy of a GUV-SLB interface shows dark patches in the GUV channel where the GUV membrane is raised beyond the illumination region due to buckling. Atto647N-labelled lipids from the SLB (bottom row) are transferred to the Atto488-labelled GUV (top row). The dark spots begin to appear in the red channel because fluorophores in the buckled region are not excited, while in the region illuminated by the evanescent field, the intensity of Atto647N becomes the sum of the intensities of both membranes. (**B**) Defect-free bilayers ensure there is no lipid exchange with the GUV. Unlike in (**A**), there are fewer adhering vesicles, which are known to cause bridging between the two bilayers. (**C**) GUV (Atto488-labelled, green) interacting directly with the substrate at an exposed patch scratched into the SLB (Atto647N-labelled, red) causes lipid mixing between the two membranes. In the green channel, a vesicle can be seen landing on the exposed patch and spreads, and the flow of lipids from the GUV is also observed to displace the fluorescent SLB lipids in the red channel. More GUVs burst on the scratch outside the field of view, and gradually the SLB lipids mix into these regions. Scale bars 10 µm.

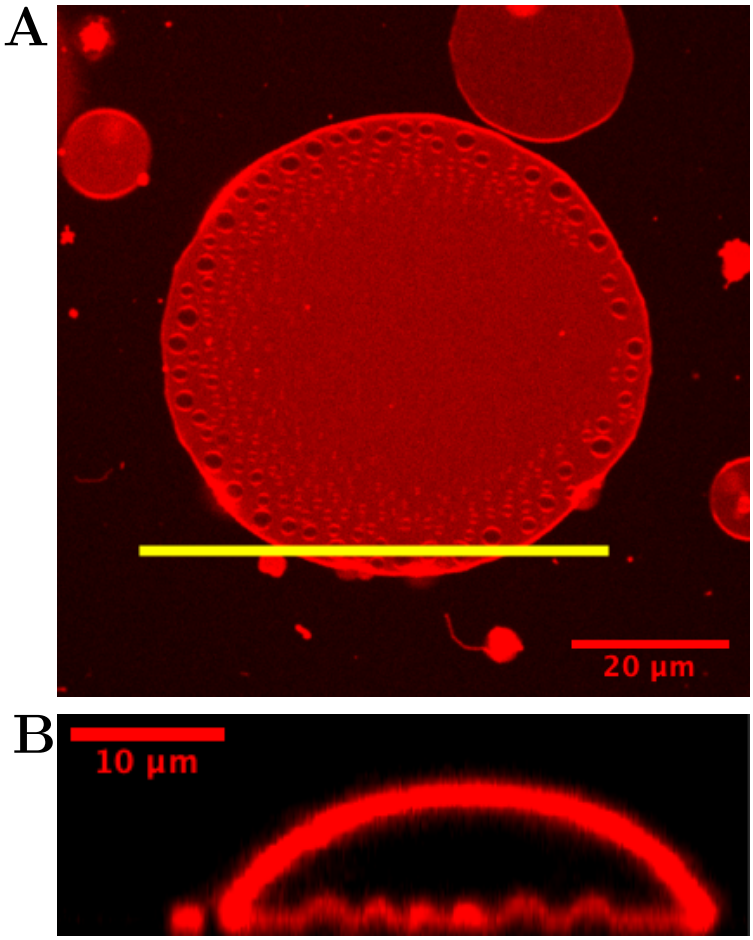

Figure 3.4: Buckling in GUVs. (**A**) Single plane confocal image of a GUV-SLB interface. (**B**) Z-stack along the yellow line in (**A**) reveals the curvature of the buckles.

of ion-bridges between the head groups [189, 188]. There is evidence in the literature of the effect of divalence in stabilising local high curvatures [190]. Divalent cations have also been implicated in causing membranes to adhere to each other [191].

Single-molecule tracks could still be obtained using TIRF, with no tracks observed in regions where buckles exist, as the membrane in these regions lies outside the evanescent field (Figure 3.6). However, the existence and effects of sub-resolution buckles have not been considered. Another interesting observation, though not pursued, was the movement of the GUV along the vertical axis (bobbing) upon the introduction of micromolar concentrations of divalent cations.

When the fluctuating GUV comes in proximity to the adsorbed SLB, the substrate hinders these fluctuations, resulting in an increase in the overall free energy of the

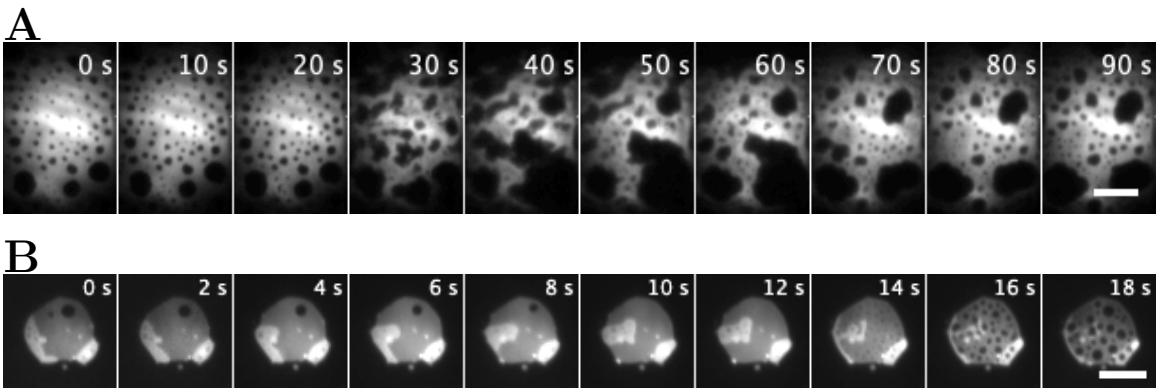

Figure 3.5: Defects at GUV-SLB interfaces. Grouped projections of defects evolving in GUV-SLB bilayers: (**A**) Buckling minimises undulation energy, with buckles coalescing and stabilising in ~100 s. (**B**) Divalent cations such as calcium cause non-specific interactions. Brighter regions denote multiple bilayers (indicating trapped GUVs) adhering to each other. Scale bars 10 µm.

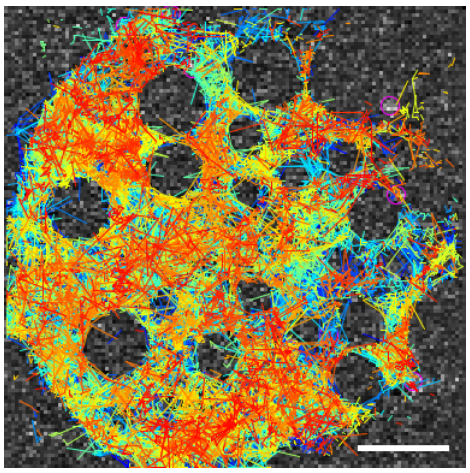

Figure 3.6: Single-molecule tracking of GUV lipids. Fluorescently labelled lipids are tracked using TrackMate. The dark regions represent buckles; no tracks are recorded here because the membrane is too high to be penetrated by the evanescent field. This is a representational image only, showing all the tracks that can be obtained from a single vesicle. In reality, specific regions of the interface are selected for tracking in order to account for edge effects, and tracks are filtered by duration to avoid capturing false tracks. Scale bar 10 µm.

system [192]. Therefore, the GUV membrane effectively exerts a net repulsive force on the SLB, which is inversely proportional to the square of the separation between the two membranes, and is commonly known as the Helfrich repulsion force [123]. In conjunction with the hydration forces and osmotic effects, this results in nanometre scale fluctuations in the GUV membrane, and causes the trapping of aqueous buffer

in the intermembrane region [184].

3.3 DNA oligomers as an adhesion-repulsion system

Following the establishment of protocols which allow for the reliable measurement of diffusivity of GUV lipids using single-molecule fluorescent tracks, DNA constructs functionalised with cholesterol were employed to modulate the interaction strength between the GUV and the SLB at the interface. SLBs were incubated with cholesterol-TEG-functionalised DNA (chol-DNA), and GUVs were incubated with similarly functionalised strands complementary to the SLB-anchored DNA, as well as a third, non-complementary strand. Two length regimes of DNA were studied. The following sections discuss the effects of hybridisation across the interface, densities of the DNA at the interfaces, as well as the effect of DNA length on the diffusivity of lipids at the interface.

3.3.1 Membrane functionalisation

DOPC GUVs with single-molecule concentrations of Atto647N-labelled DPPE were electroformed in 100 mM sucrose solution. DOPC SLBs were prepared as usual, and the hydration chamber was filled with 1× PBS (Phosphate-buffered saline) by sequential washing. DNA oligo suspension was pipetted into the SLB chamber, and allowed 20 minutes of incubation time for the cholesterol anchors to insert into the SLBs. The SLB was again washed with deionised water to remove non-specifically bound strands, and the chamber volume was again replaced with 1× PBS.

Previous studies also corroborate the spontaneous insertion of cholesterol-DNA into membranes from aqueous solutions [168, 143], and in subsequent experiments, all cholesterol DNA strands are assumed to have tethered to the membranes. For GUV coverage, aliquots of DNA strand mixtures were prepared at desired composition, and diluted such that the desired surface coverage was obtained by adding 5 µL of the mixture to 5 µL of the GUV suspension. GUVs were allowed to incubate for

20 minutes, and then introduced into the SLB chamber. The set up was once again allowed to incubate for 20 minutes to allow for the GUVs sedimenting to the bottom of the chamber, and for hybridisation to occur between the complementary strands on the GUV and SLB.

3.3.2 DNA oligo design

The DNA experiments sought to elucidate the effects of linker height and linker concentration on the interaction between membranes. For this, cholesterol-tagged DNA oligomers of two different lengths were designed. Short, 12 base pair (bp) sequences (or 12mers) were designed such that their melting temperatures ($T_m = 309K$) were sufficiently higher than room temperature (Table 3.1), so that complementary strands could hybridise under typical experimental conditions.

Strands S1 and S2 are complementary to each other, and are used, when hybridised, to form interface spanning linkages. Strand S0 is not complementary to either strands S1 or S2, and is used to control the fraction of hybridising species in an interface.

For experiments with longer 40 base pair oligomers (or 40mers), a prehybridisation strategy was employed to ensure that although the length is different, the interaction strength between the strands was the same as in the 12mer experiments (Table 3.1). To this end, a 14 base pair double stranded DNA ($T_m = 319K$) was designed with a cholesterol group on one end, and a 12 bp single stranded overhang on the other end. Hybridisation between these 'sticky' ends ($T_m = 309K$) resulted in the formation of 40 bp double stranded linkers. The simplest way to ensure similar interaction strengths would have been to maintain the same sequence for the overhangs as the 12mer constructs. Unfortunately, owing to oversight and constraints of time, logic was superseded. However, the melting temperatures of both are similar, and so the two constructs are expected to behave as expected under experimental conditions used.

SLB strand	Sequence	GUV strand
	AAGTAGCGCAAA–(5')–	S0
	GGTGACGGACGA–(5')–	S1 (309K)
S2 (309K)	–(5')–CCACTGCCTGCT	
OH1 (309K)	–(5')–GGGCGTTCCTGGAG / CCCGCAAGGACCTC–CCTAGCAGCGCA–GGATCGTCGCGT–GCCGTCACGTCACC / CGGCAGTGCAGTGG–(5')– ★	OH2(★) (309K)
F1★ (319K)	CGGCAGTGCAGTGG–(3')– ★	

Table 3.1: DNA constructs for interface modulation Short linkers S0, S1 and S2 of 12 base pair length were designed such that they interacted with each other across a GUV-SLB interface. S2 (which is complementary to S1) was tethered to the SLB, while S1 and S0 (which does not hybridise) were tethered to the GUV. 40 base pair linkers were made using dsDNA with 12 base pair overhangs. OH1 and OH2 each consist of a 14 base pair double-stranded section with a 12 base pair single stranded overhang, such that the overhangs on OH1 and OH2 are complementary. The overhanging segments are shown in **blue**. OH1 was typically tethered to the SLB, and OH2 to the GUV. The **brown oval** indicates the cholesterol-TEG anchor. ★ indicates the presence of a fluorescent label (Atto647N). In the experiments measuring DNA diffusivity in the SLB, the fluorescently labelled version of OH2, OH2★, was tethered to either the GUV or the SLB. F1★, being a partial complement of OH2, was employed as a cholesterol-free, fluorescently labelled DNA oligomer.

3.4 Results

3.4.1 DNA interaction with membranes

Insertion of cholesterol DNA was confirmed using fluorescence microscopy. Single-stranded DNA without cholesterol anchors associates with membranes via non-specific interactions and remains immobile. Figure 3.7 A shows fluorescently labelled single stranded DNA (F1★ from Table 3.1) statically bound to an SLB. Some of this DNA does not insert into the membrane and remains in solution. Washing with deionised

water replaces the buffer, thereby reducing the background fluorescence, but does not wash away the membrane-bound DNA (Figure 3.7 B).

F1★ was prehybridised with a cholesterol-functionalised DNA strand, forming the OH2★ construct, and was pipetted on to an SLB. It associates with a membrane under ionic buffer conditions (1× PBS), via the cholesterol anchor, and diffuses freely on the SLB. Figure 3.7 C shows tracking of OH2★ on an SLB. A fraction of F1★ remains unhybridised, both on the membrane and in solution, observed in the form of low quality spots and increased noise. Post-incubation, washing in deionised water eliminates the background fluorescence, but also diminishes the shielding effect of the cations on the hybridised DNA, and consequently denatures strand OH2★. This is evidenced as a loss of mobile fluorescence (Figure 3.7 D). However, similar to Figure 3.7 B, a static fraction of F1★ still remains on the membrane. Washing the membrane in Figure 3.7 C with an ionic buffer like 1×PBS, however, not only eliminates unbound DNA from the solution, but also effectively removes the static non-specifically bound DNA from the membrane. At the same time, cholesterol-anchored DNA remains diffusing on the membrane (Figure 3.7 E).

3.4.2 DNA diffusion at GUV-SLB interfaces

Analysis of the single-molecule tracks of fluorescently-labelled chol-DNA (OH2★) in GUVs and SLBs gave diffusion coefficient values of 3.25 ± 0.08 $\mu m^2 s^{-1}$ and 2.42 ± 0.21 $\mu m^2 s^{-1}$, respectively (Figure 3.8). These values are comparable to those of lipid diffusion coefficients (as seen in Figure 3.2) of 4.21 ± 0.08 μm^2 s^{-1} and 1.27 ± 0.08 μm^2 s^{-1} on the respective membranes. The variation in DNA diffusion coefficients may be attributed to a small sample size (N=3).

This same method was also used to verify the formation of GUV-SLB interface-spanning linkages of double stranded DNA. Upon hybridisation of the complementary sticky ends of the two strands OH1 and OH2★ across the GUV-SLB interface, the diffusivity of the doubly anchored DNA strands was found to be 2.46 ± 0.22 $\mu m^2 s^{-1}$. The lateral diffusion of a doubly-anchored component would be expected to be limited in its lateral movement by membrane undulations, and thus the intermembrane

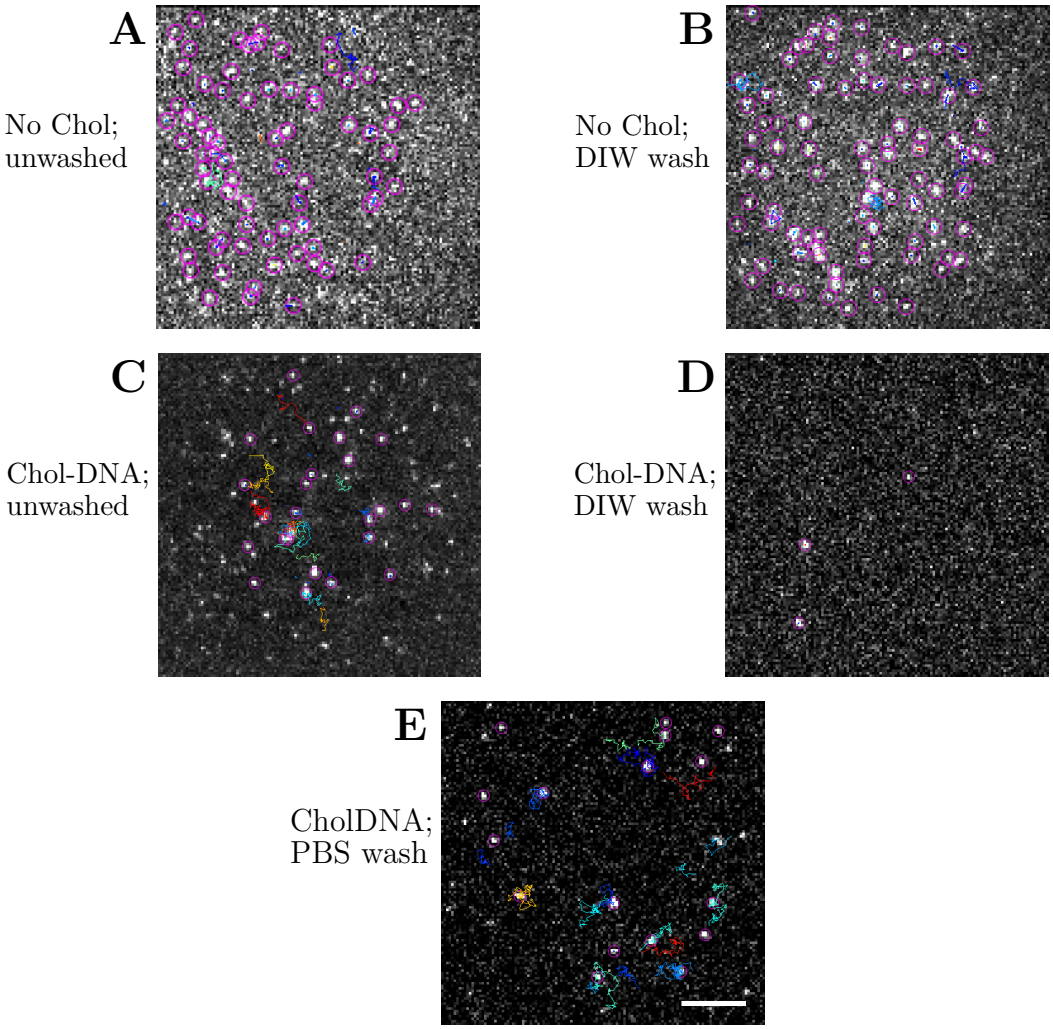

Figure 3.7: Determining the location of cholesterol anchor. (**A**) Fluorescently-labelled single stranded DNA strands without cholesterol anchors (F1★ from Table 3.1) insert into an SLB due to non-specific interactions, but do not exhibit 2-d diffusion. DNA strands still in solution contribute to greater background noise. (**B**) Replacing the aqueous buffer (*i.e.* washing) with deionised water reduces the background noise, but does not remove the immobile ssDNA from the SLB. (**C**) F1★ hybridised with cholesterol-tagged DNA strands in PBS buffer (forming the OH2★ construct from Table 3.1) diffuses freely on the SLB, indicating insertion into the membrane via cholesterol anchors. There also exists a static population of unhybridised ssDNA strands non-specifically bound to the membrane, as well as some DNA still in solution. (**D**) Washing **C** with deionised water resulted in the denaturing of the double stranded cholesterol-DNA due to removal of cations, and is evidenced by the loss of fluorescence. However, some fluorescent ssDNA remains non-specifically bound to the membrane. (**E**) Washing **C** with PBS buffer removes both non-specifically bound as well as background fluorescence, leaving only the 2-d diffusing fluorescent cholesterol-DNA. Scale bar 10 µm.

spacing [193]. In this case, however, the DNA bridge is 40 base pairs long. If these long DNA strands are able, as is argued later (Section 3.5.5), to adopt a range of tilted configurations, this allows them to explore a greater range of intermembrane spacing. Thus, the diffusivity is instead limited by the diffusion of the cholesterol anchor inserted in the SLB.

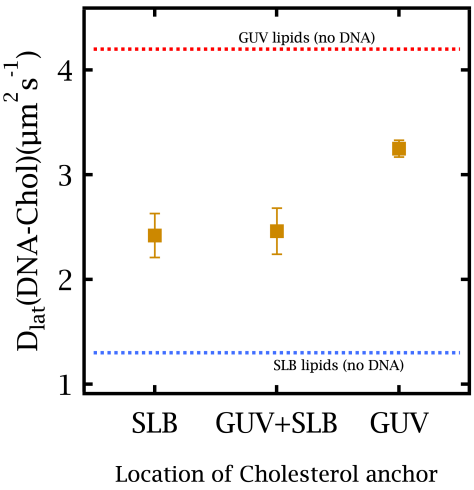

Figure 3.8: Diffusion of DNA at interfaces. The diffusivity of Atto647N-labelled dsDNA spanning the GUV-SLB interface via cholesterol anchors is similar to the diffusivity of the SLB anchor. The red and blue line indicate lipid diffusion constants in GUVs and SLBs, respectively.

3.4.3 Cushioning effect of unhybridised DNA

Interfaces were formed between GUVs and SLBs when only one of the membranes was functionalised with DNA strands (S1 on GUV, or S2 on SLB) (Figure 3.9 A and C). As seen previously (Figure 3.2), in the absence of any DNA, diffusion in the GUV at the interface with an SLB (and hence substrate) is slower than in a free membrane. The presence of unhybridised DNA on either membrane resulted in an increase in diffusivity of lipids in the GUV (Figure 3.9 B and D). This 'cushioning' effect is consistent with an increase in the distance between the GUV and the solid substrate.

On the other hand, increasing cholesterol-DNA concentration on the SLB (strand S2) has no effect on the diffusivity of lipids in an SLB (Figure 3.10). Lipid diffusion

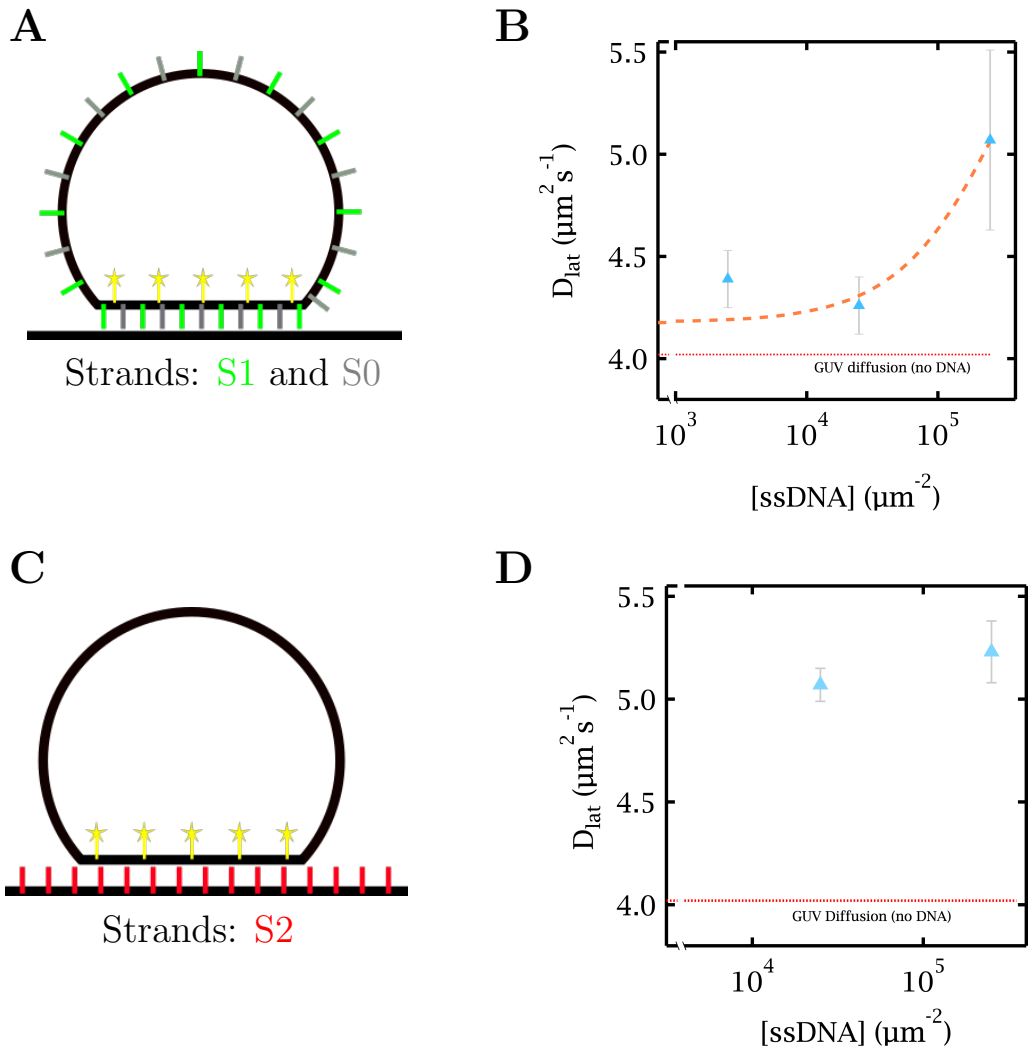

Figure 3.9: Single stranded DNA on a single membrane at GUV-SLB interfaces. The presence of single stranded DNA on either membrane at an interface (S0 and/or S1 on GUV, S2 on SLB) results in an increase in lipid diffusion in the GUV. (**A**,**C**) Cartoons depicting the location of the ssDNA. The graphs depict GUV lipid diffusivity for varying density of ssDNA on (**B**) GUV and (**D**) SLB.

in SLBs is (30-50%) lower than in GUVs [194, 195]. This is attributed to the strong coupling between the SLB and the substrate.

3.4.4 Coupling effect of hybridisation of short DNA

When the GUV and SLB were functionalised with complementary cholesterol-DNA strands, hybridisation of the strands resulted in the formation of gap-spanning double stranded linkers at the interface. When the complementary 12 base pair long strands

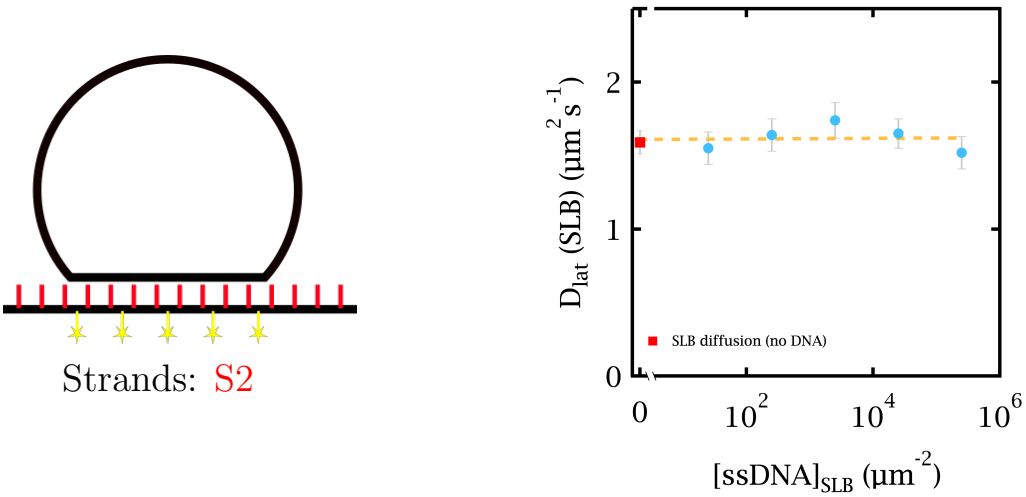

Figure 3.10: Effect of DNA concentration on SLB. Increasing the concentration of DNA S2 on the SLB has no effect on the diffusion of lipids in the SLB.

S1 and S2 (Table 3.1) were tethered to the membranes, the resultant linkers, of length ~4 nm, were observed to decrease the diffusivity of GUV lipids (Figure 3.11, orange). This effect was enhanced with the increasing density of hybridised linkers at the interface.

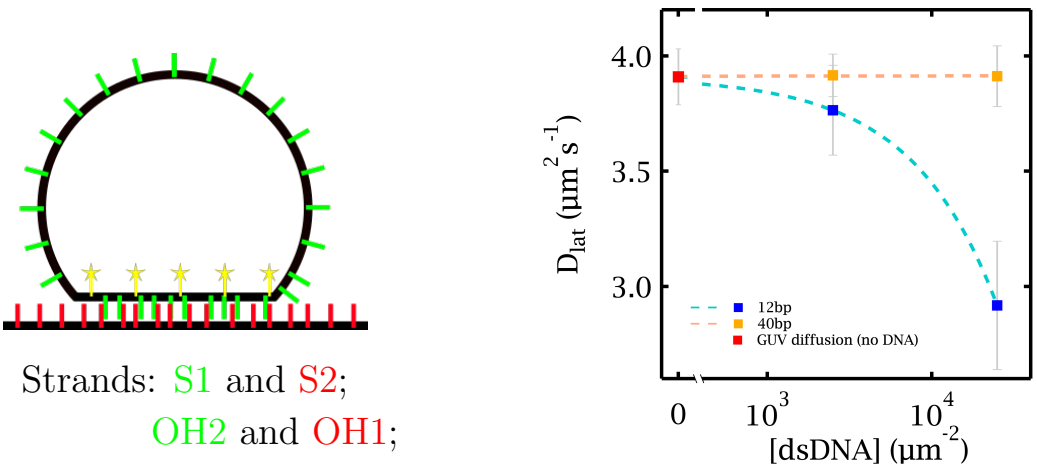

Figure 3.11: Effect of DNA hybridising across interfaces. Short 12 bp DNA (S1 on GUV and S2 on SLB) strands that hybridised across the interface resulted in a decrease in the GUV lipid diffusion (right, blue). However, hybridisation of longer 40 bp DNA (OH2 on GUV and OH1 on SLB) did not alter GUV lipid diffusion.

3.4.5 Effect of hybridisation of long DNA

A second linker length was also explored, where SLBs were loaded with sticky strand OH1 and the GUV with strand OH2 (Table 3.1). These hybridised into double stranded linkers 40 base pairs long, roughly 13.6 nm. Interestingly, hybridisation of these longer constructs did not show any effect on lipid diffusivity in the GUV (Figure 3.11, blue). This is opposed to the expected increase in diffusivity from an increase in the separation between the membranes.

3.4.6 Interplay of cushioning and coupling behaviours of short DNA

In the shorter DNA length regime, single stranded DNA tethered to membranes were found to reduce the coupling forces between the GUV and the SLB (or rather, GUV and substrate), while double stranded DNA hybridised across the interface were found to increase the coupling. This was measured as a change in the mobility of lipids in the GUV. To understand the transition between the fully coupled state and the fully cushioned state, experiments were performed where the relative surface concentrations of the linking and non-linking DNA were varied. This also provides some insight into the modulation of GUV membrane mobility.

In addition to the strand S1, GUVs were also loaded with an additional strand S0 (Table 3.1). S0 was designed such that it did not exhibit any significant base pair interactions with S1, or S2, which was present on the SLB. Thus, for any given concentration, the interface contained populations of hybridised S1S2 strands acting as couplers, and unhybridised S0 (along with any unhybridised S1 and S2) strands acting as the spacers.

First, the total DNA coverage of the GUV was kept constant at ~2500 µm^{-2}, while the mole fraction of the hybridising strand S1 x_{S1} on the GUV was varied. The SLB-side strand, S2, was also kept at constant surface density. At higher mole fractions of S1, lipid mobility in the GUV was diminished. Decreasing the amount of hybridising DNA resulted in a dramatic increase in the diffusion coefficient. For $x_{S1} < 0.6$, the

cushioning effect of S0 and S2 begins to dominate, and diffusive behaviour is similar to the cases with purely non-hybridising DNA (Figure 3.12 A).

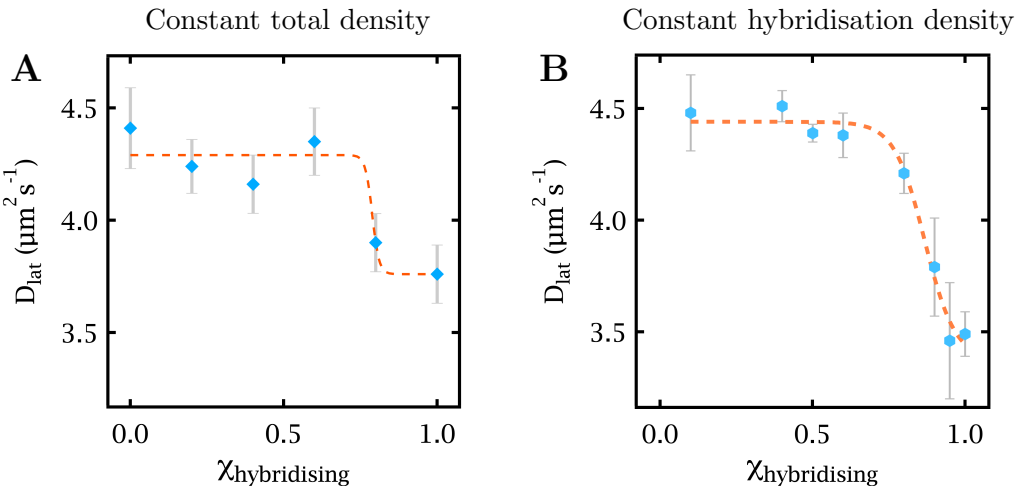

Figure 3.12: DNA linkers as a fraction of total surface coverage (**A**) Constant total surface density of DNA: When the total surface density of DNA on a GUV at an interface was kept constant, while varying the ratio of GUV-anchored DNA strands that could hybridise with an SLB-anchored species and those that could not hybridise, there is a sudden decrease in GUV lipid diffusion at higher fractions of hybridising DNA. (**B**) Constant surface density of hybridising DNA: When the total surface coverage of DNA was similarly altered while maintaining constant amount of hybridising DNA (varying the amount of non-hybridising DNA on the GUV), a similar decrease in GUV lipid diffusion was observed at lower fractions of non-hybridising DNA. In both graphs, the rightmost point ($\chi = 1$) corresponds to 2500 molecules of pure hybridising DNA per μm^{-2} of GUV membrane area.

Next, the total density of hybridising DNA was maintained at ~2500 μm^{-2}, while the density of non-hybridising strands was varied. Again, the coupling effects were observed at higher mole fractions of the hybridising strand (Figure 3.12 B). Two distinct equilibrium states, corresponding to two populations of lipids with distinct diffusivities were observed. Moreover, a crossover between the two diffusivity (and hence height) states was observed when the densities of hybridising and non-hybridising strands were nearly equal.

3.4.7 Effect of temperature on diffusion

Lipid mobility in bilayers is dependent on temperature, and higher temperatures result in increased lipid mobility. When the temperature of a GUV-SLB interface is increased, there is a resulting increase in diffusivity in the GUV (Figure 3.13). Similarly, when the temperature of a GUV-SLB interface fully couple with linking double stranded DNA (S1-S2) is increased above the melting temperature (T_m = 309 K), a much higher increase in lipid mobility was observed. While the difference in GUV diffusivities at elevated temperature does not seem statistically significant (one tail t= 0.64, p=.284), the difference between the diffusivities at high and low temperatures in the presence of DNA is highly significant (one tail t=5.38, p=.003). So, while the observed changes in diffusivity can be said to be driven by hybridisation, more information is required to state that the melting data points to a transition from the coupled state (with dsDNA) to cushioned state (with ssDNA on both membranes).

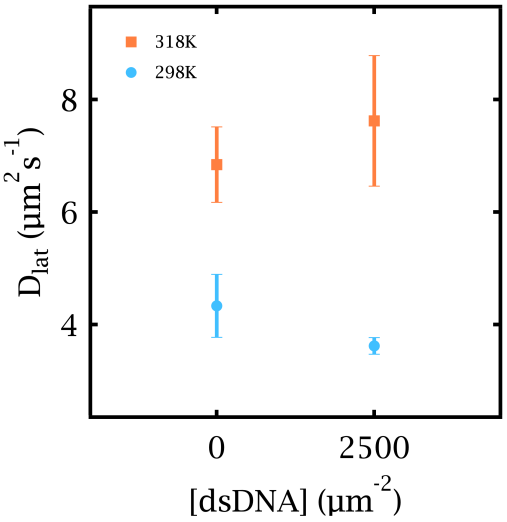

Figure 3.13: Effect of temperature on interface diffusion. Lipid diffusion in membranes increases with increasing temperature. Elevating the temperature of GUV-SLB interfaces with and without linking dsDNA strands above the melting temperature of the dsDNA strand resulted in a greater increase in lipid mobility when DNA was present (one tail t=5.38, p=.003). However, the two diffusivity values at elevated temperature are not significantly different (one tail t= 0.64, p=.284).

3.4.8 Effect of DNA on GUV membrane topography

While the results above have been predicated on the effect of the DNA on interface height, they do not take into account the effect of the DNA on membrane shape and intra-bilayer diffusion. In biological systems, phenomena such as transient binding [196], obstacles [157, 197] and crowding [158] affect the diffusion of molecules in the membrane, leading to anomalous diffusion [159]. While in normal diffusion the mean square displacement (MSD) scales linearly with time (Equation 1.6), anomalous diffusion describes motion where the second moment scales non-linearly with time. The picket-fence theory, for example, accounts for the corralling or trapping of particles due to interactions with the actin skeleton 'fences' and anchored protein 'pickets' [36].

In the DNA-mediated interface model, hybridised DNA, tending to have lower mobility than the surrounding lipid (Figure 3.8), may act as obstacles or pinning sites in the GUV membrane around which the lipids must diffuse. Figure 3.14 shows the MSD varies linearly with time, indicating that the DNA-containing GUVs exhibit pure diffusive behaviour. There is a small apparent dip in MSD for the smallest time windows. This is in part due to the empirically chosen maximum linking distance between successive frames excluding particles with larger displacements, and in part due to immobile spots, which get photobleached and thus do not influence MSD calculations for larger observation times.

However, it must be noted that the topology (undulations) and topography (density of linkers and spacers) can result in a decrease in the observed diffusion coefficient [8]. Single-molecule tracking excludes the 3-dimensional effects of membrane curvature, as it is a measures of only a 2-dimensional projection of the membrane. A relatively low bending rigidity of lipid membranes means that the DNA can induce local deformation, while membrane deformation itself can influence the spatial distribution of the DNA. While membrane buckling of the order of a few micrometers can be observed, buckling at nanoscopic length scales cannot be resolved using TIRF

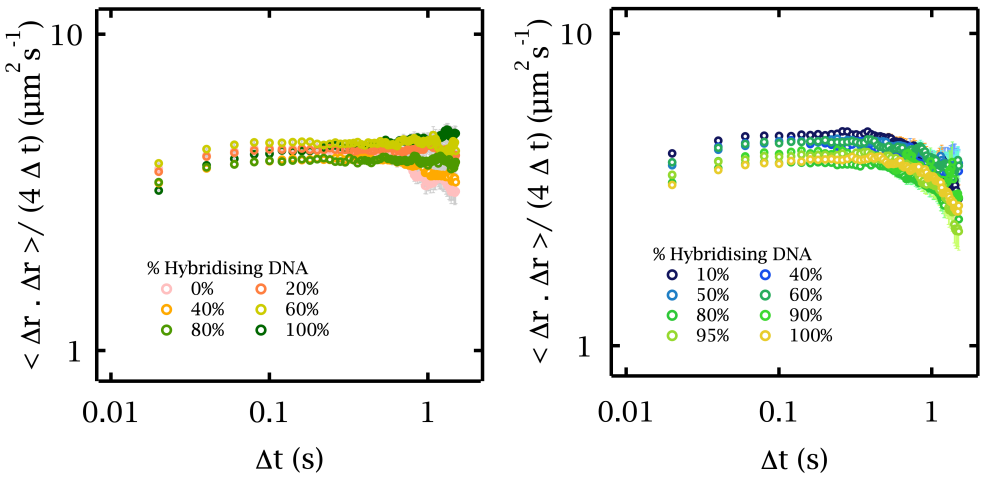

Figure 3.14: Normal or Brownian diffusion in GUVs. The presence of hybridising and non-hybridising DNA does not cause anomalous diffusion in the GUV. (**A**) MSD v t plots when total DNA concentration at the interface is constant, with varying ratios of hybridising and non-hybridising DNA. (**B**) MSD vs t plots for constant density of hybridising DNA, with varying non-hybridising DNA. Diffusion coefficient values at longer times scales are prone to greater error because there simply are a fewer number of longer tracks. The apparent dip for smaller observation times is due to the exclusion of larger unit displacements as well as due to the contribution of immobile spots.

microscopy. Despite these caveats, the GUV membrane at the interface can be modelled as a planar membrane, and the effect of the DNA can be modelled as a function of the height of the GUV.

3.5 Discussion

3.5.1 Polymer properties of DNA

DNA is a charged polymer whose physical properties are influenced by its length, hybridisation, salt concentration, graft density (on a surface), modifications to the phosphate backbone, nucleotide composition, base interactions and chemical modifications, among many other factors. In these experiments, single stranded, double stranded, and hybrid DNA of different lengths have been functionalised onto lipid membranes. In order to elucidate the effect of DNA on the physical properties of the membranes, some important polymeric properties of DNA are discussed, and certain assumptions are laid out.

1. Persistence Length: The persistence length, l_p is a measure of the flexibility of a polymer, the length over which the chain maintains a certain direction (*i.e.* is inflexible) [198]. The concentration of monovalent and divalent cations influence the persistence length of nucleic acids, as they shield the negative charge on the DNA. Divalent cations tend to have dramatic effects as compared to monovalent cations. Persistence length for double stranded DNA is known to be 50 nm [199]. For ssDNA, persistence length is taken to be ~2 nm [200, 201, 202] in 1×PBS buffer conditions.

2. Radius of gyration: The radius of gyration R_g is used to describe the shape and size of the random coil shape adopted by a polymer in solution. This is better representative of a polymer than its end to end length. For a 12mer ssDNA strand, under the same buffer conditions, R_g is taken to be ~2 nm [202]. As the radius of gyration is almost the same as the persistence length, the validity of polymer theory to this system needs to be examined.

3. Mushroom and brush conformations: When polymers are tethered to a surface, depending on the surface density, they can assume mushroom-like (lower density) or brush-like (higher density) conformations (Figure 3.15). In the mushroom regime, the DNA strands occupy a hemispherical volume of radius R_g at a surface density σ such that there is no overlap between adjacent DNA strands. [203]

4. Mushroom-brush transition: The mushroom-brush transition occurs when σ increases and the tethered chains start crowding each other. Gambinossi *et al.* consider a 18mer ssDNA strand functionalised onto a POPC SLB via a cholesterol-TEG anchor [204]. For their system, with $R_g = 2.52nm$, saturation was observed for DNA surface density of 0.045 nm^{-2} or 45000 μm^{-2}. This also corresponded to the brush transition density. However, they do not discuss the chol-TEG-DNA's diffusion in the SLB.

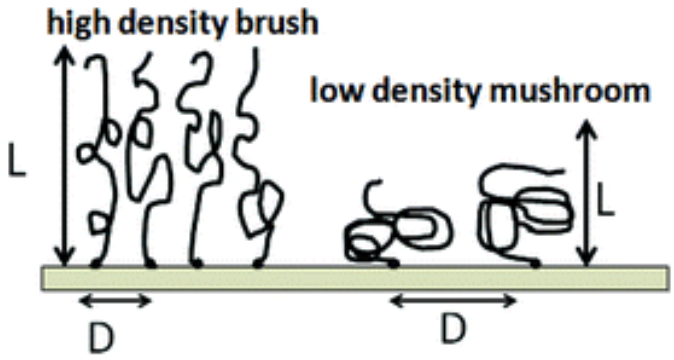

Figure 3.15: DNA tethered conformations DNA tethered to a membrane can take up either a mushroom or brush conformation depending on the surface density. Due to the presence of the chol-anchor, adsorbed state is not being considered. From [203].

5. The fully hybridised strand contain two nicks in the phosphate backbone owing to the sticky end hybridisation strategy. While nicks are known to induce bends and modify the persistence length, it has been reported that for ionic concentrations similar to those employed in these experiments, the persistence length is still larger than the actual length of the 40mer construct, and the bases remain stacked [205].

Taking the above into consideration, and as DNA is readily soluble in water (accounting for good solvent quality), it can be argued that for the ssDNA constructs used in our experiments (S0, S1, S2), at the surface densities used (<25000 µm−2), the DNA should fall within the mushroom conformation regime. Secondly, the 40mer constructs (OH1-OH2) can be said to be rigid doubly anchored objects of length 13.6 nm. In light of these assumptions, the relevance of the Evans Sackmann model shall be discussed further below.

3.5.2 Membranes in proximity to surfaces

According to Evans and Sackmann's hydrodynamic treatment of membranes in proximity to a solid substrate, the translational drag exerted by the substrate on a membrane is a function of the separation between them. The lipid diffusivity in the GUV under varying DNA conditions reveals that there exist two equilibrium regimes. These correspond to when the cushioning effect dominates and when the coupling

effects dominate for varying fractions of hybridising and non-hybridising DNA. In the coupled regime, GUV mobility is lower than in the resting regime, where there is no DNA at the interface. In the cushioned state, GUV mobility is higher than the resting regime (Table 3.2). Interpreted within the framework of the Evans Sackmann model of lipid diffusivity, these results imply that the coupling of DNA decreases the average separation between the two membranes, while unhybridised DNA increases it.

3.5.3 Unhybridised DNA increases the height of the GUV

The presence of unhybridised DNA on either membrane resulted in an increase in lipid diffusion in the GUV. The cushioning effect increases with an increase in the density of single stranded DNA on either membrane (Figure 3.9). This is consistent with an increase in the distance between the GUV and the SLB, and hence the GUV and the substrate. At high concentrations, the diffusivity value approaches that of lipids in an unsupported or free lipid bilayer ($6.3-11.3$ $\mu m^2 s^{-1}$) [206, 207, 208]. On the other hand, increasing concentrations of DNA on the SLB had no effect on diffusion in the SLB itself (Figure 3.10).

Figure 3.9 shows that GUV diffusivity is affected for densities greater than $\sim 10^4$ μm^{-2}. This could be because at low concentrations of the DNA, the membrane stays at unperturbed distance from the lower leaflet.

3.5.4 Hybridisation of short DNA strands pulls the GUV closer to the SLB

Short hybridised DNA linkers at the GUV-SLB interface caused a decrease in diffusion constant of GUV lipids (Figure 3.11). The height of the hydration layer at the interface is ~10 nm [184]. Being smaller than this separation, the hybridised linkers reduce the average height of the GUV from the substrate. This increases the coupling between the GUV and the substrate, resulting in increased drag, and reduced diffusivity. A greater density of linkers further reduces the average separation of the GUV as compared to the resting state (unfunctionalised membranes). Once again,

at lower linker densities, the membrane may conform around the linkers, and may explain why the GUV diffusivity is not strongly affected.

3.5.5 Long DNA strands are tilted by the GUV

Long hybridised DNA did not appear to have a significant effect on GUV lipid diffusion. It is postulated that it may be entropically favourable for the long, rigid double stranded DNA to preferentially adopt a tilted conformation in order to be accommodated within the interface [209]. This is also supported by the relatively high diffusivity observed for doubly anchored, interface spanning 40mer constructs (Section 3.4.2). It must be noted that the pre-hybridisation components OH1 and OH2 on each membrane are composed of a 14 base pair double stranded portion with an overhanging single strand. These fragments are relatively large and rigid ($R_h \approx 6.8nm$). The relatively large footprint of the tilted DNA may then result in the exclusion of the remaining unhybridised dsDNA fragments, thereby limiting the total amount of hybridisation. A similar phenomenon is known to occur in the case of interface spanning proteins reducing the space available for non-linking membrane proteins at an interface [210]. Moreover, the low interface height could also lead to the GUV membrane itself exerting a steric repulsive force on the double stranded, non-linking DNA [31].

3.5.6 Linker and spacer density affects GUV membrane conformation

In other words, non-linked single stranded DNA mitigated the drag experienced by the GUV, while short DNA linkers increased it. This observation gives credence to the hypothesis that at lower concentrations of both linkers and spacers, the membrane can locally deform to remain unperturbed by the DNA. As such, a crossover between the two diffusivity (and hence height) states is observed when the densities of hybridising and non-hybridising strands are nearly equal. As the density of non-hybridising strands increases, diffusing linkers at interfaces tend to aggregate into domains due to intermembrane repulsion [211], and thus the average height of the

GUV membrane is greater than the zero DNA resting state. It is also hypothesised that the high density of the non-hybridising strands, being $\sim 5\times - 10\times$ that of the hybridising strands, hinders the effective hybridising. Investigations using fluorescently labelled DNA linkers and spacers will shed light upon the formation and morphology of adhesion domains. At the concentrations of DNA currently employed ($\leq$ 2500 μm^{-2}, these domains may be expected to be very small, so greater coverage regimes may also need to be explored.

3.5.7 Calculating intermembrane separation

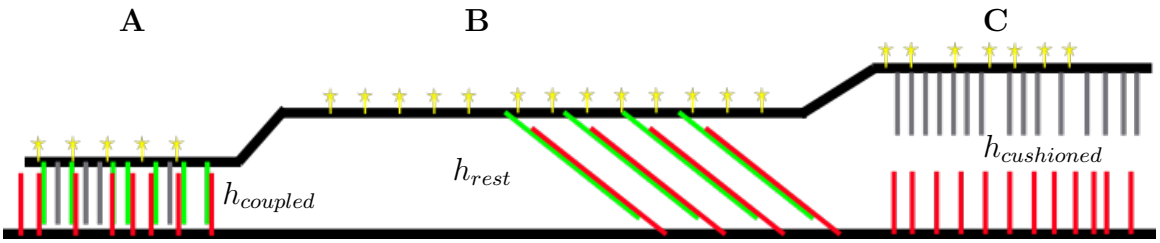

Figure 3.16: DNA linkers and intermembrane separation. The separation between the SLB (lower black line) and the GUV (upper black line) varies due to the effect of DNA. (**A**) Hybridising 12 bp DNA decreases the separation, when compared to the rest state (**B**), without any DNA. (**B**) Hybridising 40 bp long DNA does not affect the membrane separation, and assumes a tilted configuration. (**C**) Non-hybridising 12 bp DNA increase the separation between the GUV and the SLB.

From the Evans Sackmann model for membranes in proximity to a substrate, the translational drag exerted by the substrate on a membrane is a function of the separation between them. Ignoring the effect of the semi-infinite aqueous buffer on the *trans* side of the membrane (Equation 1.14),

$$\lambda_{\mathrm{T}} = 4\pi\eta_{\mathrm{m}}h\left[\frac{1}{2}\epsilon^2 + \frac{\epsilon K_1(\epsilon)}{K_0(\epsilon)}\right] \tag{3.1}$$

Again, reiterating Equation 1.13, the dimensionless radius parameter ϵ is approximated as

$$\epsilon \equiv R\left(\frac{\mathrm{b_s}}{\eta_{\mathrm{m}}h}\right)^{\frac{1}{2}} \tag{3.2}$$

Considering the frictional parameter b_s from Equation 1.12, and introducing an empirical proportionality constant α,

$$b_{\mathrm{s}} = \alpha \left(\frac{\eta_{\mathrm{b}}}{H} \right) \tag{3.3}$$

While the Evans and Sackmann [95] assigns $\alpha = 1$, Kaizuka and Groves, considering only the distance between a floating bilayer and an SLB, assign $\alpha = 2$ to fit their observations [108]. However, there is a lack of agreement in the literature about the nature of the frictional coefficient. Lipid mobility is also affected by the choice of lipid and substrate [212].

For the three mobilities, three heights can be defined with the following conditions (Figure 3.16)

1. As the average coupled state height $h_{coupled}$ is less than the average resting state height h_{rest}, the 12 bp dsDNA is considered to be perpendicular to the membranes.

2. As the 40 bp dsDNA does not affect GUV lipid mobility, h_{rest} is less than the length of the 40 bp DNA, or 13.6 nm.

3. Therefore,

$$4nm \leq h_{coupled} < h_{rest} < h_{cushioned} \tag{3.4}$$

4. The average cushioned height $h_{cushioned}$ is greater than $4\times$ the radius of gyration of the 12 bp ssDNA ($R_g \approx 2nm$[202]) (considering only steric exclusion close to mushroom-brush transition densities). This suggests the role of other repulsive forces between the two membranes, such as electrostatic and entropic repulsion.

3.5.8 Evans Sackmann Model: Caveats

The Evans Sackmann model is based on a membrane-spanning rigid, cylindrical inclusion of radius R diffusing in the membrane. While this model works well in describing the motion of lipid domains [181], the analysis presented in this chapter uses single-molecule tracks of fluorophore-functionalised lipids on both individual leaflets of the

membrane. It is believed that hydrodynamic treatments fail at molecular scales, and that diffusing lipids experience an effectively lower viscosity than do embedded proteins or other larger objects [213, 214].

Using typical values for membrane and bulk fluid viscosities ($\eta_{1\times PBS} \approx 0.9 \times 10^{-3}\text{Pa}\cdot\text{s}; \eta_{DOPC} \approx 140 \times 10^{-3}\text{Pa}\cdot\text{s}$[215]) and the height of the DOPC GUV h = 5 nm, Equation 3.1 was solved numerically for the fully coupled state where for GUV lipids, $D = 3.68 \pm 0.09$ μm^2 s^{-1}. Under the assumption that in the fully coupled state the height of the separation was 4 nm, a value of $\alpha \approx 0.17$ was found to fit the data.

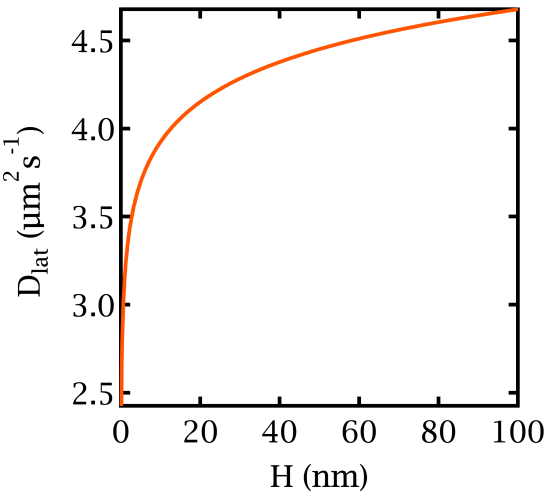

Figure 3.17: Effect of interface height on GUV diffusion. Diffusion vs height for typical values of membrane height and viscosity using $\alpha = 0.17$

The proportionality constant α accounts for the electrostatic and steric effects of the negatively charged DNA diffusing within the interface, as a function of the effective viscosity of the lubricating film. The value of α varies from that reported in the literature because it does not account for variations in the composition of the two membranes, which impacts the viscosity (η_m) and thickness (h) of the membranes, as well as for the viscosity of the bulk fluid. From Figure 3.17, the heights of the membrane can be estimated for the three equilibrium states (Table 3.2). These results are in reasonable agreement with the expected membrane separation for the resting and fully coupled states.

GUV state	Diffusivity	Height ($h_{GUV-SLB}$)
Resting (No DNA)	3.90 ± 0.07 µm^2 s^{-1}	9.5 ± 2.0 nm
Fully coupled	3.68 ± 0.09 µm^2 s^{-1}	4.0 ± 1.0 nm
Cushioned	4.44 ± 0.03 µm^2 s^{-1}	49.0 ± 5.0 nm

Table 3.2: Estimating intermembrane separation from the ES model.

However, it must be noted that the membrane height for the fully cushioned state appears to be significantly higher than expected, even taking into account *any* effect of DNA packing. Hydrodynamic treatments of membrane component dynamics work by coupling membrane flow to 3-d flow in the surrounding bulk fluid. Moreover, they tend to treat the membrane as a single elastic sheet. As such, they cannot be expected to be accurate at the molecular scale. Thus, they may only be used as a qualitative guide for interpreting experimental data on lipid diffusion [98]. Measured values of lipid diffusion vary according to methods employed [216, 160], while the choice of lipid, surface, and method of bilayer preparation also affect lipid diffusion [97, 217, 98].

Moreover, the Evans Sackmann model is accepted to be valid for a 'thin' aqueous film of up to a few hundreds of nanometers between a surface and a membrane. It is sensitive to the radius of the given inclusions [218]. As such, while numerical analyses based on lipid diffusion can provide qualitative information about interface heights, more accurate measurements can be obtained from measuring the diffusivity of larger components such as lipid domains or transmembrane proteins [108].

By contrast, the BDB adhesion model may seem to be more appropriate to model the GUV-DNA-SLB system, as a case has been made for the DNA functionalised interface to be considered as an attraction-repulsion system. However, in light of the assumptions presented in Section 3.5.1, the total surface density of all the DNA on both membranes is significantly lower than the values prescribed by the BDB model [99]. Most significantly, the ability of the 40mer construct to adopt a tilted configuration, allowing it to explore a greater range of membrane separations, precludes the

BDB model's optimal membrane separation consideration, as well as the Sackmann interpretation of the slow adhesion plaque formation process for tight contact.

Thus, as it stands, there is an urgent need to obtain more single molecule tracking data for DNA constructs of various lengths, in order to explore a relation between DNA length, membrane separation and lateral partitioning of DNA species. More evidence is required for the existence of the tilted configurations, and whether there is a transition between coupling and tilting states.The interaction of the 40mer construct with its constituent oligos OH1 and OH2 also needs to be studied.

3.5.9 GUV yield and DNA surface density

Membrane surface coverage of DNA was calculated by measuring total membrane surface area available per experiment. For the SLB, this was simply the total area of the SLB chamber. SLBs were formed in circular wells of radius 0.9 to 1 cm in diameter (depending on whether the chamber was formed using vacuum grease or the Grace BioLabs PDMS chambers). DNA was simply added to the membrane, as DNA functionalised with a cholesterol moiety are known to preferentially and irreversibly bind to lipid membranes, independent of the headgroup characteristics of the constituent lipids [129, 143]. As the DNA cholesterol was found to diffuse freely on the SLB, it can be assumed that at the time scales of membrane incubation and subsequent interface formation that the DNA are homogeneously distributed over the entire upper leaflet of the SLB.

In the case of GUVs, however, estimating the total membrane area available for interaction was more challenging. Ideally, the best control over DNA:lipid ratios (and thus surface area coverage) is achieved by adding DNA-cholesterol to the lipid stock prior to electroformation [109, 131]. However, this could not be replicated. Negatively charged DNA is thought to impede the growth of GUVs by shielding the interfilm repulsions resulting in aggregation, drop in yield and average vesicle size. Therefore, in the experiments described above, DNA-cholesterol was added to GUVs after electroformation. This method is also advantageous in that the same batch of

electroformed GUVs can be used for multiple experiments, titrating different volumes of DNA to achieve required surface densities.

For the experiments involving hybridising-non-hybridising density variation, a reference point of 2500 DNA-cholesterol per μm^2 of the membrane surface has been used. This is an estimated 1% to 10% of the typical receptor surface density in human cells [31, 219, 220, 221]. The total surface area available per experiment was calculated by estimating the total area of interfaces formed. Approximating the resting GUVs to be hemispherical, total available GUV area per experiment was thus $3\times$ the total interface area. However, due to the variation in GUV yield between electroformation batches, it was difficult to correctly ascertain the absolute surface density of the DNA-cholesterol on the GUVs. Calculating from the net GUV area per experiment gave an efficiency of electroformation (defined as the amount of lipids 'converted' into GUVs from the total amount of lipids coated onto the electrodes) of between 0.05% to 5%. This is comparable to the efficiency reported by Pereno *et al.* [222], as well as to that reported by Dr. Matthew Blosser in a private communication. However, despite a variation of the order of $\sim 10^2$ in this factor, the GUV diffusion data remains consistent with the Evans-Sackmann model of membrane height. In the case of hybridisation across the interface, steric effects are likely to dominate, thereby reaching a critical density of linkers. The diffusive trapping of the GUV-bound DNA at the interface may also play a role in limiting the density of DNA within the interface. A fluorescence microscopy based investigation of DNA density may shed light on some interesting phenomena in the experiments reported in this chapter.

3.6 Summary

In this chapter, interfaces formed between an SLB and a GUV resting on it were investigated using TIRF microscopy and single-molecule tracking techniques. DNA linkers and spacers were used to alter the separation between the two membranes, and consequently control the diffusion of lipids in the GUV. Short linkers across the hydration layer were found to reduce lipid diffusion in the GUV, corresponding to

a decrease in intermembrane separation, while unhybridised DNA at the interface increased GUV diffusivity, in effect having a cushioning effect. Varying the proportions of hybridising and non-hybridising DNA revealed two equilibrium states for the GUV, corresponding to 'fully coupled' and 'fully cushioned' regimes. Interestingly, long linkers and non-linking double stranded DNA had no effect on GUV diffusion; while the long linkers tend to assume tilted conformations, the non-linking oligomers were sterically excluded from the interface. As the entire volume of the interface is accessible to TIRF, it would be possible to explore the diffusive behaviour of various interfacial components. The ability of some constructs Further work is required, using fluorescently-labelled DNA, to ascertain the location and organisation of the various DNA strands.

Chapter 4

Modifying Membrane Morphology and Interactions with DNA Origami Clathrin-Mimic Networks

This chapter details work done in collaboration with Céline Journot and Andrew Turberfield, and forms the basis of the paper cited in Appendix A. Céline designed and characterised the DNA origami triskelion nanostructures, including TEM imaging. My role was to optically image the nanostructures' interactions with lipid bilayers.

4.1 Shaping membranes

Much of our understanding of membrane biology arises from direct observation of active cellular membrane processes, including the dynamic modulation of the size, shape and properties of the membrane by the action of membrane-associated proteins [45]. Altering membrane curvature, for example, can arrange membrane components into domains and generate microenviroments to facilitate processes such as membrane trafficking [223]. Membrane curvature is also crucial for cell growth, division and movement [223]. Curvature can be modulated by changes in lipid composition [224], imprinting scaffolding proteins [225], and by the insertion and crowding of protein 'wedges' into membranes (Figure 1.6) [44]. Peripheral membrane proteins such as clathrin, dynamin, SNARE proteins and BAR-domain proteins are recruited to impart site-specific curvature to the membrane [226, 227].

Clathrin is one such site-specific protein responsible for modulating membrane curvature. A well-studied protein, it is recognisable by its triskelion (or three-armed) shape. Clathrin is best known for its role in a classical endocytosis pathway, where clathrin proteins self-assemble into a polyhedral lattice that gradually coats the membrane. This causes the lipid bilayer to invaginate, forming what are called the *clathrin coated pits*. These subsequently detach, helped by the constricting action of dynamin at the neck of the pits [52]. Other proteins such as annexins and s-layer proteins assemble into dense networks to impart structural rigidity and protection from the environment [228, 229].

In this chapter, the properties and interactions of a DNA origami triskelion, which models the structural properties of clathrin, are presented. This shape mimic can be programmed to polymerise into flexible, extended, membrane-bound assemblies. Polymerisation of the triskelia led to nanoscale membrane deformations of lipid monolayers, resembling the effects of clathrin assembly. Interactions of the triskelia with lipid bilayers are also discussed, and the effects of DNA triskelia polymerisation on the interactions between membranes are discussed.

4.1.1 Clathrin

Clathrin is a trimer composed of three long subunits radiating from a central hub. Each arm of this triskelion consists of a ~190 kDa heavy chain joined together at their C-termini, as illustrated in Figure 4.1 **A**. Close to this central hub, each heavy chain bears a 25-35 kDa light chain [230]. Each arm is about 50 nm long [231]. Interactions between short motifs on the heavy chains of adjacent triskelia cause the arms to interdigitate, forming a lattice (Figure 4.1 B) (hence the name, from the Greek *clathratus* meaning lattice-like [232]). The clathrin lattice consists of faces that are pentagons, hexagons, and occasionally heptagons [233]. Despite the puckered shape of an individual clathrin molecule, clathrin can also assemble into flat hexagonal lattices or 'plaques' [234]. The size of the 3-dimensional cage assemblies can vary from 35 nm to 200 nm depending on type of membrane and location within the cell [235, 236]. The clathrin molecule exhibits flexibility that allows for the pucker angle to vary between

different assemblies [237]. In addition, variation in the angle between two joined arms of adjacent triskelia also contributes to the shape and size of the assembly (Figure 4.1 c). Bending of membranes by coat formation is dependent on interaction strength and conformation of the coat, and also on osmotic effects [75, 238]. Additional protein machinery such as dynamins are recruited at the clathrin-coated pits and help in the scission of the curved membrane sections, leading to the formation of clathrin-coated vesicles [52]. These coated vesicles then identify and affix on adaptor proteins on other membranes, initiating pathways for fusion and coat disassembly [43].

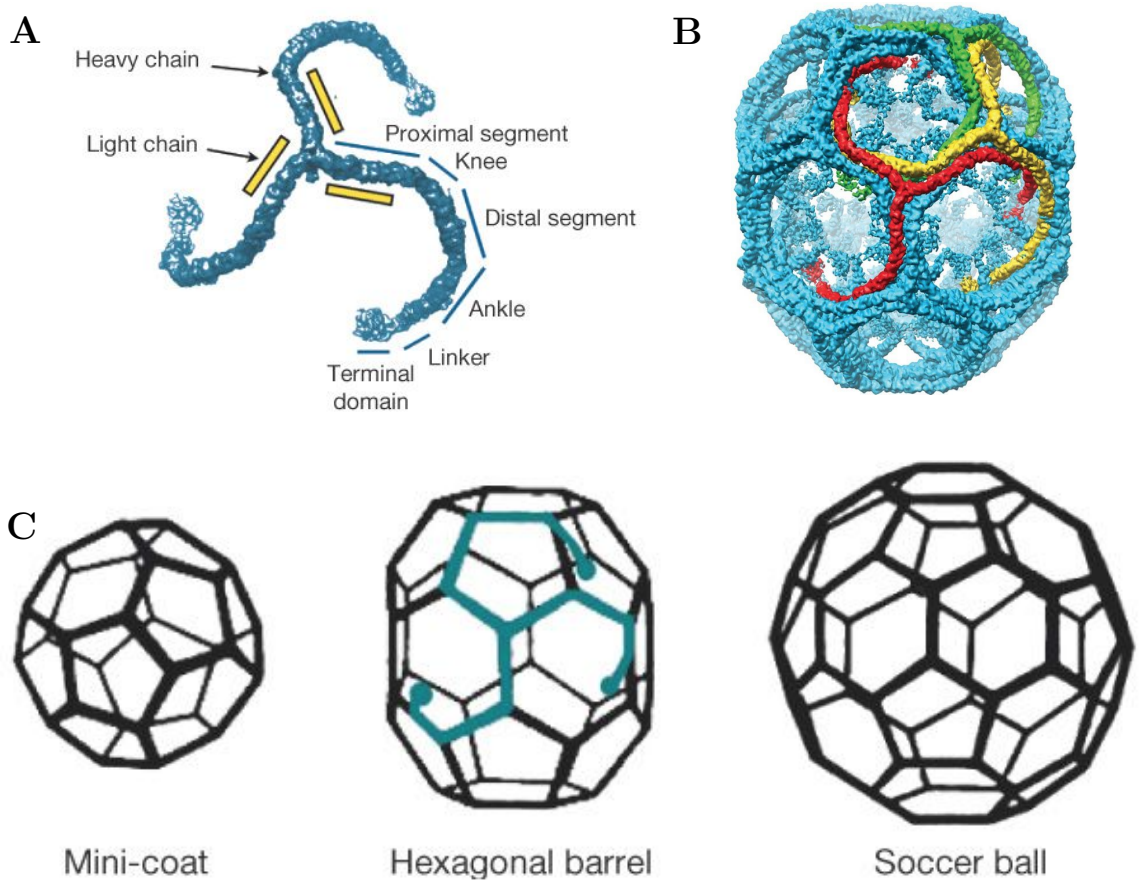

Figure 4.1: Shape of Clathrin. showing (**A**) labels expanding on the 'legs' analogy of the triskelion (referred to in this text more conventionally as 'arms'), (**B**) clathrin triskelia interdigitation, and (**C**) different conformations of the clathrin coat. Adapted from [48].

.

The mechanisms of curvature generation from flat clathrin plaques, and the general role of protein shape and protein assembly conformation in bending membranes are

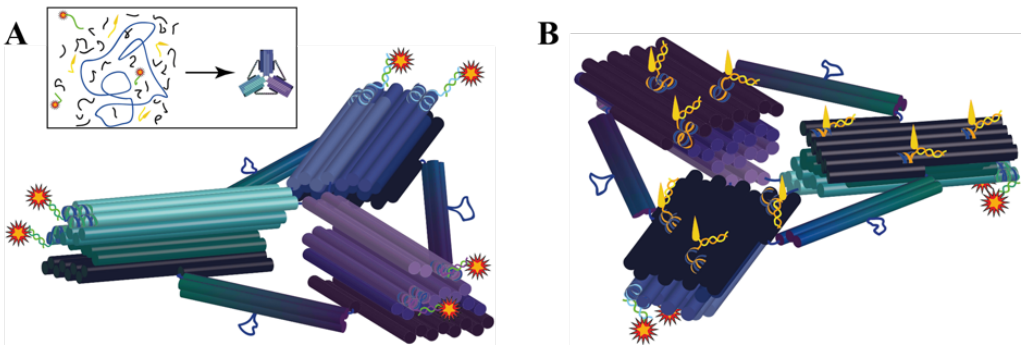

Figure 4.2: Design of DNA Origami. (**A**) Top and (**B**) bottom views of a triskelion showing the three arms, the rigid bridges to control angle, and conjugated cholesterol and Alexa647 moieties.

still the subject of debate. An artificial construct based on DNA origami provides some insights into the interplay of shaping-protein shape and lipid membranes.

4.2 Design of DNA origami triskelia

A three-arm DNA origami nanostructure was designed, whose shape resembles that of the clathrin triskelion (Figure 4.1). The construct consists of sheets of parallel DNA double helices stacked in four layers in a honeycomb fashion. The arms of the origami structure are about 30 nm long, while being about 13nm high. The four stacked layers and relatively short length ensure that the construct is sufficiently rigid to enable membrane bending [239]. This results in the DNA construct being approximately 20 times heavier than an individual clathrin molecule. The four layers of double helices are also arranged such that allow for defining a narrower 'top' surface and a broader 'bottom'.

The angles between the arms of the DNA triskelion are constrained and controlled by DNA helices that form bridges connecting the mid-points of each arm (Figure 4.2). Varying the length of these bridges (by varying the length of the single-stranded loop in the middle of the bridge) allows for control over the internal angle of the triskelia, and thereby the curvature of the assemblies. The triskelion can either be flat (180°± 4°) or curved (*i.e.* pyramidical, 118°± 4° to the bottom horizontal). The curved constructs have a height of about 18.4 nm.

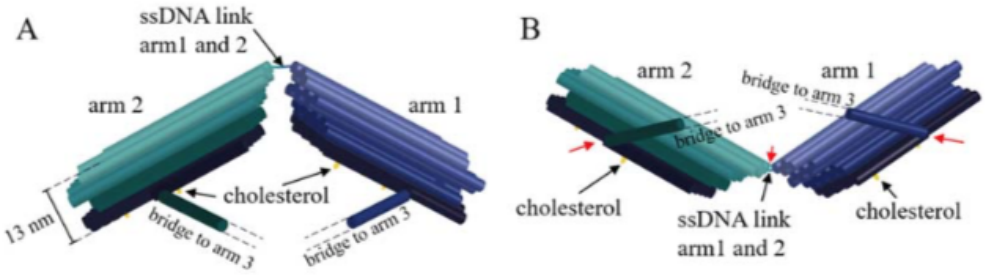

Figure 4.3: Internal curvature of DNA triskelia. (**A**) Schematic representation of a 'concave' triskelion, defined so by the presence of the cholesterol modifications on the concave surface. The cholesterol determines which face is proximal to the membrane upon insertion. (**B**) 'Convex' triskelia present the cholesterol on the convex or outer surface. While the angle of curvature is determined by the length of the bridges, the direction of curvature is dependent on the position of the cholesterol groups. In these figures, arm 3 has been removed for purposes of clarity.

The triskelia were functionalised with three cholesterol groups on the bottom side of each arm. Multiple cholesterol anchors enable the triskelia to tether irreversibly to lipid membranes [129]. The positioning of the cholesterol groups thus defines the triskelia as possessing 'convex' or 'concave' internal curvature (Figure 4.3). The end of each arm was adorned with two Alexa647 fluorophores for visualisation by fluorescence microscopy.

The CADNAno routing scheme for the DNA triskelion is shown in Appendix C.

4.2.1 Polymerisation

Clathrin self-assembles via electrostatic interactions between amino acids along the length of the arms. In the DNA triskelia, the end of each arm is 'sticky', i.e. loaded with short, single strands of DNA. 'Staple strands' are single stranded DNA in which half the sequence is complementary to the sticky end of one arm of a triskelion, and the other half is complementary to the sticky ends on one arm of another triskelion. When added to the triskelia, each staple hybridises with two triskelia, thus assembling them into a hexagonal two-dimensional matrix. Thus, this is different to the interaction of clathrin, where the linkages occur along the length of the arms. The distance between

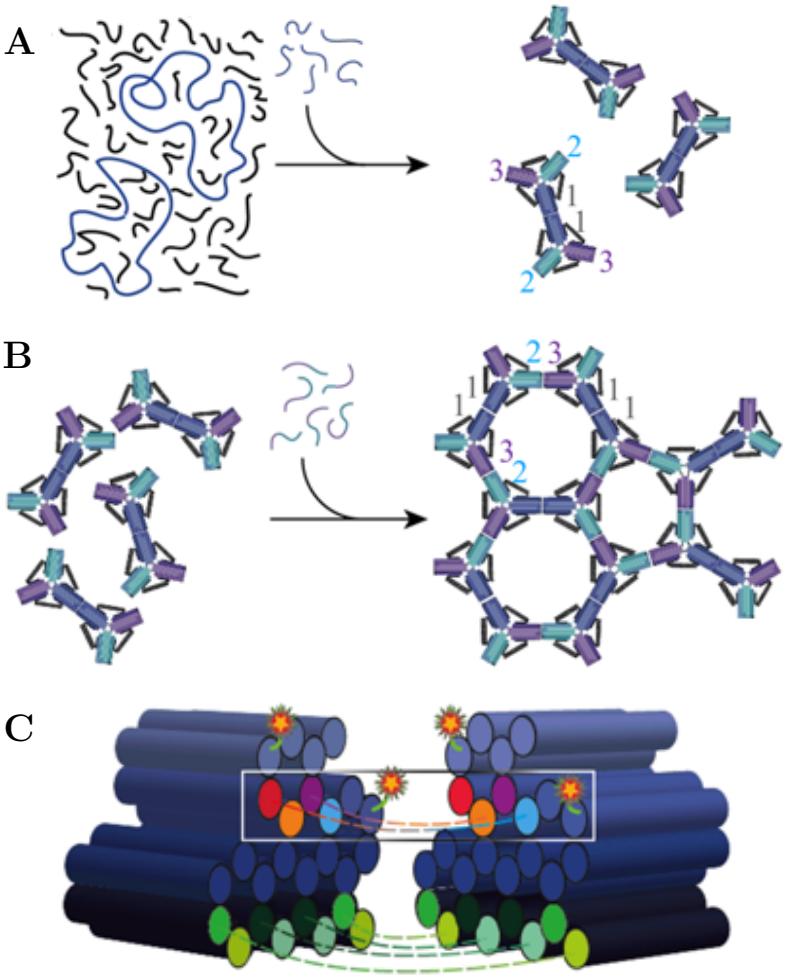

Figure 4.4: Schematics for triskelion assembly. Illustration of DNA folding leading from single stranded scaffolding to 2-dimensional triskelion array upon the addition of folding and polymerising staples (**A**,**B**). (**C**) illustrates the interaction between adjacent triskelia via their respective 'sticky ends'.

the two centres is therefore 60 nm, which is approximately twice the distance between two clathrin monomers in a lattice [240].

4.2.2 Dimers

The isothermal polymerisation of DNA triskelia was found to be faster and more accurate (in forming meshes) when using dimers of the triskelia instead of monomers. The diffusive behaviour and interactions of unpolymerised triskelia dimers on GUVs were undistinguishable from that of monomers [239]. Dimers are also assembled using the staple strand strategy. Six dimerisation staples bind to scaffold domains at the ends of two congruent arms of two component triskelia, forming six parallel connections between them (Figure 4.4). Henceforth, in the rest of this chapter, 'unpolymerised DNA triskelia' refers exclusively to the dimer form of the triskelia.

4.3 Membranes and triskelia

4.3.1 Triskelia on monolayers

DNA triskelia were assayed on DOPC monolayers which were formed on air-water interfaces by solvent evaporation, followed by insertion (via cholesterol moieties) and polymerisation of the triskelia. Insertion was achieved by incubating the monolayers in the presence of the cholesterol-functionalised triskelia dimers for at least 10 minutes. The monolayers were then transferred on to a carbon-coated gold electron microscope grid, stained with uranyl acetate and observed by transmission electron microscopy. Flat triskelia dimers were found to readily attach to the monolayer and polymerise into extended hexagonal arrays (Figure 4.5, top). Triskelia with inverted curvatures (cholesterol groups on convex side) were found to assemble into denser and less regular networks [239]. In both these cases, isolated, circular projections, were observed (Figure 4.5, bottom). This is consistent with local deformation or budding induced by the formation of the triskelion arrays. In the case of the curved triskelia, the clusters are more densely stained, which suggests that the buds have not collapsed. In the case of flat triskelia, several blebs appear to have partially collapsed.

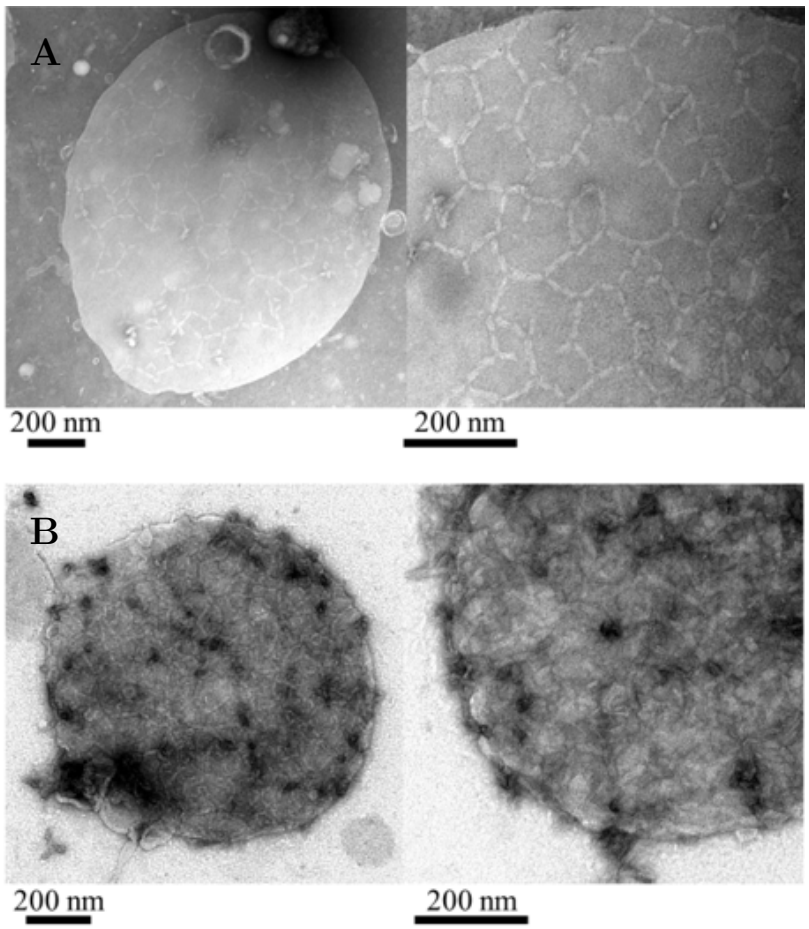

Figure 4.5: Triskelia on lipid monolayers. TEM micrographs of lipid monolayer to which (**A**) flat triskelion dimers were attached before polymerisation was triggered by addition of DNA polymerisation staples. A partially ordered array, with hexagonal and pentagonal cells, is visible. (**B**) When using curved triskelion dimers, local deformation was observed as darker regions that correspond to a higher local density of lipids. From [239].

4.3.2 Triskelia on SUVs

The interaction of triskelia with SUVs was observed using transmission electron microscopy (TEM). The triskelia tethered to the SUVs via insertion of the cholesterol conjugates into the outer monolayer. The triskelia were observed to form dense coatings around the vesicles, but the drying conditions employed in sample preparation for the TEM prevented the identification of any effects of the triskelia on membrane shape (Figure 4.6).

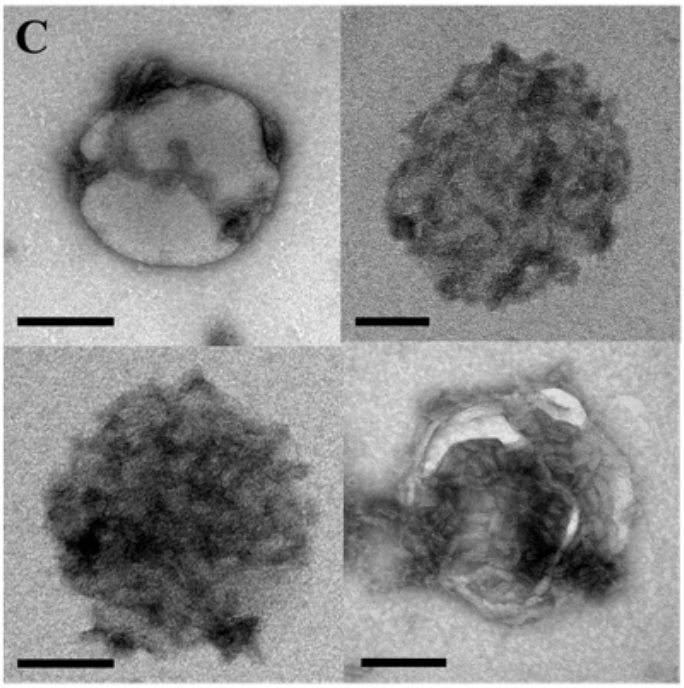

Figure 4.6: Triskelia on SUVs. Transmission electron micrographs of polymerised flat triskelia on SUVs. Scale bars 100 nm. From [239].

4.3.3 Triskelia on GUVs

The interaction of DNA triskelia with GUVs was studied using confocal, epifluorescence and TIRF microscopy. DNA dimers were allowed to interact with a small volume of GUV suspension. (The GUVs were electroformed in glucose or sucrose solutions at slightly less than 52 mM concentration, in order to be slightly deflated in 1×TE (1 mM Tris and 5 mM EDTA) + 14mM $MgCl_2$ buffer. This buffer was essential to maintain the triskelia's structure.) As previously described, DNA triskelia attached to the GUVs via insertion of the cholesterol groups, and were restricted to the outer leaflet only, as shown in Figure 4.7. Triskelia did not interact with vesicles encapsulated in GUVs during electroformation, and these vesicles are not visible in the DNA channel.

Dimers attached to the GUV were found to diffuse freely, and were distributed homogeneously over the surface of the GUVs. The fluorescence of the Alexa647-labelled origami was evenly distributed over the entire GUV, as depicted in Figure

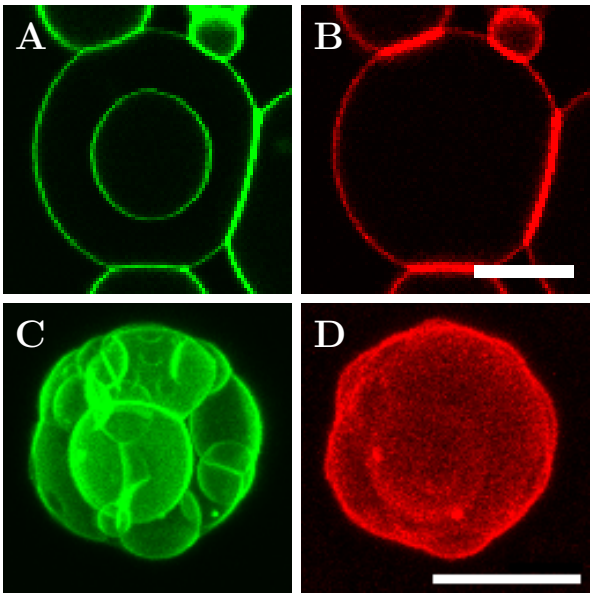

Figure 4.7: Triskelia on GUVs Triskelia attach to the outer leaflet of the GUVs but do not penetrate the membrane. (**A** and **B**) An Atto488-labelled GUV encapsulated within another GUV during electroformation is inaccessible to Alexa647-labelled DNA triskelia. The interfaces observed were formed after the insertion of the triskelia into the GUVs. (**C** and **D**) Interfaces within a cluster of GUVs formed after electroformation but before the addition of triskelia are also free of any Alexa647-labelled DNA. Scale bars 20 µm.

4.8 (B, D). The images on the left (green) show fluorescent lipids (Atto488 DPPE), and the images on the right (red) show the Alexa647-labelled triskelia.

Polymerisation was carried out by adding the polymerising staples at 10 times the concentration of the triskelia and incubating for at least 10 minutes. Upon polymerisation, the DNA triskelia aggregated into macroscopic domains, visible as discrete, diffusing entities on the GUV (Figure 4.8 C, D).

4.3.4 Triskelia on SLBs

DNA triskelia dimers were added to SLBs in 1×TE and 14 mM $MgCl_2$ buffer, and the system was allowed to incubate for at least 10 minutes. The SLB was then washed with 2 mL of the same buffer to remove triskelia which had not attached to the membrane. In contrast to their behaviour on GUVs, the diffusion of the dimers on SLBs was inhibited. Fluorescent recovery after photobleaching (FRAP) analysis showed that though lipids in the SLB were mobile, the triskelia were immobile (Figure

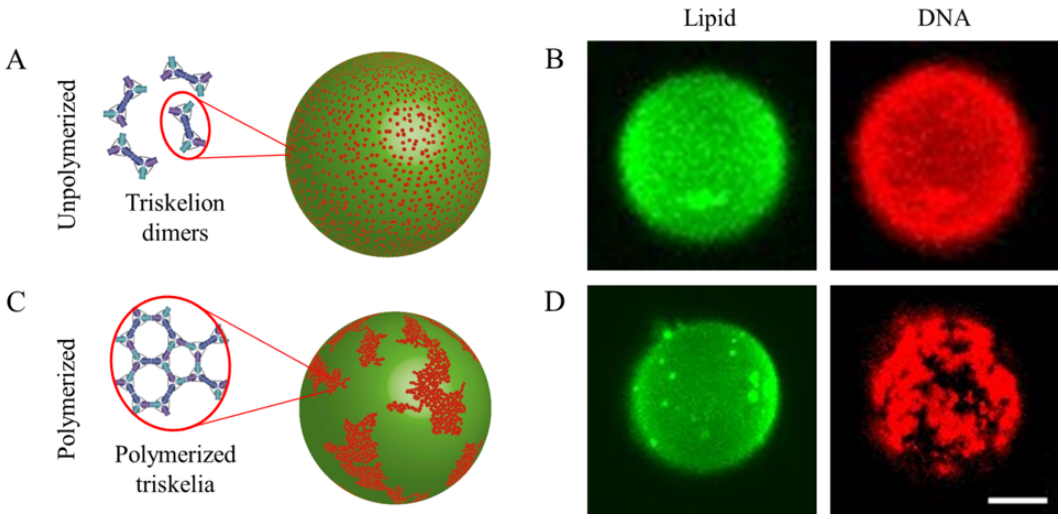

Figure 4.8: Distribution of DNA triskelia on GUVs. Unpolymerised DNA triskelia are homogeneously distributed on the GUV surface(Cartoon **A**). Polymerisation causes triskelia to form macroscopic domains(Cartoon **C**). (**B, D**) Confocal micrograph corresponding to a 500 nm-thick section at the top of the GUV. Triskelia polymerisation does not significantly affect the lipid distribution. Scale bar 10 µm.

4.9). Addition of polymerising strands did not affect the distribution of the triskelia; this suggests that triskelia mobility may be essential for polymerisation.

4.4 Membranes and triskelia at interfaces

4.4.1 GUV-GUV interfaces

After the addition of the triskelia to the GUVs, a number of vesicles were observed to have aggregated (Figures 4.10). This clustering has been attributed to the presence of the magnesium ions in the experimental buffer. Line scans (pixel intensities along a line passing through both GUVs and the interface, Figure 4.11) show that the intensity of the fluorescence signal of the lipids is the sum of the intensities of two individual membranes. However, the fluorescent intensity of the origami labels at the interface is greater than the sum of the intensities of individual triskelia-covered membranes. This suggests that the density of the triskelia at these interfaces is greater than the sum of the surface densities on individual membranes.

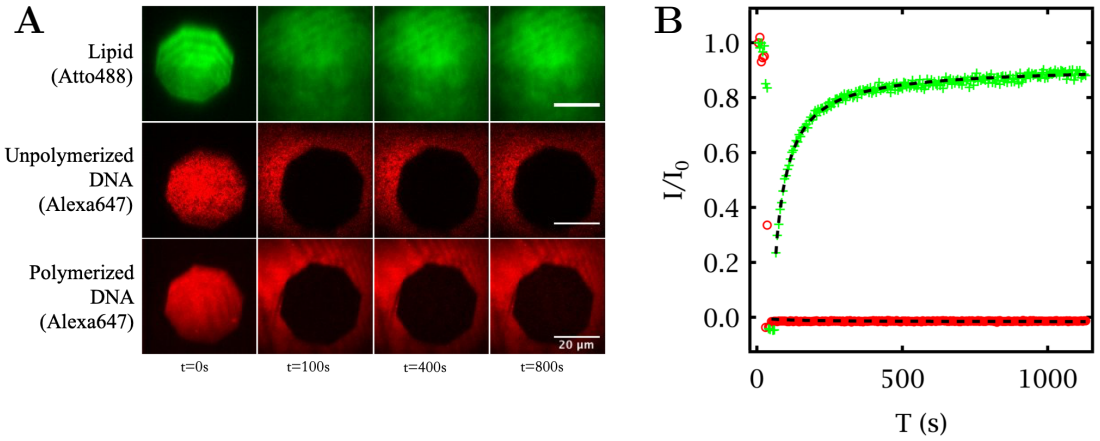

Figure 4.9: DNA Triskelia on SLBs Fluorescence recovery after photobleaching (FRAP) analysis of DNA triskelia bound to a SLB. (**A**) TIRF images of a typical FRAP experiment shows the bleaching pulse ($t = 0s$) for fluorescently labelled lipids (Atto488, *green*), unpolymerised and polymerised DNA (both Alexa647, *red*), and subsequent recovery of fluorescence. (**B**) Time-dependence of fluorescence intensities in bleached region. Fluorescently labelled lipids (green) are mobile, but triskelia (red), whether polymerised or unpolymerised, are immobile on the timescale of the measurement.

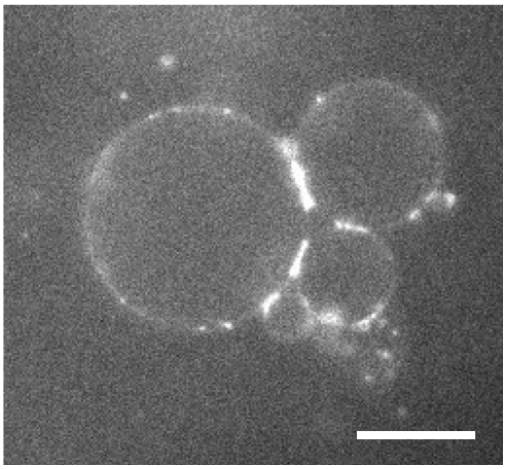

Figure 4.10: Aggregation of GUVs in solution. Addition of Alexa647 labelled triskelia to a suspension of unlabelled GUVs caused the formation of GUV clusters. This has been attributed to the magnesium present in the triskelia buffer. Scale bar 30 µm.

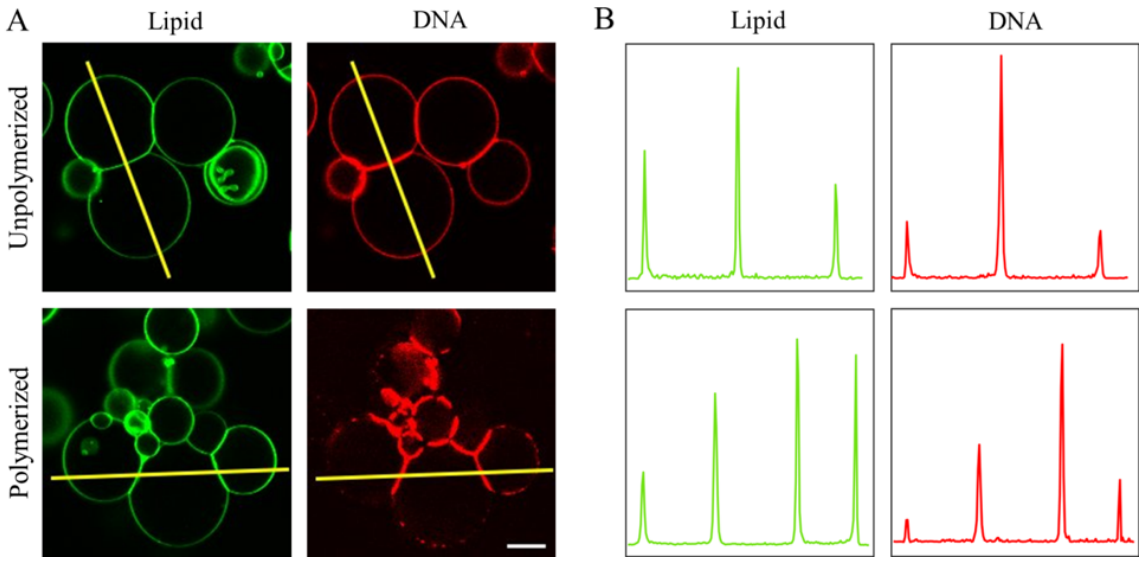

Figure 4.11: Enrichment of triskelia at GUV-GUV interfaces. (**A**) DNA triskelia are enriched at interfaces between GUVs both before and after the addition of polymerisation staples. Scale bar 20 µm. (**B**) Pixel intensity profiles along the lines depicted in (A) show the accumulation of both unpolymerised and polymerised triskelia at GUV-GUV interfaces.

4.4.2 GUV-SLB interfaces

Formation of GUV-SLB interfaces were driven by the combined effect of gravity and osmotic difference. The GUVs encapsulate sucrose solution, which, being denser than the surrounding TE buffer, causes them to sink in the experimental chamber. The osmolarity of the sucrose solution is slightly lower than that of the TE buffer. The resulting lowering of the membrane surface tension renders the vesicles floppy. The lower apical plane of the spherical GUVs comes in contact with the SLB, and an interface expands radially from this point of contact. The interface expands until the GUV membrane is taut again, in ~10^1 seconds. Freely diffusing triskelia on GUVs were excluded from these interfaces and accumulated at the interface boundary (Figure 4.12 A). Triskelia dimers added to the GUV-SLB system after the formation of the interface were also excluded from the interfaces (Figure 4.12 (D)), but also accumulated at the interface boundary. In contrast, polymerised triskelia on the GUVs inhibited the formation of these interfaces for at least several seconds, up to minutes. (Figure 4.12 B).

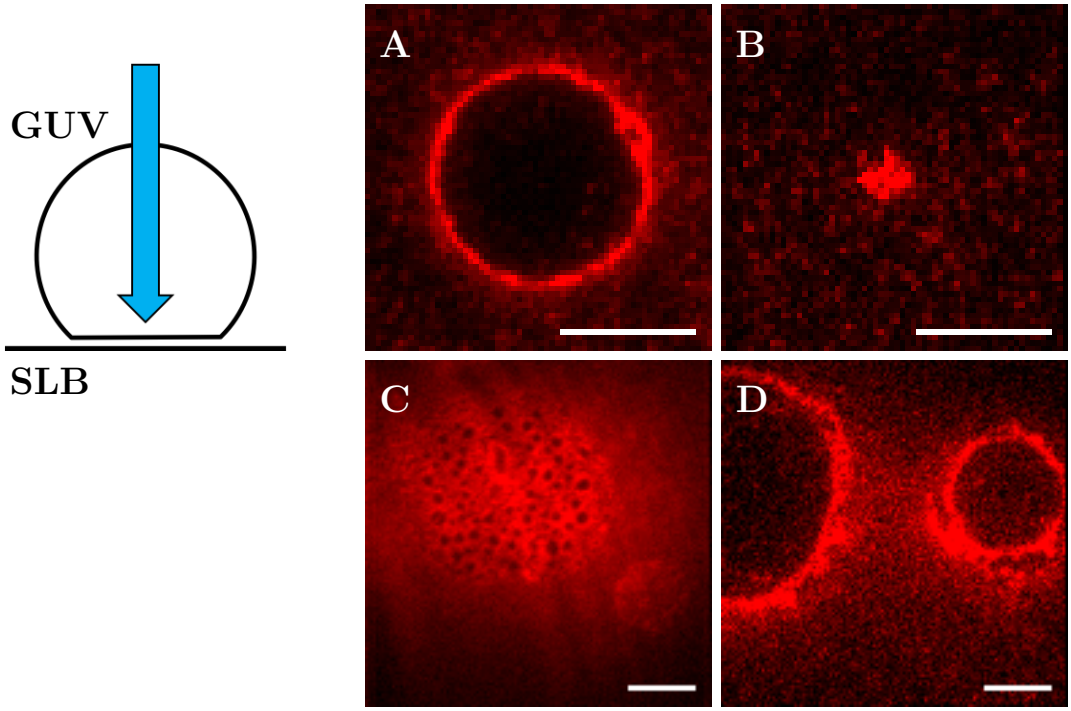

Figure 4.12: Triskelia at GUV-SLB interfaces. TIRF micrographs of fluorescently labelled triskelia at GUV-SLB interfaces: (**A**) Curved DNA triskelia added to GUV the before interface formation is excluded. (**B**) Flat DNA triskelia polymerised on the GUV inhibits interface formation. Only the point of contact between GUV and SLB is seen. (**C**) Unpolymerised curved DNA triskelia bound to the SLB prior to interface formation is trapped at the interface. The black spots are thought to be regions where the triskelia have transferred non-specifically to the GUV. However, this phenomenon was not observed consistently. (**D**) Flat DNA triskelia added after interface formation is excluded. Scale bars 10 µm.

When triskelia were bound to the SLB before GUVs were introduced, the contact formation between the two membranes only resulted in a partial exclusion of the triskelia from the interface (Figure 4.12 C). This is consistent with the inhibited mobility of the triskelia on the SLB. The dark patches visible in the interface in Figure 4.12 C are thought to be regions where the triskelia have been 'lifted' from the SLB due to interactions with the undulating GUV. While this is in line with the non-specific interactions of triskelia with GUVs (and the SLB), as discussed in Section 4.5.5, the phenomenon was not observed consistently.

4.5 Discussion

This chapter presents a study of the interaction of DNA triskelia with lipid bilayers. The triskelia were shown to successfully tether to membranes via cholesterol anchors. On monolayers, polymerisation of the triskelia were observed to cause nanoscale deformations of the membranes. On bilayer membranes, the triskelia were shown to diffuse, and could be triggered to form long-range assemblies that present as diffusive domains on the surface of GUVs. Electron microscopy showed that the triskelia confined to a 2-d surface assemble into lattices with hexagonal and pentagonal faces (akin to a flattened buckyball, or a truncated icosahedron, or a traditional football). These assemblies were also shown to modify intermembrane interactions, including the inhibition of synapses between some types of membranes.

4.5.1 Curvature effects of DNA origami

Triskelia both with and without intrinsic curvature were observed to induce similar blebbing in the monolayer membranes. However while the flat triskelion has no intrinsic curvature, the curved triskelion is much more curved than the blebs. Hence, it is unlikely that the intrinsic curvature of the triskelia array was forcing the membrane to conform to its shape. Instead, it is suggested that membrane deformation is caused by triskelion crowding. Polymerisation of the triskelia alters the distribution of triskelia so that there are regions of increased local density, where the triskelion lattice causes the membrane to curve away in order to reduce crowding. This is similar to reports of membrane curvature driven by protein crowding in biological systems [44]. Previous reports of DNA nanostructures on membranes typically force the membrane to conform to their intrinsic curvature via strong interactions [150, 241, 154, 155]. The data from the DNA triskelia instead gives credence to the shape-sensing, rather than shape-inducing role of similarly shaped proteins [242, 243, 244].

This work also aimed to design and test a DNA origami system to imprint curvature and induce budding on lipid membranes. To this end, the effects of flat and curvature triskelia constructs were studied on different types of membranes. TEM

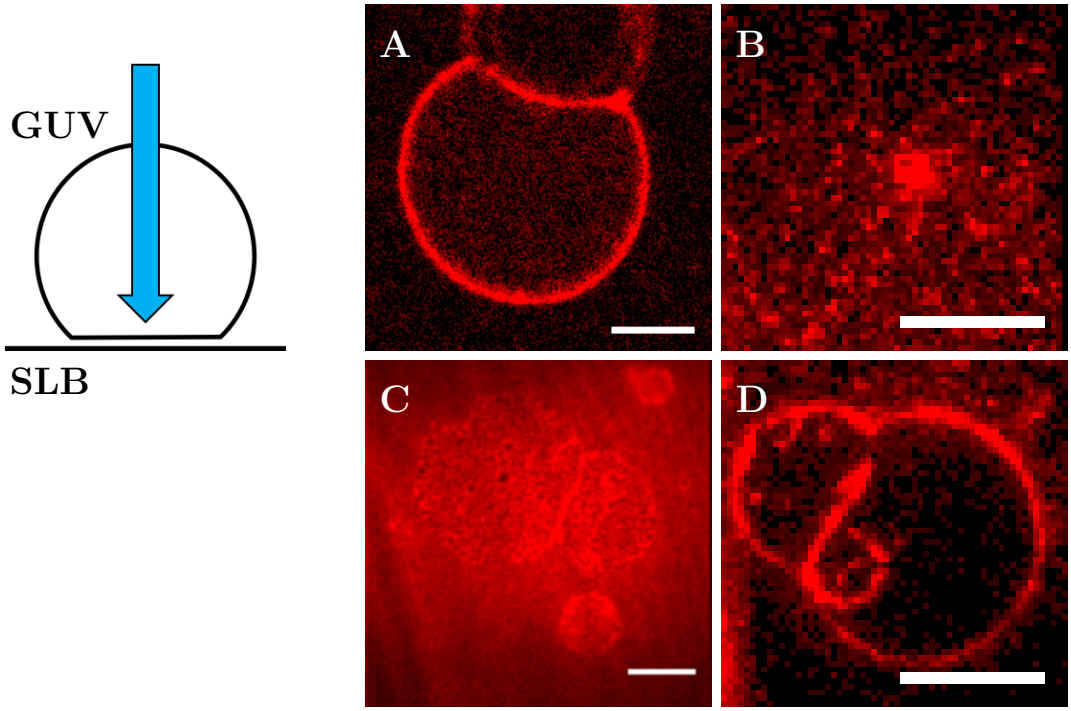

Figure 4.13: Effect of internal curvature is not observed. In comparable conditions (like Figure 4.12), changing the curvature of the origami triskelia do not alter DNA origami behaviour. (**A**) Confocal micrograph of flat triskelia DNA added to GUV before synapse formation being excluded from interface; (**B**) TIRF micrograph of curved DNA added to GUV and polymerised before synapse formation inhibits interface formation; (**C**) TIRF micrograph of flat DNA added to SLB before synapse formation is trapped at interface; (**D**) TIRF micrograph of curved DNA added after synapse formation is excluded from interface. Scale bars 10 µm.

data suggests that both constructs induce local deformations in lipid monolayers and SLB. Optical microscopy does not resolve these deformations, but reveals the behaviour of the triskelia on membranes. Figure 4.13 represents the same cases as Figure 4.12, but using curved instead of flat triskelia.

There were some instances of induced budding observed. At the boundary of interfaces between GUVs and SLBs, small vesicles were noticed with a corresponding increased density of concave triskelia (Figure 4.14). The highly curved GUV membrane at this boundary may be sufficient to drive membrane deformation by the triskelia. While it is also likely that the budding itself was driven by ionic effects, the triskelia may well be stabilising the curvature of these buds. In addition, triskelia with convex architecture were observed to drive and stabilise inward bud formation

in GUVs (Figure 4.15). However, these effects could not be reliably reproduced, and are therefore not discussed.

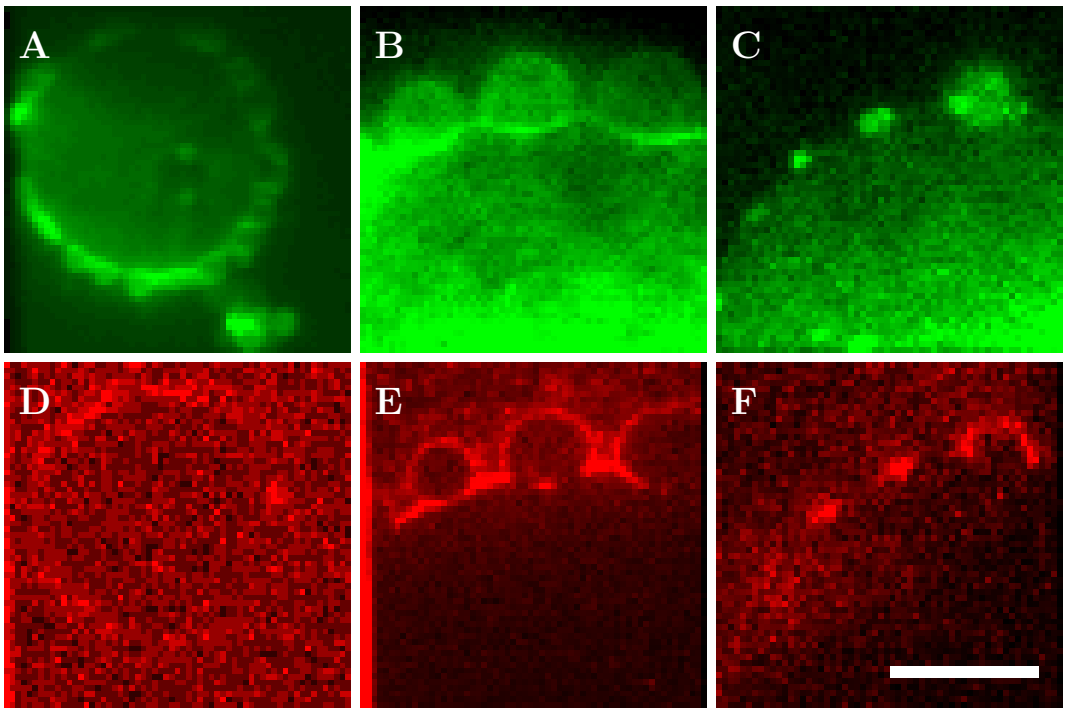

Figure 4.14: Budding at boundary of GUV-SLB interfaces TIRF micrographs showing budding at the boundary of a GUV-SLB interface. The GUV is labelled with Atto488 DOPE (top row) and functionalised with Alexa647 labelled origami (bottom row, vesicles correspond **A**-**D**, **B**-**E**, **C**-**F**). Triskelia accumulate at the interface boundary after being excluded from GUV-SLB interface, and the high curvature of the GUV at the boundary of the flat region drives membrane deformation. Scale bar 10 µm.

4.5.2 GUVs and triskelia

4.5.3 Magnesium and membranes

DNA is a polyanionic molecule, and large structures made of DNA tend to accumulate a large net negative charge. The presence of cations aids DNA hybridisation by shielding the charge and reducing electrostatic repulsion between adjacent DNA strands. The DNA origami triskelion therefore necessarily requires either large (molar) concentrations of monovalent cations, such as Na^+, or small concentrations (millimolar) of divalent cations, such as Mg^{2+} [245]. The DNA triskelia were synthesised, purified and obtained in a buffer consisting of 1× TE (1 mM EDTA and 5 mM Tris) and 12

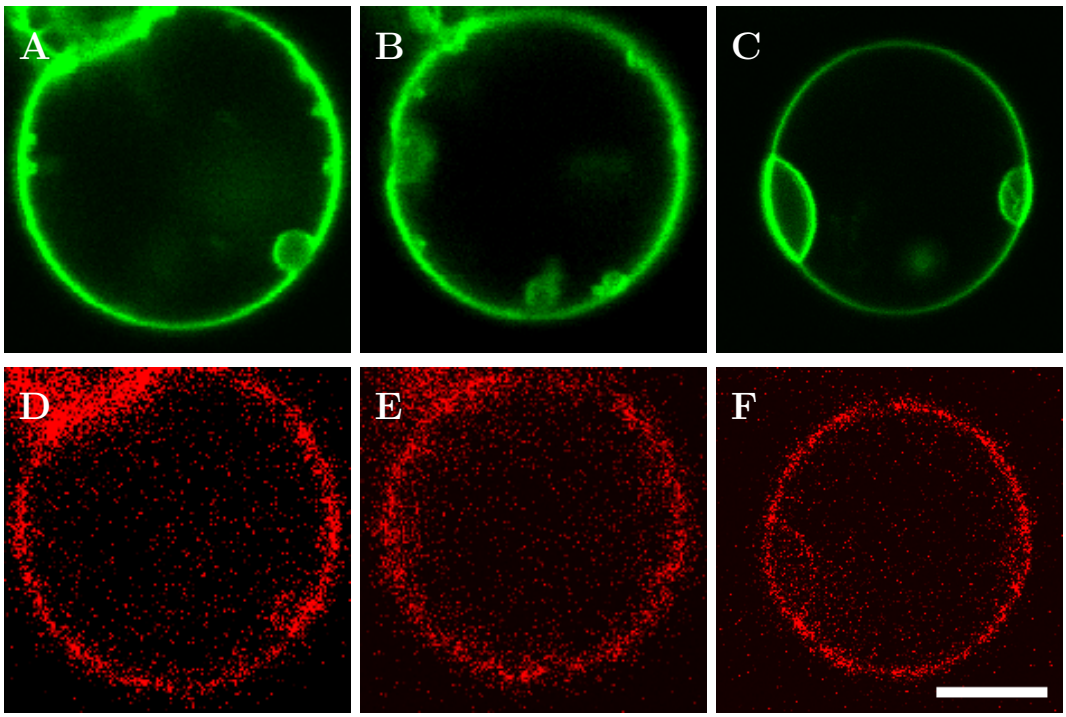

Figure 4.15: Budding due to inverted curvature triskelia Confocal images showing inwards budding on a GUV. Triskelia with convex curvature result in budding towards the inside of the GUV. The GUV is labelled with Atto488 DOPE (**A**, textbfB textbfC) and functionalised with Alexa647 labelled origami (**D**,**E**,**F**). Scale bar 10 µm.

mM $MgCl_2$. (Folding of DNA origami at high monovalent cation (Na^+) concentration was also attempted, but this resulted in a reduced yield of correctly folded triskelia.) Hence, in order to maintain this environment, experiments on GUVs were carried out by introducing them into the same TE-$MgCl_2$ medium. GUVs were formed in a slightly hypoosmolar solution of sucrose (~52 mM), so that the vesicles were slightly flaccid. This was done so as to reduce the energetic cost of locally deforming the membrane. However, divalent cations tend to disrupt bilayers in various ways. They cause bilayers to adhere to one another by acting as electrostatic bridges between the head groups of the apposing lipids. As a result, GUVs introduced to a medium containing even micromolar concentrations of Mg^{2+} ions tend to aggregate, as shown in Figure 4.16. In order to avoid this, a very small volume of the GUV suspension was diluted in the experimental buffer, allowing them to disperse far enough to avoid aggregation. In most experiments, an SLB was also used either to passivate the surface, or as an experimental condition. The effects of divalent ions on SLBs, as well as at

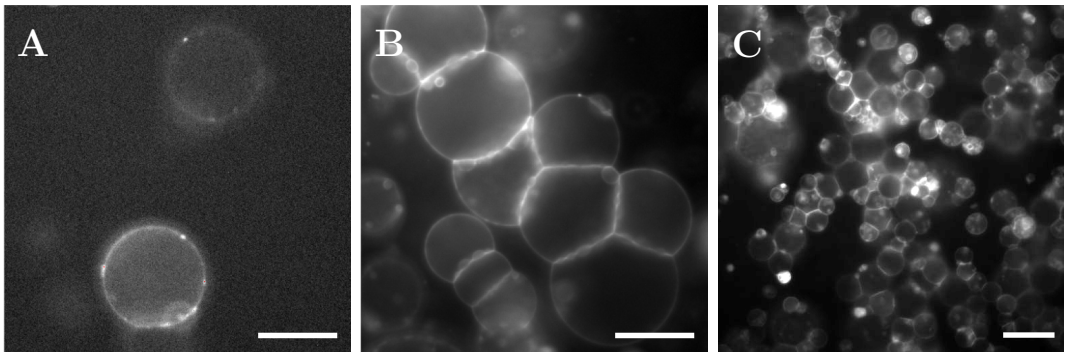

Figure 4.16: Effect of Mg^{2+} on DOPC GUVs (**A**) Divalent cations cause the appearance of lipid aggregates with unresolved structures on the surface of GUVs, observed as brighter fluorescent spots in the image.These are likely to be smaller vesicles which have detached from the same or other GUVs. In general, the presence of divalent cations cause GUVs to adhere and aggregate (**B** and **C**). GUVs of DOPC and 0.1% Texas Red DPPE were electroformed in 200mM sucrose and suspended in 100 mM NaCl, to which 10% v/v of 10 µM $MgCl_2$ was added. Scale bars 30 µm.

the interfaces between SLB and GUVs have been discussed in the previous chapter, and will be revisited.

4.5.4 SLBs and Triskelia

Origami on SLBs were observed to be immobilised. This has been attributed to the electrostatic interaction between the highly negatively charged DNA origami and the glass substrate. Polymerisation via staples was inhibited due to the reduced diffusion of the DNA on the membrane. DNA origami tethered to the SLB were found to remain trapped in the gravitationally driven interfaces formed between the SLB and GUVs.

4.5.5 Triskelia at interfaces

At interfaces between two GUVs, the DNA origami were found not only to have been trapped, but also enriched in comparison to the distribution over the rest of the GUV areas. The mechanism of formation of these interfaces is different than the GUV-SLB interfaces, because the interactions between the two GUVs were caused by the bridging effects of the Mg^{2+} ions in solution [190]. The rate of formation of these membranes is much faster than the displacement of the DNA origami due to

steric factors, leading to their being trapped. This sequestration is caused by the the triskelia interacting non-specifically with the apposing membrane, thereby mediating an attractive interaction between them [246]. Enrichment may be due to a passive diffusion-mediated process that traps the triskelia at interfaces [111]. This observation is corroborated by evidence that DNA origamis can bind to lipid membranes even in the absence of cholesterol anchors [247]. This enrichment at interfaces was also observed with polymerised triskelia (Figure 4.11).

The behaviour of DNA origami triskelia at interfaces between GUVs and SLBs are markedly different from their behaviour at GUV-GUV interfaces. Triskelia bound to the SLB were only partially excluded from the interface formed with introduced GUVs (Figure 4.12 C). This is consistent with the inhibited mobility of the triskelia on the SLB. Unpolymerised origami initially tethered to GUVs were excluded from the GUV-SLB interface. The action of the gravitational force on the denser GUVs was sufficient to displace the diffusing unpolymerised DNA on the GUV. Conversely, polymerised DNA origami on GUVs, being unable to escape from the interface, were observed to inhibit the radial expansion of the interface. Together, these suggest that the triskelia mediate a repulsive interaction between the two membranes. An explanation for this may be that the large span of the polymerised DNA stabilise membrane fluctuations at the initial contact region, preventing the membrane from flattening and spreading.

DNA triskelia showed diverse behaviours depending on which membrane they were initially bound to. This provides further confirmation that the interaction between DNA and membranes is directional, and that the cholesterol anchors insert into the first membrane they encounter.

Secondly, the SLB is planar and closely bound to a glass surface, whereas the GUV bilayer is constrained only by its natural elasticity and any residual difference in osmotic pressure across it. For a triskelion array to be incorporated at an interface requires significant distortion of the membranes. While this is possible at a GUV-GUV interface, the SLB is incapable of this distortion.

4.5.6 Experimental considerations

DNA functionalised with cholesterol is known to readily insert into membranes [129, 247]. The amount of DNA triskelia used per experiment were calculated such that at 100% insertion of the triskelia into the GUVs, the polymerised arrays would cover 10% of the total GUV area. Total available GUV area per experiment was calculated as previously discussed (Section 3.5.9). The suspensions were usually mixed and an incubation time of 10 minutes was allowed to pass, resulting in GUVs decorated with DNA triskelia. This mixture was then introduced to the experimental chamber.

Another important consideration is the ability of the optical techniques to resolve induced local deformation in the GUVs. There were numerous 'spots' of increased fluorescence signal observed on GUVs, which correspond to an increase in local lipid density, which in turn is indicative of a local deformation of the membrane. However, as discussed earlier, the specific action of the polymerising origami could not be isolated from the effects of the divalent cations present in the experimental medium, required to stabilise the origami structures. In addition, there was no observable budding away of vesicles, as was anticipated from the origami design. This suggests that additional machinery may be required to stabilise and drive neck formation and scission, similar to the role dynamin plays in in biological systems.

4.6 Summary

A DNA origami structural mimic of clathrin was designed, which can be programmed to to form extended arrays on lipid bilayers. These were observed to induce deformation in lipid monolayers, similar to the formation of clathrin coated pits. On GUVs, the polymerisation of the triskelia did not generate adequate force to deform the relatively low curvature GUV membrane. However, an interesting outcome was how triskelia modulated interfacial behaviour through a combination of hydrophobic functionalisation, electrostatic interactions and steric obstruction. This provides insight into the application of DNA origami on membranes as a cargo delivery mechanism, as well as for the design of geometries to mimic other membrane protein functions.

Chapter 5

Conclusion and Future Work

5.1 Conclusion

Interfaces between biological membranes are critical for the continued success of multicellular (and to a large extent, unicellular) life. Interactions and activities at interfaces are mediated by both membranes as well as interfacial protein machinery. The two critical parameters of intermembrane distance and protein size influence the spatial density and arrangement of membrane components, triggering downstream pathways. Transient interfaces are formed during the processes of membrane fission and fusion, such as during endocytosis, and special protein machinery is employed to induce curvature and initiate scission. All these processes are necessarily diffusion mediated, whether active or passive, and an understanding of mobility at interfaces is therefore critical.

This thesis presents two approaches, using DNA-based mimics of protein function, to the study of membrane diffusion. In the first, cholesterol-DNA linkers are used to restrict the membrane in proximity to a substrate. Tuning the cushioning and coupling effects provided a modicum of control over the diffusion in the GUV. It also showed that GUVs can be held in the fully cushioned equilibrium state, which could be developed into a platform to study (relatively) free lipid bilayers using TIRF microscopy, while maintaining the discrete environment of the GUV.

In the second approach, DNA triskelia were employed in an attempt to dictate membrane geometry through programmed self-assembly directly on the GUV. The

forces generated by this process were adequate to deform already highly curved membranes such as SUVs, but not large, low curvature GUVs. However, the very fact that these DNA constructs interacting with membranes via hydrophobic modifications can exhibit long range ordered behaviour opens up a range of applications ranging from artificial payload delivery systems to more refined mimics of protein function.

The most interesting results, though, were the interface modulation by the DNA origami, as well as the conformational organisation of the larger and more rigid DNA linkers. This demonstrates that the simpler system is capable of exhibiting complex behaviours, while also emphasising the important role of non-specific interactions in the intricately designed DNA origami system.

5.2 Future work and experimental wish-list

5.2.1 Quantification of electroformation efficiency

A major issue encountered in both projects was in estimating the surface density and/or area coverage of the DNA constructs on bilayers. Total available GUV area was estimated by selecting a representative aliquot of the GUV suspension, allowing it to settle on a passivated coverslip and manually evaluating contact area. However, even with automated counting of vesicles, this method is fraught with error. Moreover, there is scant literature on quantitative analyses of GUV yields, with most publications quite satisfied with "good" yields of "large" GUVs. It may therefore be quite useful to perform a quantitative, comparative analysis of some commonly used electroformation protocols varying in substrate material, ionic concentration, density, lipid, electrical settings, temperatures and chamber geometry. In the experience of this writer, every scientist that uses GUV electroformation tends to have strong and unique opinions on the merits of their personalised protocols. And justifiably so— individuals who require control over their GUV yields must establish their own rigorous and reliable protocols for electroformation, which once quantified, must be able to produce comparable yields of GUVs, in terms of lipid concentration, GUV volume density, size distribution and compositional homogeneity. Apart from

the optical method suggested above, GUV yield can be measured in terms of lipid mass converted into GUVs. One such method could be a surface-deposition sensitive technique such as quartz crystal microbalance (QCM). QCM techniques have been used to study the deposition of lipid bilayers on solid substrates [248, 70]. This could be adapted to measure the absolute mass of lipids in a representative volume of GUV suspension, thus providing an estimate of electroformation yield for a given set of parameters. Alternatively, chemical and colorimetric assays exist to measure different types of lipids in solution. For example, the Stewart assay measures phospholipid concentration by measuring the phosphate content in solution [249].

5.2.2 Fluorescent DNA assays of GUV-SLB interfaces

As reported in Chapter 3, DNA linkers shorter in length than the resting interface height between a GUV and an SLB tend to increase the coupling between the two membranes, observed in a decrease in lipid mobility in the GUV. Further, DNA linkers of lengths greater than the interface resting-height do not measurably change lipid mobility in the GUV. At the same time, unhybridised DNA strands were observed to have a cushioning effect on the GUV. These effects were attributed to changes in the separation between the GUV and the substrate, caused by a combination of steric and electrostatic effects. This provides a scheme to control the diffusive properties of the GUV membrane, while preserving its integrity. Maintaining the difference in aqueous buffer across a flat observation region will be useful for the study of proteins that facilitate transmembrane flux of materials. This can also be extended to the use of vesicles derived from biological membranes, such as giant plasma membrane vesicles (GPMVs). Such a system can act as a substitute for droplet interface In particular, this system can enable optical single-molecule studies of such systems. The use of lipids functionalised with polymers such as polyethylenegylcol (PEG) in lieu of DNA can be explored to isolate and control the effects of polymer size and net charge. In addition, the effect of grafting density on polymer orientation and its effects on lipid mobility need to be characterised.

Interface heights for different DNA species and hybridisation fractions need to be measured using interference microscopic techniques such as iSCAT or RICM. Alternatively, DNA linkers of different lengths can be selected to act as molecular rulers to accurately quantify membrane separation.

Another extension to this work lies in the originally envisioned study of size-based segregation of DNA linkers. Fluorescently-labelled DNA can be used to study the change in concentration of the spacers at the interface and observe the evolution of spatial domains. Preliminary work performed by the Michael Dustin lab using fluorescently-labelled DNA shows the formation at GUV-SLB interfaces of domains of DNA of differing lengths, including preliminary evidence of concentric domains, mimicking the behaviour of T-cell receptors at the immunological synapse [30, 116]. This partitioning system can also be used to pattern the planar region of the GUV to form interfaces of different separations.

The minimum effect of long DNA linkers on intermembrane separation is another interesting avenue of enquiry. It is theorised that this is due to the DNA adopting an entropically favourable tilted conformation. Further experiments are required to confirm this, and also to determine the effect of the tilt on membrane mobility. Simultaneously, the relation between linker length and tilt angle, as well as their effect on the interaction strength between the opposing strands, would need to be elucidated. The behaviour of singly anchored double stranded DNA longer than the membrane separation may also shed light on the behaviour of non-binding membrane components at biological interfaces. Similarly, the behaviour of doubly anchored single stranded DNA may prove useful as a model of elastic binding between membranes

5.2.3 DNA origami-based biomimics for membrane modification

Chapter 4 presented the interaction of triskelia dimers with lipid bilayers. Using electron microscopy, it was observed that flat triskelia formed arrays (consisting of hexagons and pentagons) on lipid monolayers. Curved triskelia produced shapes on the EM grid reminiscent of clathrin-induced budding. This budding behaviour of

curved triskelia was again observed on SLBs, indicating that the polymerised, curved DNA origami imparts a bending force on the membrane. On GUVs, the triskelia were observed to form extended 2-D arrays, but induced budding could not be successfully resolved. This suggests the role of additional assistive mechanisms may play a role in biological budding. Thus, this work represents an alternative biomimetic approach to understanding membrane deformation by proteins.

A possible extension of this work would be to design triskelia of varying curvature as a curvature sensing mechanism. For example, differently labelled flat and curved triskelia could effectively partition, respectively, to the apex and neck of incipient buds. Further, an obvious course of work would be to explore biological cargo delivery. The ability to form DNA cages that can reinforce vesicles may afford increased cargo lifetimes and increased precision in delivery.

Appendix A

Publications

Journot, C. M. A., **Ramakrishna, V.**, Wallace, M. I. & Turberfield, A. J. Modifying Membrane Morphology and Interactions with DNA Origami Clathrin-Mimic Networks. *ACS Nano* **2019**, *13* (9) 9973-9979, DOI: 10.1021/acsnano.8b07734.

Appendix B

Code

B.1 Python

B.1.1 GUI free TrackMate

Written by M.C. Blosser- Select target folder and launches the headless tracker.

```
import os #for making directories
from glob2 import glob
import tkinter.filedialog
from tqdm import tqdm
import time

#this is just a dialog to choose a folder
root = tkinter.Tk()
root.withdraw()
root.update()
file_path = tkinter.filedialog.askdirectory()
root.update()
root.destroy()

#.cine to your file type
paths = glob(file_path+'**/*.tif')
#print paths
#time.sleep(7200)
for i in tqdm(paths):
 tempName = i
 #print tempName
 #this kludges to be able to handle spaces in the path
 tempName = tempName.replace(' ','\ ')
 os.system('/Applications/Fiji.app/Contents/MacOS/ImageJ-macosx
     /Users/vivek572/Desktop/autoTracker/headlessTracker.py ' + tempName)
```

Adapted from a routine written by M. C. Blosser- Headless tracker

```
from fiji.plugin.trackmate import Model
from fiji.plugin.trackmate import Settings
from fiji.plugin.trackmate import TrackMate
from fiji.plugin.trackmate import SelectionModel
from fiji.plugin.trackmate import Logger
from fiji.plugin.trackmate.detection import LogDetectorFactory
from fiji.plugin.trackmate.detection import DogDetectorFactory
from fiji.plugin.trackmate.tracking.sparselap import
    SparseLAPTrackerFactory
from fiji.plugin.trackmate.tracking import LAPUtils
from ij import IJ
import fiji.plugin.trackmate.visualization.hyperstack.HyperStackDisplayer
    as HyperStackDisplayer
import fiji.plugin.trackmate.features.FeatureFilter as FeatureFilter
import sys
import fiji.plugin.trackmate.features.track.TrackDurationAnalyzer as
    TrackDurationAnalyzer
from ij.io import Opener
from ij import WindowManager
import fiji.plugin.trackmate.action.ExportTracksToXML as ExportTracksToXML
import fiji.plugin.trackmate.io.TmXmlWriter as TmXmlWriter
from java.io import File

opener = Opener()

imageName = sys.argv[1]
# Get currently selected image
imp = opener.openImage(imageName)


#Switch the z and t dimensions, which you apparently always need to do.
dims = imp.getDimensions();
imp.setDimensions( dims[ 2 ], dims[ 4 ], dims[ 3 ] );


#-----------------------------
# Create the model object now
#-----------------------------

# Some of the parameters we configure below need to have
# a reference to the model at creation. So we create an
# empty model now.

model = Model()

# Send all messages to ImageJ log window.
model.setLogger(Logger.IJ_LOGGER)
```

```
#-------------------------
# Prepare settings object
#-------------------------

settings = Settings()
settings.setFrom(imp)
###########################
#
#Note: all values must have a decimal point, to be interpreted as doubles
#
#*****************************SPOT DETECTION SETTINGS
    HERE*****************************
# Configure detector - We use the Strings for the keys
settings.detectorFactory = LogDetectorFactory()
settings.detectorSettings = {
    'DO_SUBPIXEL_LOCALIZATION' : True,
    'RADIUS' : 2.0,
    'TARGET_CHANNEL' : 1,
    'THRESHOLD' : 0.4,
    'DO_MEDIAN_FILTERING' : False,
}

# *****************************FILTER SPOT HERE*****************************
#Configure spot filters - Classical filter on quality
#filter1 = FeatureFilter('QUALITY', 0.004, True)
#settings.addSpotFilter(filter1)

#Add other feature filters here.
# Available Feature filters on
#
    https://github.com/fiji/TrackMate/tree/master/src/main/java/fiji/plugin/trackmate/fe
#

# Configure tracker - We don't want to allow merges and fusions
settings.trackerFactory = SparseLAPTrackerFactory()
settings.trackerSettings = LAPUtils.getDefaultLAPSettingsMap() # almost
    good enough
settings.trackerSettings['ALLOW_TRACK_SPLITTING'] = False
settings.trackerSettings['ALLOW_TRACK_MERGING'] = False

# Configure track analyzers - Later on we want to filter out tracks
# based on their displacement, so we need to state that we want
# track displacement to be calculated. By default, out of the GUI,
# not features are calculated.
```

```
settings.trackerFactory = SparseLAPTrackerFactory()
#settings.trackerSettings = LAPUtils.getDefaultLAPSettingsMap()
#*************************TRACK SETTINGS HERE*****************************
settings.trackerSettings['LINKING_MAX_DISTANCE'] = 5.0
settings.trackerSettings['GAP_CLOSING_MAX_DISTANCE']=5.0
settings.trackerSettings['MAX_FRAME_GAP']= 1
# The displacement feature is provided by the TrackDurationAnalyzer.
#****************************TRACK FILTER HERE*****************************
settings.addTrackAnalyzer(TrackDurationAnalyzer())
filter2 = FeatureFilter('TRACK_DURATION', 20, True)
#filter2 = FeatureFilter('NUMber_SPOTS', 20, True)
settings.addTrackFilter(filter2)

# Configure track filters - We want to get rid of the two immobile spots at
# the bottom right of the image. Track displacement must be above 10
    pixels.

#filter2 = FeatureFilter('TRACK_DISPLACEMENT', 10, True)
#settings.addTrackFilter(filter2)


#-------------------
# Instantiate plugin
#-------------------

trackmate = TrackMate(model, settings)

#--------
# Process
#--------

ok = trackmate.checkInput()
if not ok:
    sys.exit(str(trackmate.getErrorMessage()))

ok = trackmate.process()
if not ok:
    sys.exit(str(trackmate.getErrorMessage()))


#----------------
# Display results
#----------------

selectionModel = SelectionModel(model)
#displayer = HyperStackDisplayer(model, selectionModel, imp)
#displayer.render()
```

```
#displayer.refresh()

# Echo results with the logger we set at start:
model.getLogger().log(str(model))

outFilename = imageName.replace('.tif', '.xml')
#outputFolder = '/Users/MIWgroup/Desktop/trackertest/'
print(outFilename)
#outFile = File(outputFolder, outFilename)
outFile = File(outFilename)
#outfile = File(imp, trackmate)
ExportTracksToXML.export(model, settings, outFile)
print('hello!')
#ExportTracksToXML.export(model, settings, outFile)
#Make a copy of the first frame, and close everything else
IJ.run(imp,"Duplicate...", "duplicate range=1-1")
imp.changes = False
imp.close()
```

B.2 ImageJ background subtraction macro (Java)

```
var input_StackTitle = getTitle();
var MED_StackTitle = "MED_"+input_StackTitle;
run("Delete Slice");                          %% Use if shutter obscures
    first slice
run("Z Project...", "projection=Median");
imageCalculator("Divide create 32-bit stack", input_StackTitle,
    MED_StackTitle);
close(input_StackTitle);
close(MED_StackTitle);
rename("DivMed_"+input_StackTitle);
var output_StackTitle = getTitle();
saveAs("Tiff", output_StackTitle);
print(output_StackTitle);                     %%Lists all processed files
```

B.3 MATLAB

B.3.1 Track analysis

Written by M. R. Cheetham

```
function [MomentsOut] = AverageSecondMoment(TracksIn)
```

```
%AverageSecondMoment Calculate the scalar second moment as a function of
    dt,
%averaged over all tracks
%
%   MomentsOut = AverageSecondMoment(TracksIn)
%
%   Notes: TracksIn is a cell array, with one cell element per track. Each
%   cell element contains an N-by-3 or N-by-4 matrix. The columns should
    contain
%   Frame number, X-position, Y-position, and Intensity (optional),
    respectively.
%   MomentsOut{} is a cell array of 5 cells, which respectively contain
    {1} deltaT,
%   {2} scalar second moment, {3} uncertainty, {4} number of points
    averaged over, and {5} number
%   of tracks averaged over.

    NumSpots = cellfun(@(d) size(d,1),TracksIn);
    WaitHandle = waitbar(0, 'Calculating Average Second Moment');
    for SubLength = 1:max(NumSpots)
                                                % Set up a loop to count
        over dt for longest track (all other tracks will be covered by this
        loop)
        TempNum = 0;
                                                                % Reset
            temporary counters with each loop iteration
        TempTrackNum = 0;
        for TrackCounter = 1:length(TracksIn)
                                        % Loop over all tracks
            if SubLength <= NumSpots(TrackCounter)
                                        % Perform action if current
                sublength fits inside track
                for SpotCounter = SubLength:NumSpots(TrackCounter)
                            % Loop over possible starting points for
                    current dt (sublength)
                    TempNum = TempNum+1;
                    TempMoment{SubLength}(TempNum) =
                        ((TracksIn{TrackCounter}(SpotCounter,2)-...
                        TracksIn{TrackCounter}(SpotCounter-SubLength+1,2))^2)+...
                        ((TracksIn{TrackCounter}(SpotCounter,3)-TracksIn{TrackCounter}(Spo
                end
                TempTrackNum = TempTrackNum+1;
            end
        end
        %TempStDev{SubLength} =
            sqrt(mean((TempMoment{SubLength}-mean(TempMoment{SubLength})).^2));
            %Calculate Standard Deviation
```

```
        TempStDev{SubLength} = std(TempMoment{SubLength}); %Calculate
            Standard Deviation
        MomentsOut{1}(SubLength) = SubLength-1;
                                        % Time
        MomentsOut{2}(SubLength) = mean(TempMoment{SubLength});
                        % Second Moment
        MomentsOut{3}(SubLength) = TempStDev{SubLength}/sqrt(TempNum);
                 % Uncertainty
        MomentsOut{4}(SubLength) = TempNum;
                                             % Record Number of Points for
            current dt
        MomentsOut{5}(SubLength) = TempTrackNum;
                                          % Record Number of Tracks that have
            been averaged over
        waitbar(SubLength/max(NumSpots),WaitHandle)
    end
    close(WaitHandle)
end
```

Appendix C

DNA Origami schematics for CADNano

C.1 Triskelion sequences

Sequences of black staples on CaDNAno file: common to all the triskelia

CORE and VERTEX STAPLES

core_staple_45[95] 33[108]	GAG CAA CAG TTT ACT AGA AAA AGC CTG TTT AAT AAA GCT AAA GTA TTC AGC TAT TC
core_staple_53[102] 45[94]	GGA AGA GGT CAT TTT TGT TGA CCA GAA GCA AAA ACA GTA ATG CAG GTA A
core_staple_21[109] 25[101]	AGG CGG GGT TGA GGG TTC GTA CTC AGG AGG TAG AA
core_staple_69[70] 71[90]	GTA ACG TAG ATG ATT ACC TTT TAC ATC GCA GAA ATA GCT CAT TTC GAT C
core_staple_21[74] 13[69]	CGG CAT ATC GGC CTT GCC ATG GAA TGG ATT AGG CCA AC
core_staple_67[70] 69[83]	GGC GCA TAA ACA TAT TTG AAT TAC CTT TCA AAA GAG CCG GAA
core_staple_71[91] 73[112]	GGT GCG GAT TTG CAT ATA ATC CTG ATT GTA AAA GTG GTT TTC CCA GTT TT
core_staple_16[112] 21[108]	TTT CGC AGT CTC TGA TTT GAT GAT ACA GGT GCC TTG TAA G
core_staple_68[112] 83[112]	TTT AGG CTG CGC AAC GGG AAA CTG CGC TCA CTA TTA AAG AAT TT
core_staple_19[77] 27[80]	AGA GTA GCG TCA TAT ATA AAC TAT TCT GGC GCC GCT ACA GGG TTA G
core_staple_63[98] 69[112]	TAC ATA ATA TTC ATC ATT CGC CAT TCT TT

core_staple_70[112] 74[98]	TTT TTA CGC CAG CTG AAA GTG TCA TAG CT
core_staple_81[102] 58[95]	GTG TGG CCC TGA GAG AGA GAG TCC ACT GCC CGA AGC ATG CGA AAG ACG CCA GTT G
core_staple_30[58] 46[63]	CGC GCC TGA TAT TAT ACA GAG GCA AAA GAA TTC TTT CC
core_staple_25[91] 10[87]	CAC CCT CTT AGT ACA TAA GTG CCA CCA CCA GAG GCC ACC CTC TCA G
core_staple_27[81] 24[66]	TAA GTG AGA ATA GAA AGG AAC AAC CGT CTT TAC TG
core_staple_52[45] 40[52]	CAT GCG GTT TAT CAG CTT TGA CAA CTC GCT GAT AGG
core_staple_15[60] 22[63]	GCT TGG TAA TAA ACA GGA GGC CCT TAT GGT TAC CAC CAG GAA GGG
core_staple_32[72] 44[70]	TAA CCA GTA ATA AGA GAA ATT GAG AAT TAC GAA TCA TCT TTG ACC
core_staple_33[109] 38[102]	CAA GAG AAC AGA CTT GCT GCT ATT TTG CAC CAC TTT AAC TG
core_staple_42[112] 46[98]	TTT CCA CAT TCA ACT TCA GAA AGA TAG CG
core_staple_43[91] 45[112]	CAG TTG AAA CGC GCG TAC CGA CAA AAG GCA ACG CTC AAC ACT ATC ATT TT
core_staple_83[81] 80[67]	GTT AAA CCG TCT ATC AGG GCG ATG GGG TTG AGG T
core_staple_79[84] 60[73]	ATG CAT TGG GCG CCA GTC GGT TGT ACC ACT CAT ATT AGG AAC TTA AAT CAA AG
core_staple_23[84] 4[73]	AAT GCG GCG CCA CCC TCG TGG CGA GAA ACA CCC GCT CTG AAA ATA CCT AAA TT
core_staple_35[56] 48[59]	AAG GCT TCC AAT AGA ACC GGA AGG CGC AGG CTT GCG CAT
core_staple_33[67] 38[56]	TGT ACC GCG CAT CCG GTA ACG CTA ACG AGC GCC AGA ACC AAA GCT
core_staple_57[84] 64[84]	GAA GTA TAC ATT ATT CAT CAA CGT AAA AGG AGA AAA CCT GAG TTT AAT GCT TAG AA
core_staple_41[70] 43[90]	TAC CCA AAA TCA TTA GAA ACC AAT CAA TTC AAC AAT TGA AAG AGT TCA T
core_staple_29[77] 33[66]	CAC CGG ATT CTG ACC TAA ATT TAA TGG TTA AAT AAA TAT TTA TTT CGA GGT CCT GAA GCA
core_staple_74[97] 70[84]	GTT TCC TAT GCC TGA AAC GAC GGC CAG TTT GGG TAG GGG ATG
core_staple_5[98] 15[112]	TTA TTC ATA AGT TTT TGA CAG GAG GTT TT

core_staple_4[72] 16[70]	CAT ATT ACG CAG TAT GTA ACC GAG CAA ATA ATA CTG TCC ATC ACG
core_staple_54[112] 53[90]	TTT CGC AAA TGG TCA ATA ACC TGT TTA GCA TTT AGT CGG ATG GGC AAA CT
core_staple_49[109] 53[101]	GAA GAC TAT TGA TTA AGT AAT TCG AGC TTC AGT CA
core_staple_77[109] 81[101]	CCT ATT GCG TCT GTC GTG GGA GAG GCG GTT TAC CA
core_staple_78[62] 77[52]	TAT GAC CAT AAA GCC CCA GCA GGC GAA AAA TAG CCG GGT GAG TGA T
core_staple_5[109] 7[97]	AGG GGG AAT TCG TCA GAT AGC CCC CTT ATT AGC GTT AAA AGT TTG
core_staple_79[46] 80[35]	GCA ACT TTT GCG GGA GAA AGA ATT TTG ATG G
core_staple_14[83] 19[76]	ATA TTC AAA CCT ATA GTT AAT GCC CCC TGA GTA AA
core_staple_39[81] 39[69]	GAG GAC GTT GGG AAA TCA ACG TAA GAG TAG T
core_staple_24[65] 21[73]	AGT GAC GGG GAA AGC CGG CGA ACA CCA TGT ACC GTA ACC CAG ACG CGC GTA CAT TT
core_staple_24[45] 12[52]	CTA CGG AGC CCC CGA TTT CGA AAG GTC ACG CTT GGC
core_staple_1[77] 5[66]	AAT AAG ACA AAG TCA GAG GGT AAT TGA GGA GTT AAA ATA ATA ACT CCT TAT GGT TTC CGA
core_staple_57[77] 61[66]	GGA TTT ATA TCT AAA ATA TCT TTA GGA GGA TAA TAA AGA AAC TGA TTA TTT GCG TAG TAA
core_staple_77[74] 69[69]	ACA AGA GGA AGA TTG TAA TTT TTG GCC ATC ATG AGC GA
core_staple_12[112] 27[112]	TTT CCG CCA CCA GAA CCG TCG ATT GCT CAT GGG ATT TTG CTT TT
core_staple_39[70] 41[83]	AAA TTG GTC TTA CCA TTC TAA GAA CGC GTC GTA GGG AAA AAT
core_staple_70[83] 75[76]	TGC TGC ACA ACA TAA TTG TTA TCC GCT CGT CTG GA
core_staple_80[45] 68[52]	CTG TAG CAA AAT TAA GCA CTG TAA TAG GAT AAT TCG
core_staple_11[81] 11[69]	TGA CGC CAC CCT TAG AAC CCT TCT AGT CTT T
core_staple_82[112] 81[90]	TTT CGT GGA CTC CAA CGT CAA AGG GCG AAT GGA ACA TTG CAG CTG GTT TT
core_staple_26[112] 25[90]	TTT AAA CAA CTT TCA ACA GTT TCA GCG GAA TGA ATT TAG GAA CGA ACC GC

core_staple_13[70] 15[90]	AGA GAC ATT ACC ATA GGG AGG GAA GGT AAA TAG AAC ATT TTG ACC CGC C
core_staple_23[45] 24[35]	GCG GAG CGG GCG CTA GGG CCT AAA GAA CGC CT
core_staple_42[83] 47[76]	ACG CCA ACC CTC AAA TCG TCA TAA ATA TAC ACT AA
core_staple_11[70] 23[83]	AAT GCG CAT ACC GAG TAA TCA GTA GCG AAG CAC CAG AAC CGC TCA ATC GCG CGC TT
core_staple_75[77] 83[80]	GCA AAC AAG CTT GCG TGT GAA CGA GCC GGC ATG CCT GAG TAA TCC A
core_staple_80[66] 77[73]	TTG CCT CAG AGC ATA AAG CTA AAG GAA GCG GTC CAC GCT GTG TTG TTG TGT AGT TCC
core_staple_81[91] 79[83]	TCT TTT CGC GTA TTT CCA GTC TGT TGG GAA GGG TTT AAC CAA ATT TTA A
core_staple_25[102] 17[94]	CCG GAT AGC AAG CCC AAT TCT GTA GTA CCA GAA ACA TGG ACG ATT TTA A
core_staple_40[112] 55[112]	TTT ACA ACA TTA TTA TCA AAA AAT AGT CAT TAG ATA CAT TTT TT
core_staple_46[97] 42[84]	TCC AAT AGC GAG AGC CAG ACG ACG ATA AAG GCA TAA TAC ATA
core_staple_61[98] 71[112]	GGA TTC GCA AAA TTG CCT CTT CGC TAT TT
core_staple_1[84] 8[84]	GCA AGA AAG AAG GAT AGC AAA CAC AAT CAA TAT TGC ACC AGT CAG AAT CCA TCG CC
core_staple_43[60] 50[63]	AAC GCT CCA TTT CAT GAG GAA GAT AAA GAC AAG GGA GTA GTT GCG
core_staple_5[67] 10[56]	TTG TAG CAA GCA GCA CCA CGA ACC ACC AGC AGG CTA TTG ACC TGA
core_staple_63[56] 76[59]	ATT TAA CAC ATC AAT TAA ATG AAA ATA AAA ATT TTT TCA
core_staple_15[91] 17[112]	GCC AGC AAT TTT GTC GTA GAA AAT ACA TCG AAC AAC AGA ATG GAA AGT TT
core_staple_67[81] 67[69]	ACC CCG CTT CTG AAC CCG TCG GAT GTA GAT G
core_staple_60[72] 72[70]	AAA CAG ATG ATG GCA ATC ATT TTG GAT TAA GGC CAA GAG AAT CGA
core_staple_41[84] 35[97]	CTA CGT TCA GTC AGA TGG TTT AAT TTC ACA GCT ACT TAG CGA
core_staple_52[65] 49[73]	AAT AGG TGA ATT TCT TAA ACA GAA CTT AGA GCT TAA TTC TGC GAA AGC AGC GTG AA
core_staple_22[62] 21[52]	AAG AAA GAG AGC TTT TCG TCA CCA GTA CAT CTA AAC GAG CAC GGG A

core_staple_14[112] 18[98]	TTT TGA GGC AGG TCA AAA GTA TAG TAA CA
core_staple_76[58] 80[46]	AAA CGA GAT AGC CCA CTA CGC CCA AAT CAA GTC AAA AGA TC
core_staple_49[74] 41[69]	TCC AAA ATC CGC GAC CTC GAA CTG ACA GAC CTA TTC AT
core_staple_18[97] 14[84]	GTG CCC GCA TGG CTA TTT ACC GTT CCA GAT CCT CAG GCC TTG
core_staple_20[58] 24[46]	TGA GTT TTG TTA AAG GAA TTG TTT TTT CAC GCG TAA CGA AA
core_staple_51[84] 32[73]	GCG GGC GCC AGA CCG GCT TGA TAC CGA TTA AAG GCA CGG TGT ACC AAC TTA GA
core_staple_33[98] 43[112]	CCT TAT CAA TGC AGG ATT TAG GAA TAT TT
core_staple_44[112] 49[108]	TTT AAC CCT CGT TTA GCT TTT GCA AAA GAT AGA CTG ACG A
core_staple_2[58] 18[63]	AAT TGA GTA GAC CGT TGT CAG TGA GGC CAC CGC GAT TA
core_staple_17[95] 5[108]	AGC AGT TAC CAC AAT GAA ATA GCA ATA GCT AAG ATA GCA CAT AAA CAC GGA ATT AA
core_staple_7[56] 20[59]	TCG ATA GGC CGG AAA CAT TCT TTT ACA TGC GCG TAG CTT
core_staple_53[91] 51[83]	CCA ACA GAA GCG AAG ATT GCA CAG GTA GAA AGA GAC AGA TGA CGC TTT T
core_staple_47[77] 55[80]	AAC ACA CCA AAA TAC TGC GGA ATG CTT TAG ATC GTC ACC CTC CGA G
core_staple_69[84] 63[97]	ACC AGG CTC CGG CAG TGC ATC TGC CAG TAT TTT CCG AAA CAG
core_staple_29[84] 36[84]	ATC ATA AAG GGC TTA TAT AAA CTG TTT AAA TCG GCA TTT TCA AGG CGT TAA TTT TA
core_staple_51[45] 52[35]	TCG GAA CCA TCG CCC ACG ATT GTA TTT TTA AA
core_staple_58[58] 74[63]	AGA TCA GAA ATA ATC GTG TCA TTG CCT GAG AAC CTG AT
core_staple_58[94] 61[108]	AGT ATA GAC TTT ACA AAC AAT TCG ATT AAT TTT TTG GAT ACC ATA TCC TG
core_staple_7[98] 13[112]	CCT TTA GAG AGC CAC CAC CCT CAG AGT TT
core_staple_72[112] 77[108]	TTT CAC GAC GTT GTA CAG GTC GAC TCT AGT CAT GGT AAA G
core_staple_71[60] 78[63]	TAA TAA GCA ACA ACC GTT CTA GAA GTA AAG ATA GAA CCA AAA CAT

core_staple_50[62] 49[52]	CCG ACA AGC TTT CGA TAA TGC TGT AGC TTA TAA CAA ACG AGG AGA C
core_staple_55[81] 52[66]	TAG TAT ATT TTC ATT TGG GGC GCG CCC AAT TGC TG
core_staple_48[58] 52[46]	CGG GTT GAT TAG CTG AAA AGT TCT ACT AAT ACA TTC CAC AA
core_staple_35[98] 41[112]	ACC TCC CAG CAA GCC GAA CTA ACG GAT TT
core_staple_61[109] 67[101]	ATT GGC GAA TAT CAA TAG TCG CTA TTA ATT ATT GA
core_staple_61[67] 66[56]	CAG GAA ACA AAA TTT CAG CGA TAG CTT AGA TCG TTG GTT CTC CGT
10[123]11[123] -not in contact	TTT GAA CCA GAG CCA CCA CAT AAT CAA AAT CAC CGT TT
38[123] 39[123] -not in contact	TTT TAT GCG ATT TTA AGA ATC ATT GTG AAT TAC CTT TT
66[123] 67[123] -not in contact	TTT GCC TCA GGA AGA TCG CGA CGA CGA CAG TAT CGT TT
triskelion_vertex 6T_ 21[53] 2[42]	GCT ATC CAG AAC TTG CCA CCC AAA AGT TTT TT
triskelion_vertex_6T_ 68[51] 58[59]	CGT AAA ATT CAG GTT TAA CTT TTT TTT TTT TAT TAT CAT CAT ATT CCC ACC
triskelion_vertex_6T_ 79[27] 82[21]	TTT TTT CCT TTA TTT GGA GAC ATT ATA AAT TTT TTG GGG TCG AGG TGC CG
triskelion_vertex_6T_ 12[51] 2[59]	AGA ACA GGA ACC AAA GAC ATT TTT TTT TTT TAA CTG GCA TGA TTA AGA CGG
triskelion_vertex_6T_ 46[62] 44[31]	ATT AAA CGG GTA AAA AAC GAA CAA GCG CGA AAC AAA GTA CTT TTT T
triskelion_vertex_6T_ 83[28] 74[27]	AAA TCC CGT TTT TTT TTT TTT CAA ATC ACC GCT ATT TTT TTT TTT
triskelion_vertex_6T_ 73[31] 70[31]	TTT TTT TAT GTA CCC CGG AAT TGT AAA CGT TTT TTT
triskelion_vertex_6T_ 9[42] 11[80]	TTT TTT ACA GAG GTG AGG CGG TCA GTA TTA ACA CCG CCT GCA AAT TAA AAG AAC
triskelion_vertex_6T_ 23[27] 26[21]	TTT TTT CTG GCA AGT GTG CTT TTA GTT AGT TGA AAA TCT CCA AAA AAA AG
triskelion_vertex_6T_ 74[62] 72[31]	AAA TTA ATG CCG GAC TAT CAG AAA ACT AGC ATG TCA ATC ATT TTT T
triskelion_vertex_6T_ 18[62] 16[31]	AAG GGA TTT TAG ACT TTA TAA TAG CAA TAC TTC TTT GAT TTT TTT T
triskelion_vertex_6T_ 19[27] 23[44]	TTT TTT AAT CCT GAG AAG TGT TAG GAA CGT CAG AGC GTA TAA CGT A

triskelion_vertex_6T_41[31] 38[31]	TTT TTT CAA GAG TAA TCT CAG TGA ATA AGG TTT TTT
triskelion_vertex_6T_51[27] 54[21]	TTT TTT TAA CCG ATA CGG CTA CGA AGT TTG TAG TAG CAT TAA CAT CCA AT
triskelion_vertex_6T_65[41] 67[80]	TTT TTT GAG AAG AGT CAA TAG TGA ATT TAT CAA AAT CAT AGG TTC CTT GAC GTA
triskelion_vertex_6T_55[28] 46[27]	GTG TCT GAG TTT TTT TTT TTT AGG CTT TGA ATG CCA CTA TTT TTT
triskelion_vertex_6T_69[31] 66[31]	TTT TTT TAG CCA GCT TTC AAC GGC GGA TTG TTT TTT
triskelion_vertex_6T_77[53] 58[41]	ATT ATA TTT ATT GAT AAA GGA GCG GAT TTT TT
triskelion_vertex_6T_27[28] 18[27]	GCC CTC ACC TTT TTT TTT TTT TCG TTA GAA GTA CGC CAG TTT TTT
triskelion_vertex_6T_47[27] 51[44]	TTT TTT CGA AGG CAC CAA CCT AAT ACG TAG GAC TAA GTA GCA ATA T
triskelion_vertex_6T_17[31] 14[31]	TTT TTT AGT AAT AAC ATC ACA ATA TTA CCG TTT TTT
triskelion_vertex_6T_37[41] 39[80]	TTT TTT AGC CTA ATT TGC CAG TTA CAA AAT AAA CAG CCA TAT TTC CTG AAG CTT
triskelion_vertex_6T_40[51] 30[59]	CTG AAT CAT AAA ATA ATA TTT TTT TTT TTT TAT TTA GGC AGA GGC ATA CAA
triskelion_vertex_6T_49[53] 30[41]	TTT GTT ACT TTA TCA TCC AAC ATG TAT TTT TT
triskelion_vertex_6T_29[41] 28[41]	TTT TTT GTG ATA AAT AAG GCG TTT GAA ATA CCG ACC GTT TTT TT
triskelion_vertex_6T_15[31] 12[31]	TTT TTT CCA GCC ATT GCA TTC ACC AGT CAC TTT TTT
triskelion_vertex_6T_43[31] 40[31]	TTT TTT GCG CAG ACG GTC GCT GAC CTT CAT TTT TTT
triskelion_vertex_6T_75[27] 79[45]	TTT TTT GAG AGA TCT ACA AAG GGA GGG TAA TCA ATA AAA GGC CCA AC
triskelion_vertex_6T_1[41] 0[41]	TTT TTT ATA ACC CAC AAG AAT TCG CTA ATA TCA GAG AGT TTT TT
triskelion_vertex_6T_13[31] 10[31]	TTT TTT ACG ACC AGT AAT AGA ATA CGT GGC TTT TTT
triskelion_vertex_6T_57[41] 56[41]	TTT TTT ATT AGA GCC GTC AAT ACA CTA ACA ACT AAT AGT TTT TT
triskelion_vertex_6T_45[31] 42[31]	TTT TTT AAC GGA GAT TTG AGC CGG AAC GAG TTT TTT
triskelion_vertex_6T_71[31] 68[31]	TTT TTT TAA TAT TTT GTT CTG GCC TTC CTG TTT TTT

triskelion_vertex_6T_66[55]71[59]	GGG AAC AAT CAA CAG AAA ACA AAT TTT TTT TTT TTG TCA GAT GAA TAT ACA GAT TTT CGC AT
triskelion_vertex_6T_10[55]15[59]	AAG CGT AAA AAG GGA CGT CAC CAT TTT TTT TTT TTA AAG GGC GAC ATT CAA ACC AGC GAA AC
triskelion_vertex_6T_38[55]43[59]	GCT CAT TTG ACA AGC AAG CAA ATT TTT TTT TTT TTC CCA TCC TAA TTT ACG ACA AGA AAG GG
extra_support_25[21]22[27]	CAC TAA ATC GGA ACC GTT TTT T
extra_support_53[21]50[27]	AAA AGG AGC CTT TAC ATT TTT T
extra_support_80[34]55[27]	TGG TTC CGA AAT TTT TTT TTT TTT TGT ACG
extra_support_52[34]27[27]	TAT GCA ACT AAA TTT TTT TTT TTT TTA GAC A
extra_support_81[21]78[27]	ATA CAG GCA AGG CAA GTT TTT T
extra_support_24[34]83[27]	GTA GCA TTC CAC TTT TTT TTT TTT TTC GGC A
78[127]79[127]	AAT CGG CCA ACG CGC GGC CAG CTG CAT TAA TG
50[127]51[127]	TTC AAA TAT CGC GTT TAG GAA GCC CGA AAG AC
22[127]23[127]	GGA ATA GGT GTA TCA CGA TAT AAG TAT AGC CC

STIFF BRIDGES

Common to both flat and curved bridges

Arm1_1_HB84	CGC CGG AGA CAG AGA GAA CCG CCA ACG TGT TCC ATC ATA ACT TAA CAC TTC CAG ACT GGT CG
Arm1_2_HB84	CGC GGA AGT CCT ACC GAC CAA CGC AGG ACA CAT GAG GTC GAG TGC GGC AGT TGT TGT GCG
Arm1_3_HB84	CGC TTC TTC TGT ACT ATC TCT GTC GCA CGC CGA CTA TAA CTA CTG TTG GTA CAA TGG CCG
Arm2_1_HB85	CGG TTC CTA GAC CTA AGT AGA GAT CCG AGA GTC TCA GGT GCC TCT ATG ACC GAG TCC TAC CG
Arm2_2_HB85	CGC TCG GAG CGC AAT GCA ACT CCG GAC CAA CTG TGG ATC CTG TCG TCG GAC CGG ACT GCG

Arm2_3_HB85	CGT GCA TTC TCG CCA TGT TCC GTC AGT ACA AGT TGA AGA GTC GGT CAC GTT AGA ACA ACG
Arm3_1_HB87	CGC CTC ACT AAC ATG TAA GTG TAA TTG AAT GTG AGA TTC AGC TCG AGA GAC TAA CAC ACA GC
Arm3_2_HB87	GCG CTG TCG TGC CGC ACG TGT AAG TAA GGT TAG CGT ACT GAC AGG TCG AAC CGG CGC TGC
Arm3_3_HB87	GCG GTC CAG TGA CCG CCA TTC GGA CCG CTC TCA CAC ACA CGA ATA ACG AAG TCA AGG TGC
Arm1_2*_HB84	CAA CAC TAG GTT GGG TTA TAT AAC TAT ATG TGC GAG AAA ACT TTT TCA AAA CAC GT
Arm1_3*_HB84	TGG CGG GAC TTC CGC GCG GCC CCT GCG TTG GTC GGT AGT TCT CTC TGT CT
Arm1_4*_HB84	TTT AAC CTC CGG CTT AGT TAT AGC CGC ACT CGA CCT CAT GTG TAT TGT AC
Arm2_2*_HB85	GTG ACC GAA TCT AAA GCA TCA CCT TGC TGA ATG GTC AGT TGG CAA ATC ACT CTC GG
Arm2_3*_HB85	ATC TCC GCT CCG AGC GCG TTG CTC CGG AGT TGC ATT GTA CTT AGG TCT AG
Arm2_4*_HB85	CAG CAG CAA ATG AAA ACT CTT CCG ACG ACA GGA TCC ACA GTT CTT CTA AC
Arm3_2*_HB87	CGT TAT TGT TTA ACG TGA AAA ATC AAA ATA GCA GGG AAG CGC ATT AGA CCA TTC AA
Arm3_3*_HB87	TTA CAC ACG ACA GCG CGC ACC TTA CTT ACA CGT GCG GCT TAC ATG TTA GT
Arm3_4*_HB87	AAG AAA CGA TTT TTT CGT GTG TCG ACC TGT CAG TAC GCT AAC CTT GAC TT

Strands specific to flat bridges (92 bp long)

Arm1_1*fl_HB84	CCG GCG CGA CCA GTT AAG TTA TGA TGG CAA ATA TAT TTT AGT TAA TTT TTA AGT GTC TGG TTT
Arm1_5*fl_HB84	GAG ACT ACG AGA TAG GAA GAA GCG CGC ACA ACA ACT GTC GGC GTG CGA CAC TTT TT
Arm2_1*fl_HB85	GAA CCG CGG TAG GAG AGG CAC CTG AGA ACA GTT GAA AGG AAT TGA GGA TTG TCA TAC TGC TTT
Arm2_5*fl_HB85	GCC ACG CTG AAC ATG GAA TGC ACG CGC AGT CCG GTC AAC TTG TAC TGA CGG AGA GC
Arm3_1*fl_HB87	GAG GCG GCT GTG TCG AGC TGA ATC TCA GGG AGA ATT AAC TGA ACA CCC TTT CTC TGT TAC TTT

Arm3_5*fl_HB87	ATC CCA ATA ATG GCG CTG GAC CGC GCA GCG CCG GTT GTG AGA GCG GTC CGC CAA AT

Strands specific to curved bridges (84 bp long)

Arm1_1*cu_HB84	CCG GCG CGA CCA GTT AAG TTA TGA TGG ATA TAT TTT AGT TAA TTT
Arm1_5*cu_HB84	GAG ACG AGA TAG GAA GAA GCG CGC ACA ACA ACT GTC GGC GTG CGA CAT ACC TT
Arm2_1*cu_HB85	GAA CCG CGG TAG GAG AGG CAC CTG AGA GTT GAA AGG AAT TGA GGA
Arm2_5*cu_HB85	GCC ACG AAC ATG GAA TGC ACG CGC AGT CCG GTC AAC TTG TAC TGA CGG CTG AG
Arm3_1*cu_HB87	GAG GCG GCT GTG TCG AGC TGA ATC TCA AGA ATT AAC TGA ACA CCC
Arm3_5*cu_HB87	ATC CCA ATG GCG CTG GAC CGC GCA GCG CCG GTT GTG AGA GCG GTC CGA AT

DIMERISATION STRANDS 3T (6 bp and 3T spacer arm 1-1)

2[121]1 [133] 1<->1, 6bp TTT	AAA AGT AAG CTC TTA CCG AAG CCC TT T TTT CGG CA
4[121]3 [133] 1<->1, 6bp TTT	GCA AAG ACA CGG TGG CAA CAT ATA AA T TTC CGA CT
6[121]5[133] 1<->1 , 6bp TTT	TGA GCC ATT TTG AAT TAT CAC CGT CA T TTA GAA AC
8[121] 7[133] 1<->1, 6bp TTT	TTT TCG GTC ACT GTA GCG CGT TTT CA T TTT TTA AG
20[121]21[133] 1<->1, 6bp TTT	TTA GGA TTA GCT GAG ACT CCT CAA GA T TTG GAA TA
22[121]23[133] 1<->1, 6bp TTT	GGT GTA TCA CGA TAT AAG TAT AGC CC T TTG AAG GA

POLYMERISATION STAPLES (6 bp sticky ends arm 2-3)

30[133]29[133] 2<->3, 6bp	AGT CTG AC AAA TTC TTA CCA GTG TAT CAT ATG CGT TAT CAG TCA
32[133]31[133] 2<->3, 6bp	GCA CTG GA CAA TAA ACA ACA TGA TTC TGT CCA GAC GAC TAA CCG
34[133]33[133] 2<->3, 6bp	CGT GAT AA GTA CCG CAC TCA TCG AAC GGG TAT TAA ACC ATG CTC
36[129] 35[129] 2<->3, 6bp	TTT TTA AAT CAA GAT TAG TGG GAG GTT TTG AAG CC T AGC CA

48[133]49[133] 2<->3, 6bp	GGA CGT AT CAG GTC TTT ACC CTT GAC CAT AAA TCA AAA TCG TCC
50[133]51[133] 2<->3, 6bp	TTT TTC AAA TAT CGC GTT TAG GAA GCC CGA AAG AC C GCA TG
58[133]57[133] 3<->2, 6bp	CAG ACT CT TTG CCC GAA CGT TAC AAC TCG TAT TAA ATC TGA CTG
60[133]59[133] 3<->2, 6bp	CAG TGC GG AAG GGT TAG AAC CTT ATA CTT CTG AAT AAT CGG TTA
62[133]61[133] 3<->2, 6bp	ATC ACG TA CAA AAT CGC GCA GAG CTT TGA ATA CCA AGT GAG CAT
64[129] 63[129] 3<->2, 6bp	TTT CTT GCT TCT GTA AAT CTA TGT GAG TGA ATA AC T GGC TA
76[133]77[133] 3<->2, 6bp	ACG TCC GA GCT AAC TCA CAT TAG GGG TGC CTA ATG AGT GGA CGA
78[133]79[133] 3<->2, 6bp	TTT AAT CGG CCA ACG CGC GGC CAG CTG CAT TAA TG C ATG CG

DYE HANDLES

80[118]81[120] 5'-handle	TGC GAT ATT GCA TTA ATG CCC TTC ACC GCC AGA CGG GCA ACA GCT G
52[118]53[120] 5'-handle	TGC GAT ATT GCA TTA ATG CTC CTT TTG ATA TTA GAG AGT ACC TTT A
24[118]25[120] 5'-handle	TGC GAT ATT GCA TTA ACC CTC ATT TTC AGG CCA CCC TCA GAG CCA C
46[127]47[125] 3'-handle	GTA ATA GTA AAA TGT TAG TTT TGC CAG AGG TGC GAT ATT GCA TTA A
74[127]75[125] 3'-handle	GAG CTC GAA TTC GTA AAG GAT CCC CGG GTA TGC GAT ATT GCA TTA A
18[127]19[125] 3'-handle	GTT TTA ACG GGG TCA GAG TGT ACT GGT AAT TGC GAT ATT GCA TTA A

CHOLESTEROL HANDLES

lipid handle arm1_HB 1	CAA ATT AAA GAA CTC AAA CAA GAA ACG CGC CCA ATC ATT CTC CTA TTA CTA CC
lipid handle arm1_HB 5	AGC TAG CCC TAA TGC CAT CTT TTC CGG AAC CGC CTC CCA GAG CCA GCA AAA TAC GGA AAC ATT CTC CTA TTA CTA CC
lipid handle arm1_HB 7	TTT TTT ACA GAC AAT ATT TTT GAA TGA AGA TAA ATT TTT TTT TTT TAT GAA ACC ACA TTC TCC TAT TAC TAC C
lipid handle arm 2_HB 29	CCC AGC GAA ATT GTG TCG AGG AAT CGC CGA ATA AAC ATT CTC CTA TTA CTA CC

lipid handle arm 2_HB 33	GCT CAT TAT ACA ATA AAA CGT TTT TTG TCT TTC ATT CTC CTA TTA CTA CC
lipid handle arm 2_HB 35	TTT TTT CTT GCC CTG ACG AGA AAC ATC TTT CCA GTT TTT TTT TTT TCA GAT ATA GCA TTC TCC TAT TAC TAC C
lipid handle arm 3_HB 57	TGA ACG GAG CCC CAA AAA CGC CGG AAC ACA TTT GAC ATT CTC CTA TTA CTA CC
lipid handle arm 3_HB 61	GGG ACT CCA GCC AGC TTA AAG CGC TTC AAT TCA ATA ACC ATT CTC CTA TTA CTA CC
lipid handle arm 3_HB 63	TTT TTT ACC GTA ATG GGA TAG GTC ATA AGA CGC TTT TTT TTT TTT TAT TAA TTA CCA TTC TCC TAT TAC TAC C

Alexa647-DNA conjugate: /Alexa647/ TTA ATG CAA TAT CGC A

Cholesterol-DNA conjugate: GGT AGT AAT AGG AGA ATG /3CholTEG/

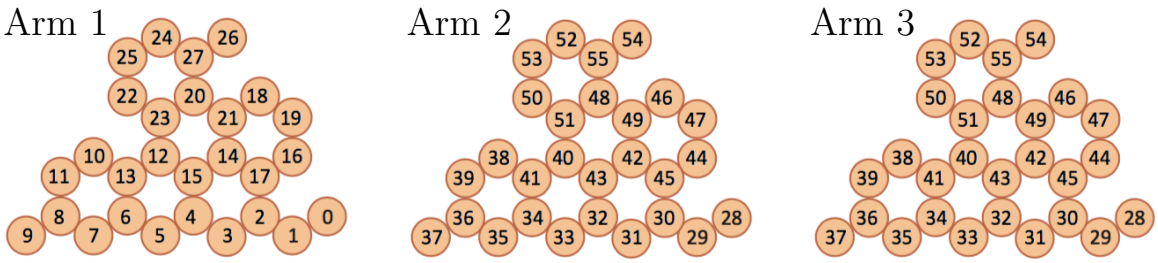

Figure C.1: Arrangement of helices.

Figure C.2: (Next page) **CADNAno routing for triskelion.** blue: DNA scaffold; black: main staples, common to flat and curved triskelia; red: staples bearing 6 bp sticky ends for polymerisation (Arm 2 and Arm 3); purple: dimerisation strands (Arm 1); green: strands bearing dye handle; yellow: strands bearing cholesterol handle. The last three lanes (HB 84, 85 and 87) are simplified representation of the bridges.

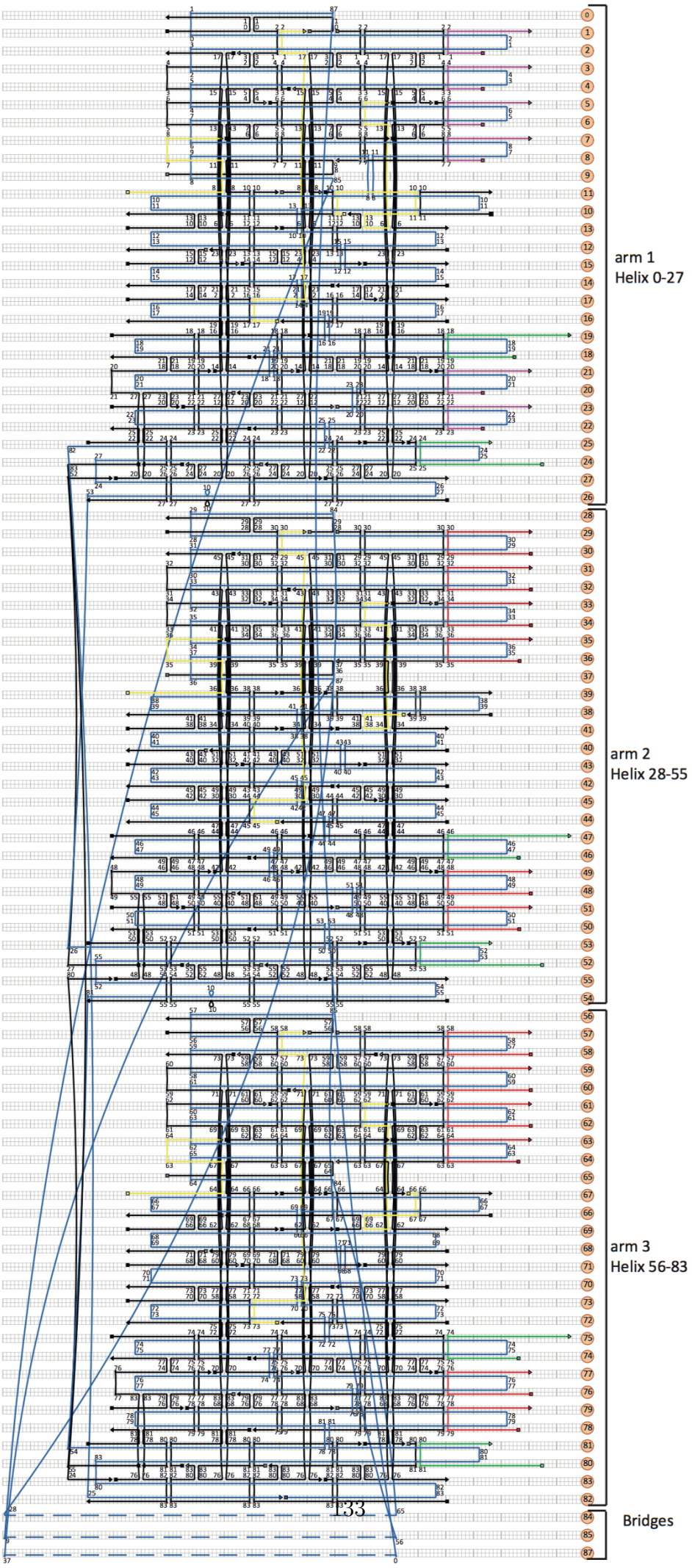
arm 1
Helix 0-27
arm 2
Helix 28-55
arm 3
Helix 56-83
Bridges

Bibliography

[1] Ruiz-Mirazo, K. & Moreno, A. Autonomy in evolution: from minimal to complex life. *Synthese* **185**, 21–52 (2012).

[2] Nelson, G. J. The phospholipid composition of plasma in various mammalian species. *Lipids* **2**, 323–328 (1967).

[3] Marquardt, D. *et al.* Lipid bilayer thickness determines cholesterol's location in model membranes. *Soft Matter* **12**, 9417–9428 (2016).

[4] Veatch, S. L. & Keller, S. L. Separation of liquid phases in giant vesicles of ternary mixtures of phospholipids and cholesterol. *Biophysical Journal* **85**, 3074–83 (2003).

[5] Needham, D. & Nunn, R. Elastic deformation and failure of lipid bilayer membranes containing cholesterol. *Biophysical Journal* **58**, 997–1009 (1990).

[6] Ohvo-Rekilä, H., Ramstedt, B., Leppimäki, P. & Slotte, J. P. Cholesterol interactions with phospholipids in membranes. *Progress in lipid research* **41**, 66–97 (2002).

[7] Lingwood, D. & Simons, K. Lipid Rafts As a Membrane-Organizing Principle. *Science* **327**, 46–50 (2010).

[8] Coker, H. L. E. *Anomalous Diffusion in Artificial Lipid Bilayers*. Ph.D. thesis, University of Oxford (2018).

[9] Silverstein, T. P. The Real Reason Why Oil and Water Don't Mix. *Journal of Chemical Education* **75**, 116 (1998).

[10] Israelachvili, J. N. *Intermolecular and surface forces* (Academic Press, 2011).

[11] Bangham, A. & Horne, R. Negative staining of phospholipids and their structural modification by surface-active agents as observed in the electron microscope. *Journal of Molecular Biology* **8**, 660–668 (1964).

[12] Siontorou, C. G., Nikoleli, G.-P., Nikolelis, D. P. & Karapetis, S. K. Artificial Lipid Membranes: Past, Present, and Future. *Membranes* **7**, 38 (2017).

[13] van den Brink-van der Laan, E., Antoinette Killian, J. & de Kruijff, B. Nonbilayer lipids affect peripheral and integral membrane proteins via changes in the lateral pressure profile. *Biochimica et Biophysica Acta (BBA) - Biomembranes* **1666**, 275–288 (2004).

[14] Alberts, B. *et al. Molecular biology of the cell* (Garland Science, 2002).

[15] Singer, S. J. & Nicolson, G. L. The fluid mosaic model of the structure of cell membranes. *Science (New York, N.Y.)* **175**, 720–31 (1972).

[16] Saffman, P. G. & Delbruck, M. Brownian motion in biological membranes. *Proceedings of the National Academy of Sciences of the United States of America* **72**, 3111–3113 (1975).

[17] Gracià, R. S., Bezlyepkina, N., Knorr, R. L., Lipowsky, R. & Dimova, R. Effect of cholesterol on the rigidity of saturated and unsaturated membranes: fluctuation and electrodeformation analysis of giant vesicles. *Soft Matter* **6**, 1472 (2010).

[18] García-Sáez, A. J., Chiantia, S. & Schwille, P. Effect of Line Tension on the Lateral Organization of Lipid Membranes. *Journal of Biological Chemistry* **282**, 33537–33544 (2007).

[19] Mouritsen, O. G. & Bagatolli, L. A. *Life - as a matter of fat* (Springer, 2005).

[20] Rothman, J. & Lenard, J. Membrane asymmetry. *Science* **195**, 743–753 (1977).

[21] Chiantia, S. & London, E. Lipid Bilayer Asymmetry. In *Encyclopedia of Biophysics*, 1250–1253 (Springer Berlin Heidelberg, Berlin, Heidelberg, 2013).

[22] Gupta, K. *et al.* The role of interfacial lipids in stabilizing membrane protein oligomers. *Nature* **541**, 421–424 (2017).

[23] Bernardino De La Serna, J., Schütz, G. J., Eggeling, C. & Cebecauer, M. There Is No Simple Model of the Plasma Membrane Organization. *Front. Cell Dev. Biol* **4**, 106 (2016).

[24] Holzer, M., Momm, J. & Schubert, R. Lipid Transfer Mediated by a Recombinant Pro-Sterol Carrier Protein 2 for the Accurate Preparation of Asymmetrical Membrane Vesicles Requires a Narrow Vesicle Size Distribution: A Free-Flow Electrophoresis Study. *Langmuir* **26**, 4142–4151 (2010).

[25] Thompson, J. R., Cronin, B., Bayley, H. & Wallace, M. I. Rapid assembly of a multimeric membrane protein pore. *Biophysical Journal* **101**, 2679–83 (2011).

[26] Roux, A. *et al.* Membrane curvature controls dynamin polymerization. *Proceedings of the National Academy of Sciences of the United States of America* **107**, 4141–6 (2010).

[27] Peraro, M. D. & van der Goot, F. G. Pore-forming toxins: ancient, but never really out of fashion. *Nature Reviews Microbiology* **14**, 77–92 (2016).

[28] Kusumi, A., Tsunoyama, T. A., Hirosawa, K. M., Kasai, R. S. & Fujiwara, T. K. Tracking single molecules at work in living cells. *Nature Chemical Biology* **10**, 524–532 (2014).

[29] Rawle, R. J., Boxer, S. G. & Kasson, P. M. Disentangling Viral Membrane Fusion from Receptor Binding Using Synthetic DNA-Lipid Conjugates. *Biophysical Journal* **111**, 123–131 (2016).

[30] Grakoui, A. *et al.* The immunological synapse: A molecular machine controlling T cell activation. *Science* **285**, 221–227 (1999).

[31] Schmid, E. M. *et al.* Size-dependent protein segregation at membrane interfaces. *Nature Physics* **12**, 704–711 (2016).

[32] Fenz, S. F., Merkel, R. & Sengupta, K. Diffusion and Intermembrane Distance: Case Study of Avidin and E-Cadherin Mediated Adhesion. *Langmuir* **25**, 1074–1085 (2009).

[33] Wen, P. J. *et al.* Actin dynamics provides membrane tension to merge fusing vesicles into the plasma membrane. *Nature Communications* **7**, 12604 (2016).

[34] Goode, B. L., Eskin, J. A. & Wendland, B. Actin and Endocytosis in Budding Yeast. *Genetics* **199**, 315–358 (2015).

[35] Kusumi, A. & Sako, Y. Cell surface organization by the membrane skeleton. *Current Opinion in Cell Biology* **8**, 566–74 (1996).

[36] Kusumi, A. *et al.* Paradigm Shift of the Plasma Membrane Concept from the Two-Dimensional Continuum Fluid to the Partitioned Fluid: High-Speed Single-Molecule Tracking of Membrane Molecules. *Annual Review of Biophysics and Biomolecular Structure* **34**, 351–378 (2005).

[37] Goswami, D. *et al.* Nanoclusters of GPI-Anchored Proteins Are Formed by Cortical Actin-Driven Activity. *Cell* **135**, 1085–1097 (2008).

[38] Jacobson, K., Ishihara, A. & Inman, R. Lateral Diffusion of Proteins in Membranes. *Annual Review of Physiology* **49**, 163–175 (1987).

[39] Sabri, S. *et al.* Glycocalyx modulation is a physiological means of regulating cell adhesion. *Journal of Cell Science* **113** (2000).

[40] Albersdorfer, A., Feder, T. & Sackmann, E. Adhesion-induced domain formation by interplay of long-range repulsion and short-range attraction force: a model membrane study. *Biophysical Journal* **73**, 245–257 (1997).

[41] Gallop, J. L. & McMahon, H. T. BAR domains and membrane curvature: bringing your curves to the BAR. *Biochemical Society Symposium* 223–31 (2005).

[42] Takei, K. *et al.* Generation of Coated Intermediates of Clathrin-Mediated Endocytosis on Protein-Free Liposomes. *Cell* **94**, 131–141 (1998).

[43] Nossal, R. Energetics of Clathrin Basket Assembly. *Traffic* **2**, 138–147 (2001).

[44] Stachowiak, J. C. *et al.* Membrane bending by protein-protein crowding. *Nature Cell Biology* **14**, 944–9 (2012).

[45] Zimmerberg, J. & Kozlov, M. M. How proteins produce cellular membrane curvature. *Nature Reviews Molecular Cell Biology* **7**, 9 (2005).

[46] Campelo, F., McMahon, H. T. & Kozlov, M. M. The Hydrophobic Insertion Mechanism of Membrane Curvature Generation by Proteins. *Biophysical Journal* **95**, 2325–2339 (2008).

[47] Drin, G. & Antonny, B. Amphipathic helices and membrane curvature. *FEBS Letters* **584**, 1840–1847 (2010).

[48] Fotin, A. *et al.* Molecular model for a complete clathrin lattice from electron cryomicroscopy. *Nature* **432**, 573–579 (2004).

[49] Antonny, B., Gounon, P., Schekman, R. & Orci, L. Self-assembly of minimal COPII cages. *EMBO Reports* **4**, 419–424 (2003).

[50] Kirchhausen, T. Imaging endocytic clathrin structures in living cells. *Trends in Cell Biology* **19**, 596–605 (2009).

[51] Kaksonen, M. & Roux, A. Mechanisms of clathrin-mediated endocytosis. *Nature Reviews Molecular Cell Biology* (2018).

[52] Mettlen, M., Pucadyil, T., Ramachandran, R. & Schmid, S. Dissecting dynamin's role in clathrin-mediated endocytosis. *Biochemical Society Transactions* **37**, 1022–1026 (2009).

[53] Pobbati, A. V., Stein, A. & Fasshauer, D. N- to C-terminal SNARE complex assembly promotes rapid membrane fusion. *Science* **313**, 673–6 (2006).

[54] Mayor, S., Parton, R. G. & Donaldson, J. G. Clathrin-independent pathways of endocytosis. *Cold Spring Harbor Perspectives in Biology* **6** (2014).

[55] Beams, H. & Kessel, R. The Golgi Apparatus: Structure and Function. *International Review of Cytology* **23**, 209–276 (1968).

[56] Yang, S.-T., Kiessling, V., Simmons, J. A., White, J. M. & Tamm, L. K. HIV gp41-mediated membrane fusion occurs at edges of cholesterol-rich lipid domains. *Nature Chemical Biology* **11**, 424–431 (2015).

[57] Hell, S. W. *et al.* The 2015 super-resolution microscopy roadmap. *Journal of Physics D: Applied Physics* **48**, 443001 (2015).

[58] Yokosuka, T. *et al.* Newly generated T cell receptor microclusters initiate and sustain T cell activation by recruitment of Zap70 and SLP-76. *Nature Immunology* **6**, 1253–1262 (2005).

[59] Montal, M. & Mueller, P. Formation of bimolecular membranes from lipid monolayers and a study of their electrical properties. *Proceedings of the National Academy of Sciences of the United States of America* **69**, 3561–6 (1972).

[60] Römer, W. & Steinem, C. Impedance Analysis and Single-Channel Recordings on Nano-Black Lipid Membranes Based on Porous Alumina. *Biophysical Journal* **86**, 955–965 (2004).

[61] Tamm, L. & McConnell, H. Supported phospholipid bilayers. *Biophysical Journal* **47**, 105–113 (1985).

[62] Brian, A. A. & McConnell, H. M. Allogeneic stimulation of cytotoxic T cells by supported planar membranes. *Proceedings of the National Academy of Sciences of the United States of America* **81**, 6159–63 (1984).

[63] Wong, A. P. & Groves, J. T. Molecular topography imaging by intermembrane fluorescence resonance energy transfer. *Proceedings of the National Academy of Sciences of the United States of America* **99**, 14147–14152 (2002).

[64] Charitat, T., Bellet-Amalric, E., Fragneto, G. & Graner, F. Adsorbed and free lipid bilayers at the solid-liquid interface. *The European Physical Journal B* **8**, 583–593 (1999).

[65] Knoll, W. *et al.* Functional tethered lipid bilayers. *Reviews in Molecular Biotechnology* **74**, 137–158 (2000).

[66] Tabaei, S. R., Jönsson, P., Brändén, M. & Höök, F. Self-assembly formation of multiple DNA-tethered lipid bilayers. *Journal of Structural Biology* **168**, 200–206 (2009).

[67] Wagner, M. L. & Tamm, L. K. Tethered Polymer-Supported Planar Lipid Bilayers for Reconstitution of Integral Membrane Proteins: Silane-Polyethyleneglycol-Lipid as a Cushion and Covalent Linker. *Biophysical Journal* **79**, 1400–1414 (2000).

[68] Bayley, H. *et al.* Droplet interface bilayers. *Molecular bioSystems* **4**, 1191–208 (2008).

[69] Civjan, N. R., Bayburt, T. H., Schuler, M. A. & Sligar, S. G. Direct solubilization of heterologously expressed membrane proteins by incorporation into nanoscale lipid bilayers. *BioTechniques* **35**, 556–563 (2003).

[70] Richter, R. P., Bérat, R. & Brisson, A. R. Formation of solid-supported lipid bilayers: An integrated view. *Langmuir* **22**, 3497–3505 (2006).

[71] Rigaud, J. L., Pitard, B. & Levy, D. Reconstitution of membrane proteins into liposomes: application to energy-transducing membrane proteins (1995).

[72] Aimon, S. *et al.* Membrane Shape Modulates Transmembrane Protein Distribution. *Developmental Cell* **28**, 212–218 (2014).

[73] Hindley, J. W. *et al.* Building a synthetic mechanosensitive signaling pathway in compartmentalized artificial cells. *Proceedings of the National Academy of Sciences of the United States of America* **116**, 16711–16716 (2019).

[74] Stengel, G., Zahn, R. & Höök, F. DNA-induced programmable fusion of phospholipid vesicles. *Journal of the American Chemical Society* **129**, 9584–9585 (2007).

[75] Dannhauser, P. N. & Ungewickell, E. J. Reconstitution of clathrin-coated bud and vesicle formation with minimal components. *Nature Cell Biology* **14**, 634–639 (2012).

[76] Fenz, S. F. & Sengupta, K. Giant vesicles as cell models. *Integrative Biology* **4**, 982–995 (2012).

[77] Blosser, M. C., Starr, J. B., Turtle, C. W., Ashcraft, J. & Keller, S. L. Minimal effect of lipid charge on membrane miscibility phase behavior in three ternary systems. *Biophysical Journal* **104**, 2629–38 (2013).

[78] Kurihara, K. *et al.* Self-reproduction of supramolecular giant vesicles combined with the amplification of encapsulated DNA. *Nature Chemistry* **3**, 775–781 (2011).

[79] Elani, Y., Law, R. V. & Ces, O. Vesicle-based artificial cells as chemical microreactors with spatially segregated reaction pathways. *Nature Communications* **5**, 5305 (2014).

[80] Cicuta, P., Keller, S. L. & Veatch, S. L. Diffusion of liquid domains in lipid bilayer membranes. *Journal of Physical Chemistry B* **111**, 3328–3331 (2007).

[81] Dimova, R. Recent developments in the field of bending rigidity measurements on membranes. *Advances in Colloid and Interface Science* **208**, 225–234 (2014).

[82] Henriksen, J., Rowat, A. C. & Ipsen, J. H. Vesicle fluctuation analysis of the effects of sterols on membrane bending rigidity. *European Biophysics Journal* **33**, 732–741 (2004).

[83] Reeves, J. P. & Dowben, R. M. Formation and properties of thin-walled phospholipid vesicles. *Journal of Cellular Physiology* **73**, 49–60 (1969).

[84] Angelova, M. I. & Dimitrov, D. S. Liposome electroformation. *Faraday Discussions of the Chemical Society* **81**, 303 (1986).

[85] Horger, K. S., Estes, D. J., Capone, R. & Mayer, M. Films of agarose enable rapid formation of giant liposomes in solutions of physiologic ionic strength. *Journal of the American Chemical Society* **131**, 1810–9 (2009).

[86] Girard, P. *et al.* A new method for the reconstitution of membrane proteins into giant unilamellar vesicles. *Biophysical Journal* **87**, 419–29 (2004).

[87] Pott, T., Bouvrais, H. & Méléard, P. Giant unilamellar vesicle formation under physiologically relevant conditions. *Chemistry and Physics of Lipids* **154**, 115–9 (2008).

[88] Mossman, K. & Groves, J. Micropatterned supported membranes as tools for quantitative studies of the immunological synapse. *Chemical Society Reviews* **36**, 46–54 (2007).

[89] Bayerl, T. M. & Bloom, M. Physical properties of single phospholipid bilayers adsorbed to micro glass beads. A new vesicular model system studied by 2H-nuclear magnetic resonance. *Biophysical Journal* **58**, 357–62 (1990).

[90] Axelrod, D. Cell-substrate contacts illuminated by total internal reflection fluorescence. *The Journal of Cell Biology* **89**, 141–145 (1981).

[91] van de Linde, S. Single-molecule localization microscopy analysis with ImageJ. *Journal of Physics D: Applied Physics* **52**, 203002 (2019).

[92] Thompson, R. E., Larson, D. R. & Webb, W. W. Precise Nanometer Localization Analysis for Individual Fluorescent Probes. *Biophysical Journal* **82**, 2775–2783 (2002).

[93] Einstein, A. On the Motion of Small Particles Suspended in Liquids at Rest Required by the Molecular-Kinetic Theory of Heat. *Annalen der Physik* **17**, 549–560 (1905).

[94] Block, S. Brownian Motion at Lipid Membranes: A Comparison of Hydrodynamic Models Describing and Experiments Quantifying Diffusion within Lipid Bilayers. *Biomolecules* **8**, 30 (2018).

[95] Evans, E. & Sackmann, E. Translational and rotational drag coefficients for a disk moving in a liquid membrane associated with a rigid substrate. *Journal of Fluid Mechanics* **194**, 553 (1988).

[96] Merkel, R., Sackmann, E. & Evans, E. Molecular friction and epitactic coupling between monolayers in supported bilayers. *Journal de Physique* **50** (1989).

[97] Scomparin, C., Lecuyer, S., Ferreira, M., Charitat, T. & Tinland, B. Diffusion in supported lipid bilayers: influence of substrate and preparation technique on the internal dynamics. *The European Physical Journal E* **28**, 211–20 (2009).

[98] Camley, B. A. & Brown, F. L. H. Diffusion of complex objects embedded in free and supported lipid bilayer membranes: role of shape anisotropy and leaflet structure. *Soft Matter* **9**, 4767 (2013).

[99] Bell, G., Dembo, M. & Bongrand, P. Cell adhesion. Competition between nonspecific repulsion and specific bonding. *Biophysical Journal* **45**, 1051–1064 (1984).

[100] Bruinsma, R., Behrisch, A. & Sackmann, E. Adhesive switching of membranes: Experiment and theory. *Physical Review E - Statistical Physics, Plasmas, Fluids, and Related Interdisciplinary Topics* **61**, 4253–4267 (2000).

[101] Weikl, T. R. & Lipowsky, R. Advances in Planar Lipid Bilayers and Liposomes. Chapter 4: Membrane Adhesion and Domain Formation (2006).

[102] Biswas, K. H. & Groves, J. T. Hybrid Live Cell–Supported Membrane Interfaces for Signaling Studies. *Annual Review of Biophysics* **48**, 537–562 (2019).

[103] Kloboucek, A., Behrisch, A., Faix, J. & Sackmann, E. Adhesion-Induced Receptor Segregation and Adhesion Plaque Formation: A Model Membrane Study. *Biophysical Journal* **77**, 2311–2328 (1999).

[104] Smith, A.-S., Sengupta, K., Goennenwein, S., Seifert, U. & Sackmann, E. Force-induced growth of adhesion domains is controlled by receptor mobility. *Proceedings of the National Academy of Sciences of the United States of America* **105**, 6906–6911 (2008).

[105] Bongrand, P. Ligand-receptor interactions. *Reports on Progress in Physics* **62**, 921–968 (1999).

[106] Sackmann, E. & Smith, A. S. Physics of cell adhesion: Some lessons from cell-mimetic systems (2014).

[107] Wong, A. P. & Groves, J. T. Topographical imaging of an intermembrane junction by combined fluorescence interference and energy transfer microscopies (2001).

[108] Kaizuka, Y. & Groves, J. T. Structure and Dynamics of Supported Intermembrane Junctions. *Biophysical Journal* **86**, 905–912 (2004).

[109] Chung, M., Lowe, R. D., Chan, Y. H. M., Ganesan, P. V. & Boxer, S. G. DNA-tethered membranes formed by giant vesicle rupture. *Journal of Structural Biology* **168**, 190–199 (2009).

[110] Chung, M., Koo, B. J. & Boxer, S. G. Formation and analysis of topographical domains between lipid membranes tethered by DNA hybrids of different lengths. *Faraday Discussions* **161**, 333–345 (2012).

[111] McCloskey, M. A. & Poo, M. M. Contact-induced redistribution of specific membrane components: local accumulation and development of adhesion. *The Journal of Cell Biology* **102**, 2185–96 (1986).

[112] Aoki, P. H., Schroder, A. P., Constantino, C. J. & Marques, C. M. Bioadhesive giant vesicles for monitoring hydroperoxidation in lipid membranes. *Soft Matter* **11**, 5995–5998 (2015).

[113] Heath, G. R. *et al.* Layer-by-Layer Assembly of Supported Lipid Bilayer Poly-l -Lysine Multilayers. *Biomacromolecules* **17**, 324–335 (2016).

[114] Mossman, K. D., Campi, G., Groves, J. T. & Dustin, M. L. Altered TCR Signaling from Geometrically Repatterned Immunological Synapses. *Science* **310**, 1191–1193 (2005).

[115] Yu, Y., Smoligovets, A. A. & Groves, J. T. Modulation of T cell signaling by the actin cytoskeleton. *Journal of Cell Science* **126**, 1049–1058 (2013).

[116] Chang, V. T. *et al.* Initiation of T cell signaling by CD45 segregation at 'close contacts'. *Nature Immunology* **17**, 574–582 (2016).

[117] Dustin, M. L., Sanders, M. E., Shaw, S. & Springer, T. A. Purified lymphocyte function-associated antigen 3 binds to CD2 and mediates T lymphocyte adhesion. *The Journal of Experimental Medicine* **165**, 677–92 (1987).

[118] Selvaraj, P. *et al.* The T lymphocyte glycoprotein CD2 binds the cell surface ligand LFA-3. *Nature* **326**, 400–403 (1987).

[119] Dustin, M. L. & Springer, T. A. Lymphocyte function-associated antigen-1 (LFA-1) interaction with intercellular adhesion molecule-1 (ICAM-1) is one of at least three mechanisms for lymphocyte adhesion to cultured endothelial cells. *The Journal of Cell Biology* **107**, 321–31 (1988).

[120] Dustin, M. L., Bromley, S. K., Davis, M. M. & Zhu, C. Identification of Self Through Two-Dimensional Chemistry and Synapses. *Annual Review of Cell and Developmental Biology* **17**, 133–157 (2001).

[121] Chan, P. Y. *et al.* Influence of receptor lateral mobility on adhesion strengthening between membranes containing LFA-3 and CD2. *Journal of Cell Biology* **115**, 245–255 (1991).

[122] Tozeren, A. *et al.* Micromanipulation of adhesion of a Jurkat cell to a planar bilayer membrane containing lymphocyte function-associated antigen 3 molecules. *Journal of Cell Biology* **116**, 997–1006 (1992).

[123] Helfrich, W. Steric Interaction of Fluid Membranes in Multilayer Systems. *Zeitschrift fur Naturforschung - A* **33**, 305–315 (1978).

[124] Holliday, R. A mechanism for gene conversion in fungi. *Genetical Research* **5**, 282 (1964).

[125] Seeman, N. Nucleic acid junctions: Building blocks for genetic engineering in three dimensions. In R.H. Sarma (ed.) *Biomolecular Stereodynamics*, 269–277 (Adenine Press, New York, 1981).

[126] Seeman, N. C. Nucleic acid junctions and lattices. *Journal of Theoretical Biology* **99**, 237–247 (1982).

[127] Chen, J. & Seeman, N. C. Synthesis from DNA of a molecule with the connectivity of a cube. *Nature* **350**, 631–633 (1991).

[128] Börjesson, K., Lundberg, E. P., Woller, J. G., Nordén, B. & Albinsson, B. Soft-surface DNA nanotechnology: DNA constructs anchored and aligned to lipid membrane. *Angewandte Chemie International Edition* **50**, 8312–8315 (2011).

[129] Pfeiffer, I. & Höök, F. Bivalent cholesterol-based coupling of oligonucletides to lipid membrane assemblies. *Journal of the American Chemical Society* **126**, 10224–10225 (2004).

[130] Yoshina-Ishii, C. & Boxer, S. G. Arrays of mobile tethered vesicles on supported lipid bilayers. *Journal of the American Chemical Society* **125**, 3696–3697 (2003).

[131] Yoshina-Ishii, C. *et al.* Diffusive dynamics of vesicles tethered to a fluid supported bilayer by single-particle tracking. *Langmuir* **22**, 5682–5689 (2006).

[132] Chan, Y.-H. M., Lenz, P. & Boxer, S. G. Kinetics of DNA-mediated docking reactions between vesicles tethered to supported lipid bilayers. *Proceedings of the National Academy of Sciences of the United States of America* **104**, 18913–8 (2007).

[133] Chan, Y.-H. M., van Lengerich, B. & Boxer, S. G. Lipid-anchored DNA mediates vesicle fusion as observed by lipid and content mixing. *Biointerphases* **3**, FA17–FA21 (2008).

[134] Chan, Y.-H. M., van Lengerich, B. & Boxer, S. G. Effects of linker sequences on vesicle fusion mediated by lipid-anchored DNA oligonucleotides. *Proceedings of the National Academy of Sciences of the United States of America* **106**, 979–84 (2009).

[135] Rawle, R., van Lengerich, B., Chung, M., Bendix, P. & Boxer, S. Vesicle Fusion Observed by Content Transfer across a Tethered Lipid Bilayer. *Biophysical Journal* **101**, L37–L39 (2011).

[136] van Lengerich, B., Rawle, R., Bendix, P. & Boxer, S. Individual Vesicle Fusion Events Mediated by Lipid-Anchored DNA. *Biophysical Journal* **105**, 409–419 (2013).

[137] Beales, P. A. & Kyle Vanderlick, T. Specific binding of different vesicle populations by the hybridization of membrane-anchored DNA. *Journal of Physical Chemistry A* **111**, 12372–12380 (2007).

[138] Beales, P. A. & Vanderlick, T. K. DNA as Membrane-Bound Ligand-Receptor Pairs: Duplex Stability Is Tuned by Intermembrane Forces. *Biophysical Journal* **96**, 1554–1565 (2009).

[139] Parolini, L. *et al.* Volume and porosity thermal regulation in lipid mesophases by coupling mobile ligands to soft membranes. *Nature Communications* **6**, 5948 (2015).

[140] Shimobayashi, S. F. *et al.* Direct measurement of DNA-mediated adhesion between lipid bilayers. *Physical Chemistry Chemical Physics* **17**, 15615–15628 (2015).

[141] Taylor, M. J., Husain, K., Gartner, Z. J., Mayor, S. & Vale, R. D. A DNA-Based T Cell Receptor Reveals a Role for Receptor Clustering in Ligand Discrimination. *Cell* **169**, 108–119.e20 (2017).

[142] Rothemund, P. W. K. Folding DNA to create nanoscale shapes and patterns. *Nature* **440**, 297–302 (2006).

[143] Czogalla, A., Franquelim, H. & Schwille, P. DNA Nanostructures on Membranes as Tools for Synthetic Biology. *Biophysical Journal* **110**, 1698–1707 (2016).

[144] Suzuki, Y., Endo, M. & Sugiyama, H. Lipid-bilayer-assisted two-dimensional self-assembly of DNA origami nanostructures. *Nature Communications* **6**, 8052 (2015).

[145] Johnson-Buck, A., Jiang, S., Yan, H. & Walter, N. G. DNA–Cholesterol Barges as Programmable Membrane-Exploring Agents. *ACS Nano* **8**, 5641–5649 (2014).

[146] Arnott, P. M., Joshi, H., Aksimentiev, A. & Howorka, S. Dynamic Interactions between Lipid-Tethered DNA and Phospholipid Membranes. *Langmuir* **34**, 15084–15092 (2018).

[147] Czogalla, A. *et al.* Amphipathic DNA Origami Nanoparticles to Scaffold and Deform Lipid Membrane Vesicles. *Angewandte Chemie International Edition* **54**, 6501–6505 (2015).

[148] Avakyan, N., Conway, J. W. & Sleiman, H. F. Long-Range Ordering of Blunt-Ended DNA Tiles on Supported Lipid Bilayers. *Journal of the American Chemical Society* **139**, 12027–12034 (2017).

[149] Kocabey, S. *et al.* Membrane-Assisted Growth of DNA Origami Nanostructure Arrays. *ACS Nano* **9**, 3530–3539 (2015).

[150] Zhang, Z., Yang, Y., Pincet, F., Llaguno, M. C. & Lin, C. Placing and shaping liposomes with reconfigurable DNA nanocages. *Nature Chemistry* **9**, 653 (2017).

[151] Birkholz, O. *et al.* Multi-functional DNA nanostructures that puncture and remodel lipid membranes into hybrid materials. *Nature Communications* **9**, 1521 (2018).

[152] Douglas, S. M. *et al.* Self-assembly of DNA into nanoscale three-dimensional shapes. *Nature* **459**, 414 (2009).

[153] Xu, W. *et al.* A Programmable DNA Origami Platform to Organize SNAREs for Membrane Fusion. *Journal of the American Chemical Society* **138**, 4439–4447 (2016).

[154] Franquelim, H. G., Khmelinskaia, A., Sobczak, J.-P., Dietz, H. & Schwille, P. Membrane sculpting by curved DNA origami scaffolds. *Nature Communications* **9**, 811 (2018).

[155] Grome, M. W., Zhang, Z., Pincet, F. & Lin, C. Vesicle Tubulation with Self-Assembling DNA Nanosprings. *Angewandte Chemie International Edition* **57**, 5330–5334 (2018).

[156] Schoch, R. L., Barel, I., Brown, F. L. H. & Haran, G. Lipid diffusion in the distal and proximal leaflets of supported lipid bilayer membranes studied by single particle tracking. *The Journal of Chemical Physics* **148**, 123333 (2018).

[157] Saxton, M. J. Lateral diffusion in an archipelago. The effect of mobile obstacles. *Biophysical Journal* **52**, 989–97 (1987).

[158] Saxton, M. Lateral diffusion in an archipelago. Distance dependence of the diffusion coefficient. *Biophysical Journal* **56**, 615–622 (1989).

[159] Saxton, M. J. Anomalous diffusion due to obstacles: a Monte Carlo study. *Biophysical Journal* **66**, 394–401 (1994).

[160] Guo, L. *et al.* Molecular Diffusion Measurement in Lipid Bilayers over Wide Concentration Ranges: A Comparative Study. *ChemPhysChem* **9**, 721–728 (2008).

[161] Saxton, M. J. & Jacobson, K. Single-particle Tracking:Applications to Membrane Dynamics. *Annual Review of Biophysics and Biomolecular Structure* **26**, 373–399 (1997).

[162] Adler, J., Shevchuk, A. I., Novak, P., Korchev, Y. E. & Parmryd, I. Plasma membrane topography and interpretation of single-particle tracks. *Nature Methods* **7**, 170–171 (2010).

[163] Sharonov, A. *et al.* Lipid diffusion from single molecules of a labeled protein undergoing dynamic association with giant unilamellar vesicles and supported bilayers. *Langmuir* **24**, 844–850 (2008).

[164] Woodward, X., Stimpson, E. E. & Kelly, C. V. Single-lipid tracking on nanoscale membrane buds: The effects of curvature on lipid diffusion and sorting. *Biochimica et Biophysica Acta (BBA) - Biomembranes* **1860**, 2064–2075 (2018).

[165] Coker, H. L. *et al.* Controlling Anomalous Diffusion in Lipid Membranes. *Biophysical Journal* **116**, 1085–1094 (2019).

[166] Murray, D. H., Tamm, L. K. & Kiessling, V. Supported double membranes. *Journal of structural biology* **168**, 183–9 (2009).

[167] Wang, T., Ingram, C. & Weisshaar, J. C. Model Lipid Bilayer with Facile Diffusion of Lipids and Integral Membrane Proteins. *Langmuir* **26**, 11157–11164 (2010).

[168] Bunge, A. *et al.* Lipid Membranes Carrying Lipophilic Cholesterol-Based Oligonucleotides—Characterization and Application on Layer-by-Layer Coated Particles. *The Journal of Physical Chemistry B* **113**, 16425–16434 (2009).

[169] Lira, R. B., Dimova, R. & Riske, K. A. Giant unilamellar vesicles formed by hybrid films of agarose and lipids display altered mechanical properties. *Biophysical Journal* **107**, 1609–19 (2014).

[170] Mertins, O., da Silveira, N. P., Pohlmann, A. R., Schröder, A. P. & Marques, C. M. Electroformation of Giant Vesicles from an Inverse Phase Precursor. *Biophysical Journal* **96**, 2719–2726 (2009).

[171] Morales-Penningston, N. F. *et al.* GUV preparation and imaging: Minimizing artifacts. *Biochimica et Biophysica Acta (BBA) - Biomembranes* **1798**, 1324–1332 (2010).

[172] Tinevez, J.-Y. *et al.* TrackMate: An open and extensible platform for single-particle tracking. *Methods* **115**, 80–90 (2017).

[173] Axelrod, D., Koppel, D., Schlessinger, J., Elson, E. & Webb, W. Mobility measurement by analysis of fluorescence photobleaching recovery kinetics. *Biophysical Journal* **16**, 1055–1069 (1976).

[174] Soumpasis, D. M. Theoretical analysis of fluorescence photobleaching recovery experiments. *Biophysical Journal* **41**, 95–7 (1983).

[175] Schindelin, J. *et al.* Fiji: an open-source platform for biological-image analysis. *Nature Methods* **9**, 676–682 (2012).

[176] Kong, H., Akakin, H. C. & Sarma, S. E. A Generalized Laplacian of Gaussian Filter for Blob Detection and Its Applications. *IEEE Transactions on Cybernetics* **43**, 1719–1733 (2013).

[177] Getting started with TrackMate - ImageJ. `https://imagej.net/Getting_started_with_TrackMate`. Accessed: 2019-10-08.

[178] Jaqaman, K. *et al.* Robust single-particle tracking in live-cell time-lapse sequences. *Nature Methods* **5**, 695–702 (2008).

[179] Banchelli, M. *et al.* Phospholipid membranes decorated by cholesterol-based oligonucleotides as soft hybrid nanostructures. *The Journal of Physical Chemistry B* **112**, 10942–52 (2008).

[180] Georgiev, V., Bléger, D., Grafmüller, A., Hecht, S. & Dimova, R. Light-Induced Transformations in Lipid Membranes. *Biophysical Journal* **108**, 240a (2015).

[181] de Wit, G., Danial, J. S. H., Kukura, P. & Wallace, M. I. Dynamic label-free imaging of lipid nanodomains. *Proceedings of the National Academy of Sciences of the United States of America* **112**, 12299–303 (2015).

[182] Danial, J. S. H. *Imaging lipid phase separation in droplet interface bilayers.* Ph.D. thesis, University of Oxford (2015).

[183] Marx, S., Schilling, J., Sackmann, E. & Bruinsma, R. Helfrich Repulsion and Dynamical Phase Separation of Multicomponent Lipid Bilayers. *Physical Review Letters* **88**, 138102 (2002).

[184] Parthasarathy, R., Jackson, B. L., Lowery, T. J., Wong, A. P. & Groves, J. T. Nonequilibrium Adhesion Patterns at Lipid Bilayer Junctions. *Journal of Physical Chemistry B* **108**, 649–657 (2004).

[185] Hamai, C., Cremer, P. S. & Musser, S. M. Single giant vesicle rupture events reveal multiple mechanisms of glass-supported bilayer formation. *Biophysical Journal* **92**, 1988–1999 (2007).

[186] Borst, J. W., Visser, N. V., Kouptsova, O. & Visser, A. J. Oxidation of unsaturated phospholipids in membrane bilayer mixtures is accompanied by membrane fluidity changes. *Biochimica et Biophysica Acta (BBA) - Molecular and Cell Biology of Lipids* **1487**, 61–73 (2000).

[187] Megli, F. M. & Russo, L. Different oxidized phospholipid molecules unequally affect bilayer packing. *Biochimica et Biophysica Acta (BBA) - Biomembranes* **1778**, 143–152 (2008).

[188] Melcrová, A. *et al.* The complex nature of calcium cation interactions with phospholipid bilayers. *Scientific Reports* **6**, 38035 (2016).

[189] Alsop, R. J., Maria Schober, R. & Rheinstädter, M. C. Swelling of phospholipid membranes by divalent metal ions depends on the location of the ions in the bilayers. *Soft Matter* **12**, 6737–6748 (2016).

[190] Ali Doosti, B. *et al.* Membrane Tubulation in Lipid Vesicles Triggered by the Local Application of Calcium Ions. *Langmuir* **33**, 11010–11017 (2017).

[191] Komorowski, K. *et al.* Vesicle Adhesion and Fusion Studied by Small-Angle X-Ray Scattering. *Biophysical Journal* **114**, 1908–1920 (2018).

[192] Sharma, P. Entropic force between membranes reexamined. *Proceedings of the National Academy of Sciences of the United States of America* **110**, 1976–7 (2013).

[193] Groves, J. T. Molecular Organization and Signal Transduction at Intermembrane Junctions. *Angewandte Chemie International Edition* **44**, 3524–3538 (2005).

[194] Przybylo, M. *et al.* Lipid diffusion in giant unilamellar vesicles is more than 2 times faster than in supported phospholipid bilayers under identical conditions. *Langmuir* **22**, 9096–9099 (2006).

[195] Sonnleitner, A., Schütz, G. J. & Schmidt, T. Free Brownian motion of individual lipid molecules in biomembranes. *Biophysical Journal* **77**, 2638–42 (1999).

[196] Weigel, A. V., Simon, B., Tamkun, M. M. & Krapf, D. Ergodic and nonergodic processes coexist in the plasma membrane as observed by single-molecule tracking. *Proceedings of the National Academy of Sciences of the United States of America* **108**, 6438–43 (2011).

[197] Berry, H. & Chaté, H. Anomalous diffusion due to hindering by mobile obstacles undergoing Brownian motion or Orstein-Ulhenbeck processes. *Physical Review E* **89**, 022708 (2014).

[198] Chen, H. *et al.* Ionic strength-dependent persistence lengths of single-stranded RNA and DNA. *Proceedings of the National Academy of Sciences of the United States of America* **109**, 799–804 (2012).

[199] Bockelmann, U., Essevaz-Roulet, B. & Heslot, F. DNA strand separation studied by single molecule force measurements. *Physical Review E* **58**, 2386–2394 (1998).

[200] Chi, Q., Wang, G. & Jiang, J. The persistence length and length per base of single-stranded DNA obtained from fluorescence correlation spectroscopy measurements using mean field theory. *Physica A: Statistical Mechanics and its Applications* **392**, 1072–1079 (2013).

[201] Murphy, M. C., Rasnik, I., Cheng, W., Lohman, T. M. & Ha, T. Probing single-stranded DNA conformational flexibility using fluorescence spectroscopy. *Biophysical Journal* **86**, 2530–7 (2004).

[202] Sim, A. Y., Lipfert, J., Herschlag, D. & Doniach, S. Salt dependence of the radius of gyration and flexibility of single-stranded DNA in solution probed by small-angle x-ray scattering. *Physical Review E - Statistical, Nonlinear, and Soft Matter Physics* **86**, 021901 (2012).

[203] Rao, A. N. & Grainger, D. W. Biophysical properties of nucleic acids at surfaces relevant to microarray performance (2014).

[204] Gambinossi, F. *et al.* Modulation of Density and Orientation of Amphiphilic DNA Anchored to Phospholipid Membranes. I. Supported Lipid Bilayers. *The Journal of Physical Chemistry B* **114**, 7338–7347 (2010).

[205] Furrer, P. *et al.* Opposite effect of counterions on the persistence length of nicked and non-nicked DNA. *Journal of Molecular Biology* **266**, 711–721 (1997).

[206] Kahya, N., Scherfeld, D., Bacia, K., Poolman, B. & Schwille, P. Probing Lipid Mobility of Raft-exhibiting Model Membranes by Fluorescence Correlation Spectroscopy. *Journal of Biological Chemistry* **278**, 28109–28115 (2003).

[207] Doeven, M. K. *et al.* Distribution, lateral mobility and function of membrane proteins incorporated into giant unilamellar vesicles. *Biophysical Journal* **88**, 1134–42 (2005).

[208] Ramadurai, S. *et al.* Lateral Diffusion of Membrane Proteins. *Journal of the American Chemical Society* **131**, 12650–12656 (2009).

[209] Peel, C. *et al.* Coupled diffusion processes and 2D affinities of adhesion molecules at synthetic membrane junctions. *Bulletin of the American Physical Society* **Volume 61,** (2016).

[210] Wu, Y. *et al.* Cooperativity between trans and cis interactions in cadherin-mediated junction formation. *Proceedings of the National Academy of Sciences of the United States of America* **107**, 17592–7 (2010).

[211] Bruinsma, R., Goulian, M. & Pincus, P. Self-assembly of membrane junctions. *Biophysical Journal* **67**, 746–50 (1994).

[212] Glazier, R. & Salaita, K. Supported lipid bilayer platforms to probe cell mechanobiology. *Biochimica et Biophysica Acta (BBA) - Biomembranes* **1859**, 1465–1482 (2017).

[213] Hormel, T. T., Kurihara, S. Q., Brennan, M. K., Wozniak, M. C. & Parthasarathy, R. Measuring Lipid Membrane Viscosity Using Rotational and Translational Probe Diffusion. *Physical Review Letters* **112**, 188101 (2014).

[214] Vaz, W. L. C., Clegg, R. M. & Hallmann, D. Translational diffusion of lipids in liquid crystalline phase phosphatidylcholine multibilayers. A comparison of experiment with theory. *Biochemistry* **24**, 781–786 (1985).

[215] Herold, C., Schwille, P. & Petrov, E. P. DNA Condensation at Freestanding Cationic Lipid Bilayers. *Physical Review Letters* **104**, 148102 (2010).

[216] Tero, R. Substrate Effects on the Formation Process, Structure and Physicochemical Properties of Supported Lipid Bilayers. *Materials* **5**, 2658–2680 (2012).

[217] Xing, C. & Faller, R. Interactions of Lipid Bilayers with Supports: A Coarse-Grained Molecular Simulation Study. *The Journal of Physical Chemistry B* **112**, 7086–7094 (2008).

[218] Stone, H. A. & Ajdari, A. Hydrodynamics of particles embedded in a flat surfactant layer overlying a subphase of finite depth. *Journal of Fluid Mechanics* **369**, 151–173 (1998).

[219] Takamori, S. *et al.* Molecular Anatomy of a Trafficking Organelle. *Cell* **127**, 831–846 (2006).

[220] Quinn, P., Griffiths, G. & Warren, G. Density of newly synthesized plasma membrane proteins in intracellular membranes II. Biochemical studies. *The Journal of Cell Biology* **98**, 2142–7 (1984).

[221] Brisson, A. & Unwin, P. N. Tubular crystals of acetylcholine receptor. *The Journal of Cell Biology* **99**, 1202–11 (1984).

[222] Pereno, V. *et al.* Electroformation of Giant Unilamellar Vesicles on Stainless Steel Electrodes. *ACS Omega* **2**, 994–1002 (2017).

[223] McMahon, H. T. & Gallop, J. L. Membrane curvature and mechanisms of dynamic cell membrane remodelling. *Nature* **438**, 590–596 (2005).

[224] Cooke, I. R. & Deserno, M. Coupling between lipid shape and membrane curvature. *Biophysical Journal* **91**, 487–95 (2006).

[225] Peter, B. J. *et al.* BAR Domains as Sensors of Membrane Curvature: The Amphiphysin BAR Structure. *Science* **303**, 495–499 (2004).

[226] Doherty, G. J. & McMahon, H. T. Mechanisms of Endocytosis. *Annual Review of Biochemistry* **78**, 857–902 (2009).

[227] Jahn, R. & Scheller, R. H. SNAREs — engines for membrane fusion. *Nature Reviews Molecular Cell Biology* **7**, 631 (2006).

[228] Sleytr, U. B., Schuster, B., Egelseer, E.-M. & Pum, D. S-layers: principles and applications. *FEMS Microbiology Reviews* **38**, 823–864 (2014).

[229] Bouter, A. *et al.* Annexin-A5 assembled into two-dimensional arrays promotes cell membrane repair. *Nature Communications* **2**, 270 (2011).

[230] Kirchhausen, T. & Harrison, S. C. Protein organization in clathrin trimers. *Cell* **23**, 755–761 (1981).

[231] Kirchhausen, T., Harrison, S. & Heuser, J. Configuration of clathrin trimers: Evidence from electron microscopy. *Journal of Ultrastructure and Molecular Structure Research* **94**, 199–208 (1986).

[232] Pearse, B. M. Clathrin: a unique protein associated with intracellular transfer of membrane by coated vesicles. *Proceedings of the National Academy of Sciences of the United States of America* **73**, 1255–9 (1976).

[233] Cheng, Y., Boll, W., Kirchhausen, T., Harrison, S. C. & Walz, T. Cryo-electron Tomography of Clathrin-coated Vesicles: Structural Implications for Coat Assembly. *Journal of Molecular Biology* **365**, 892–899 (2007).

[234] Heuser, J. Three-dimensional visualization of coated vesicle formation in fibroblasts. *The Journal of Cell Biology* **84**, 560–583 (1980).

[235] McMahon, H. T. & Boucrot, E. Molecular mechanism and physiological functions of clathrin-mediated endocytosis. *Nature Reviews Molecular Cell Biology* **12**, 517–533 (2011).

[236] Kirchhausen, T., Owen, D. & Harrison, S. C. Molecular structure, function, and dynamics of clathrin-mediated membrane traffic. *Cold Spring Harbor Perspectives in Biology* **6**, a016725 (2014).

[237] Ferguson, M. L. *et al.* Clathrin Triskelia Show Evidence of Molecular Flexibility. *Biophysical Journal* **95**, 1945–1955 (2008).

[238] Ferguson, J. P. *et al.* Mechanoregulation of clathrin-mediated endocytosis. *Journal of Cell Science* **130**, 3631–3636 (2017).

[239] Journot, C. *On the interaction of DNA nanostructures with lipid bilayers*. Ph.D. thesis, University of Oxford (2017).

[240] Heuser, J. E., Keen, J. H., Amende, L. M., Lippoldt, R. E. & Prasad, K. Deep-etch visualization of 27S clathrin: a tetrahedral tetramer. *The Journal of Cell Biology* **105**, 1999–2009 (1987).

[241] Birkholz, O. *et al.* Multi-functional DNA nanostructures that puncture and remodel lipid membranes into hybrid materials. *Nature Communications* **9**, 1521 (2018).

[242] Antonny, B. Mechanisms of Membrane Curvature Sensing. *Annual Review of Biochemistry* **80**, 101–123 (2011).

[243] Bhatia, V. K., Hatzakis, N. S. & Stamou, D. A unifying mechanism accounts for sensing of membrane curvature by BAR domains, amphipathic helices and membrane-anchored proteins. *Seminars in Cell & Developmental Biology* **21**, 381–390 (2010).

[244] Kirchhausen, T. Bending membranes. *Nature Cell Biology* **14**, 906–908 (2012).

[245] Springer, T., Sípová, H., Vaisocherová, H., Stepánek, J. & Homola, J. Shielding effect of monovalent and divalent cations on solid-phase DNA hybridization: surface plasmon resonance biosensor study. *Nucleic Acids Research* **38**, 7343–51 (2010).

[246] Bell, G. I. Models for the specific adhesion of cells to cells. *Science* **200**, 618–627 (1978).

[247] Langecker, M., Arnaut, V., List, J. & Simmel, F. C. DNA Nanostructures Interacting with Lipid Bilayer Membranes. *Accounts of Chemical Research* **47**, 1807–1815 (2014).

[248] Keller, C. A., Glasmästar, K., Zhdanov, V. P. & Kasemo, B. Formation of Supported Membranes from Vesicles. *Physical Review Letters* **84**, 5443–5446 (2000).

[249] Stewart, J. C. M. Colorimetric determination of phospholipids with ammonium ferrothiocyanate. *Analytical Biochemistry* **104**, 10–14 (1980).